Department of Physics and Astronomy
Heidelberg University

Bachelor Thesis in Physics
submitted by

Nikita Philip Tatsch

born in Heidelberg (Germany)

2022

Software development and validation for photon measurements in Run 3 using the photon conversion method in ALICE

This Bachelor Thesis has been carried out by Nikita Philip Tatsch at the
Physikalisches Institut Universität Heidelberg, Heidelberg (Germany)
under the supervision of
Prof. Dr. Johanna Stachel

Abstract

During the Long Shutdown 2 upgrades to the LHC injector system were installed to increase the collision rate to 50 kHz for Pb–Pb collisions along with other major modifications. To cope with the increased data rate several modifications in the central barrel detectors of the ALICE experiment were performed. Furthermore, a new data processing framework, O^2, was implemented to handle the increase of data rates by up to 100 times in Run 3. Using the photon conversion method, the current state of the software for photon analysis is validated for the Pilot Beam of October of 2021 and the corresponding Monte Carlo simulation LHC22c5. In the process the existing analysis chain in the O^2 framework was supplemented with additional tables, histograms and recalculations for the conversion point coordinates and several post-processing scripts were written from scratch. It was noticed, that the detector material is not fully implemented for Monte Carlo simulations yet. A conversion probability of p_{conv} = 10.7 % for the radial range of $0\,\text{cm} < R < 180\,\text{cm}$ and p_{conv} = 4.2 % for the radial range of $0\,\text{cm} < R < 42\,\text{cm}$ as an average of the photons transverse momentum range p_T of $0.8\,\text{GeV/c} < p_T < 4.0\,\text{GeV/c}$ was determined. Moreover, a reconstruction efficiency for photon conversions of ϵ_{rec} = 4.76 % for transverse momenta of photons in the range of $1.5\,\text{GeV/c} < p_T < 3.0\,\text{GeV/c}$ was calculated. The reconstruction efficiency for the whole transverse momentum range was found to be ϵ_{rec} = 0.42 %. The spacial and momentum resolution of the vertex for the transverse plane was determined to $(3.75 \pm 0.09)\,\text{cm}$ and $(0.0245 \pm 0.0008)\,\text{GeV/c}$, respectively. By recalculating the conversion point coordinates the transverse spacial resolution was improved by a factor of (1.73 ± 0.05).

Zusammenfassung

Während dem Long Shutdown 2 wurden Neuerungen an dem Injetione-system installiert, um unter anderem die Kollisionsrate für Pb–Pb Kollisionen auf 50 kHz zu erhöhen. Einige der Detektorkomponenten am ALICE Experiment wurden erneuert oder ausgetauscht, um mit höheren Kollisionsraten klarzukommen. Des Weiteren wurde ein neues Framework zur Datenverarbeitung implementiert, dass mit um bis zu hundertfachen Datenmengen in Run 3 zurechtkommt. Unter Benutzung der Photonenkonversionsmethode wird der Softwarestand der Photonenanalyse validiert. Dabei werden Daten des Pilot Beams vom Oktober 2021 und die zugehörige Monte Carlo Simulation LHC22c5 verwendet. Im Laufe der Arbeit wurde die bestehende Analysekette durch zusätzliche Tabellen, Histogramme und einer neuen Berechung der Koordinaten des Konversionspunktes ergänzt, als auch Programme für die Datennachbearbeitung geschrieben. Es wurde festgestellt, dass das Detektormaterial in Monte Carlo Simulationen noch nicht vollständig implementiert ist. Weiterhin wurde eine für das Photon Transversalimpulsintervall $0.8\,\mathrm{GeV/c} < p_T < 4.0\,\mathrm{GeV/c}$ durchschnittliche Konversionswahrscheinlichkeit von $p_{conv} = 10.7\,\%$ für den Bereich von $0\,\mathrm{cm} < R < 180\,\mathrm{cm}$ und $p_{conv} = 4.2\,\%$ für $0\,\mathrm{cm} < R < 42\,\mathrm{cm}$ gefunden, wobei R der Abstand in der Transversalebene zum Detekotmittelpunkt ist. Zudem konnte eine Rekonstruktionseffizienz für Photonenkonversionen von $\epsilon_{rec} = 4.76\,\%$ für das Photonen Transversalimpulsintervall von $1.5\,\mathrm{GeV/c} < p_T < 3\,\mathrm{GeV/c}$ bestimmt werden. Die Rekonstruktionseffizienz für das gesamte Photonen Transversalimpulsintervall beträgt $\epsilon_{rec} = 0.42\,\%$. Die räumliche Auflösung des Vertex in der Transversalebene wurde zu $(3.75 \pm 0.09)\,\mathrm{cm}$ und die Auflösung des Transversalimpulses wurde zu $(0.0245 \pm 0.0008)\,\mathrm{GeV/c}$ bestimmt. Durch die neue Berechnung der Koordinaten des Konversionspunktes des Photons konnte eine Verbesserung der Auflösung um Faktor (1.73 ± 0.05) erzielt werden.

Acronyms

SM   Standard Model

CERN   Conseil Européen pour la Recherche Nucléaire

LHC   Large Hadron Collider

Linac 2 Linear Accelerator 2

Linac 4 Linear Accelerator 4

PSB   Proton Synchrotron Booster

PS   Proton Synchrotron

SPS   Super Proton Synchrotron

LS2   Long Shutdown 2

QGP   Quark–Gluon Plasma

QCD   Quantum Chromo Dynamics

ATLAS   A Toroidal LHC ApparatuS

CMS   Compact Muon Solenoid

ALICE   A Large Ion Collider Experiment

TOTEM TOTal Elastic and diffractive cross section Measurement

LHCf   Large Hadron Collider forward

FASER   Forward Search Experiment

LHCb   Large Hadron Collider beauty

MoEDAL Monopole and Exotics Detector at the LHC

ITS   Inner Tracking System

IB   Inner Barrel

OB   Outer Barrel

IL   Inner Layer

ML   Middle Layer

OL   Outer Layer

CYSS   Cylindrical Structural Shell

MFT   Muon Forward Tracker

MAPS   Monolithic Active Pixel Sensors

TPC   Time Projection Chamber

GEM   Gas Electron Multiplier

ROC   ReadOut Chambers

TRD   Transition Radiation Detector

TR   Transition Radiation

O²   Online-Offline

CR1   Counting Room 1

CR0   Counting Room 0

FLP   First Level Processor

EPN   Event Processing Node

CCDB   Condition and Calibration Data Base

FAIR   Facility for Antiproton and Ion Research

DCA   Distance of Closest Approach

Contents

List of Tables

List of Figures

1 | Introduction

To research the fundamental building blocks that make up the universe, the largest particle accelerator and research complex in the world called CERN was founded. One of CERN's main experiments is the ALICE detector, which was put in place to investigate strongly interacting matter at high densities in a state of matter called the Quark–Gluon Plasma (QGP). Characteristics of the QGP can be measured in many ways, one of which is observing the photon spectrum. In order to improve the measurement capability of ALICE several components were upgraded and a new data processing framework was implemented during the Long Shutdown 2 (LS2). The objective for the work in this thesis is to validate the current state of photon measurement using the photon conversion method for the beginning of the Run 3 period and to contribute to the software development in O^2Physics.

In the photon conversion method a photon first converts into an electron-positron pair in the presence of an atomic nucleus. After that, the two particles are measured by the detector and their helical flight path is reconstructed. By combining information of both tracks the conversion point and other parameters of the original photon can be calculated. In contrast to traditional calorimeters the photon conversion method is capable of reconstructing the momentum in all three spacial directions of the photon.

In chapter 2 the theory is briefly outlined and the interest in photon analysis, as well as sources of photons in the collisions are explained. After that the experimental apparatus is described in chapter 3. In chapter 4 interaction processes of photons and electrons with the detector material are clarified. Chapter 5 focuses on the way Monte Carlo simulations and data are processed in the analysis chain, summarizes the code implementation and Monte Carlo and data that was used in the analysis. In chapter 6 the analysis is described. First the implementation of detector material in Monte Carlo simulations is evaluated. After that, the conversion probability of photons is calculated. Following this is the validation of the photon sample purity using cuts. Then the reconstruction efficiency is discussed. Finally the Monte Carlo simulation and data are compared.

2 | ALICE research objective and purpose of photon analysis

First the Standard Model is introduced in section 2.1, which gives a brief overview over the theory and sets the theoretical framework. Then in section 2.2 the Quark Gluon Plasma is described, which makes it clear why there is an interest in photon analysis.

2.1 The Standard Model

For a long time physicists have been trying to establish a complete and mathematically correct description of the universe to make precise predictions about the future and create a starting point for technical advancement. Several groundbreaking discoveries like Newton's laws of motion, the atomic model by Bohr and the quantization of energy by Planck ultimately led to the formulation of the Standard Model (SM) in the 1970s, which today is mostly recognized as our best understanding of the fundamental structure of matter [1]. The SM includes several elementary particles shown in Figure 2.1 and three fundamentals forces, namely the weak interaction, the strong interaction and the electromagnetic interaction. The elementary particles are categorized in quarks, leptons, gauge bosons and the Higgs boson and are further divided into three generations beginning with the most stable ones (first column in Figure 2.1) like the up quark and ending with the most unstable ones like the top quark (third column in Figure 2.1). These particles can form hadronic matter like the proton and the neutron which make up most of our world's visible mass.

The fundamental forces describe how force carriers mediate interactions. The strong interaction uses the gluon, the weak interaction uses W and Z bosons, while the electromagnetic interaction uses photons. In addition to that each force respects different conservation laws.

Even though the SM is our best description of the microworld, it is far from perfect. Despite the best effort, including gravity and general relativity into the SM has proven to be a very difficult task and is one of
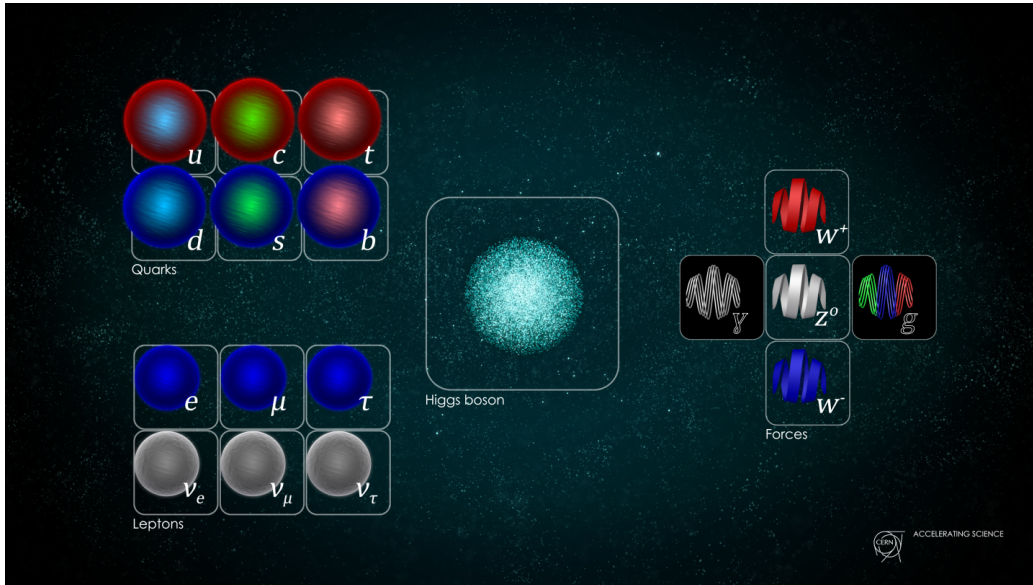
Figure 2.1: SM particles divided in quarks, leptons force carrier particles and the Higgs boson [2].

the biggest challenges in modern physics. It fails to explain the particle-antiparticle asymmetry and doesn't describe neutrino oscillations fully. Furthermore, conservation laws, as well as CPT symmetries are questionable.

2.2 Quark Gluon Plasma

Even though QGP is not of immediate interest in this thesis it should be mentioned and briefly described, since it is the main part of the research plan of ALICE. In addition to that, the photon reconstruction and analysis that is carried out in chapter 6 is done to investigate and observe the QGP in the first place. The QGP is a state of matter defined by an extremely high energy density which makes it possible for quarks and gluons to exist in a deconfined state. These conditions are believed to have existed shortly after the Big Bang and by recreating these conditions, a lot can be learned about the strong interaction and the characteristics of the early universe [3, 4]. In Figure 2.2 one can see the QGP phase diagram.
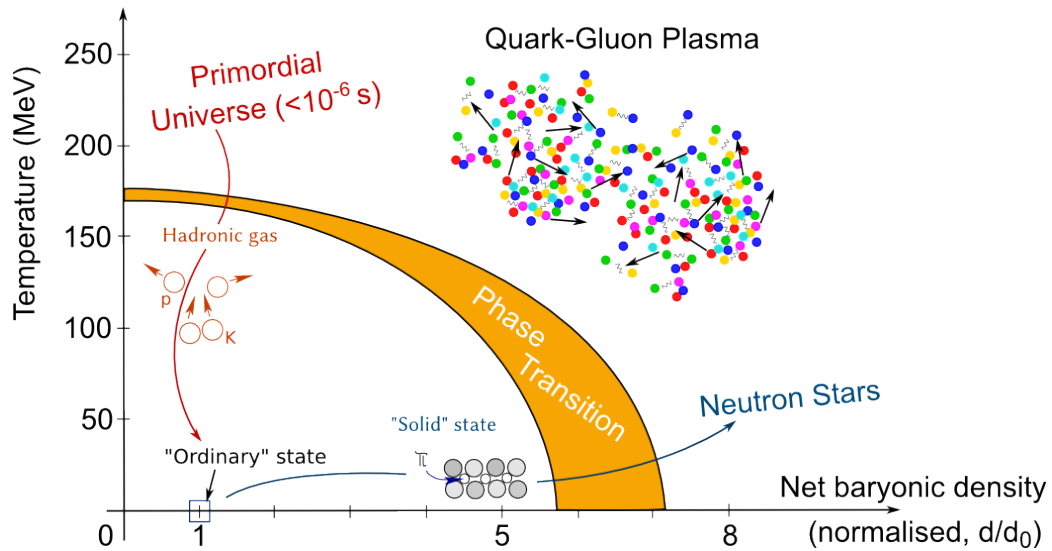
Figure 2.2: QGP phase diagram [5].

In this diagram the state of matter with respect to the temperature and density is drawn. One can see, that the QGP primarily exist at high temperatures, while the hadronic solid state matter primarily exists at low temperatures. Furthermore, the diagram shows that for extremely high net baryonic densities we believe matter transforms into a state similar to a neutron star.

The QGP can be created by heating hadronic matter beyond the Hagedorn temperature of $150\,\mathrm{MeV}$ which corresponds to a temperature in the region of 10^{12} K. The QGP can be produced in an experimental environment by colliding ultrarelativistic heavy ions using particle accelerators like the LHC. The collisions of these ions create fireballs, which expand and cool down creating hadronic matter in the process that is scattered in all directions. The created particles can then be detected by a particle detector. Means for observing the existence of the QGP are e.g. extracting characteristics of jet quenching effects, scattered hadrons and direct photons.

2.2.1 Jet quenching

In high energy collisions partons from the QGP flying in opposite directions can create more parton-antiparton pairs due to confinement when the fireball expands and cools down. These partons can then combine and form particles flying in cone-shaped showers into different regions of the detector. Detecting and tracking these showers makes it possible to reconstruct a single object called jet. Jets passing through a QGP can be influenced by the medium and for example lose energy or gain transverse momentum p_T. These so-called quenching effects can be investigated by analyzing the jets characteristics and have so far been measured in heavy ion collisions [6].

2.2.2 Photons

Photons can come from many different sources at all stages of the collision and may be difficult to detect and interpret due to the high background, but can give a comprehensive insight into the QGP, since they leave the medium unscathed because of their high mean free path length in contrast to the size of the fireball [7]. Furthermore they have the advantage to be produced at all stages of the collision, whereas hadrons only form in a later stage in the hadron gas phase. The stages on the collision can be seen in Figure 2.3.

Photons can be differentiated into decay photons and direct photons, which are all photons that do not come from a decay. In Figure 2.3 one can see both kinds of photons.

Photons from decays

Some of the hadrons produced in the QGP or in jets can decay into photons. By analyzing the photons it is possible to reconstruct the momentum and energy of the original particle and learn more about the particles origin.

13
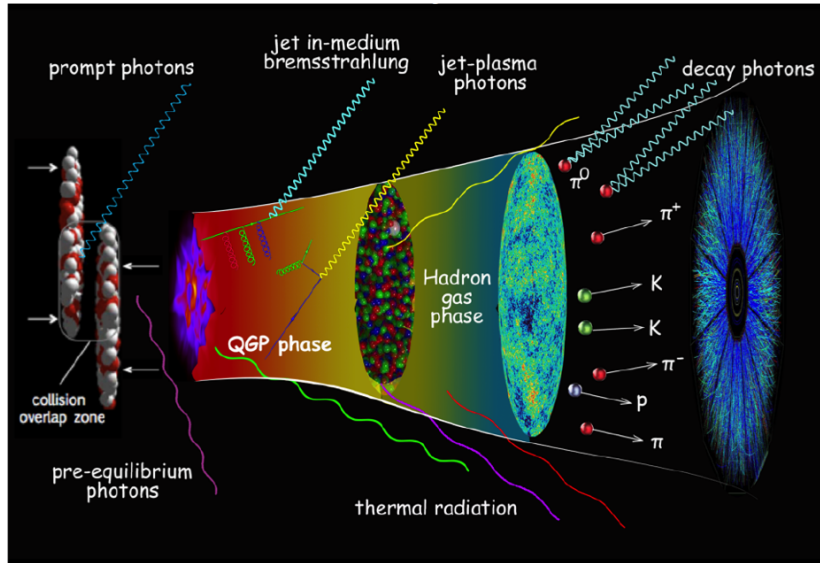
Figure 2.3: Illustration of the dynamical evolution of relativistic heavy-ion collisions. [8]

Thermal photons

One of the most interesting sources of photons are the early phases of the collision, where the QGP forms and the hadron gas phase. Parton scattering inside the fireball and meson-meson or meson-baryon interaction in the hadron gas phase [9] yield a photon spectrum, which reflects the temperature of the QGP [10]. This provides valuable information in the research of all stages of the QGP.

Prompt photons

Another source of photons are photons that are emitted from interactions of colliding nuclei in the initial hard parton scatterings. These photons are mainly produced in quark-antiquark annihilation, Compton scattering and bremsstrahlung [9].

3 | CERN accelerators and detectors

One of the most important tools for particle physics are particle accelerators and detectors. In this chapter I intend to describe the machinery used for producing and collecting of the data, which will serve as a basis for my analysis. The largest research center for particle physics is the Conseil Européen pour la Recherche Nucléaire (CERN) in Geneva, Switzerland, where a succession of particle accelerators is used to accelerate beams of protons or heavy ions to extreme energies and collide them in four collision points. All my data in this thesis is obtained at ALICE, which is one of the detectors located at a collision point at CERN.

In section 3.1 and section 3.2 a broad overview of CERN is given. After that the ALICE experiment is described in detail.

3.1 Large Hadron Collider

The main accelerator, namely the LHC, is the largest particle accelerator in the world with a circumference of 27 km and a maximum depth of up to 175 m beneath the ground at the french-swiss border. It was built as an extension to the other particle accelerators at CERN between 1998 and 2008. The accelerator ring is currently capable of achieving a center of mass energy of 13.6 TeV for proton-proton (pp) collisions and 5.5 TeV per nucleon-nucleon pair for heavy ions with a luminosity of $\mathcal{L} \sim 10^{34}$ cm^{-2}s^{-1} for pp collisions and $\mathcal{L} \sim 10^{27}$ cm^{-2}s^{-1} for heavy ion collisions. Achieving such high energies requires leading edge technology in different fields of science and engineering. For instance, the two beam pipes are kept at ultrahigh vacuum and are surrounded by 1232 dipole magnets for bending and 392 quadrupole magnets for focusing the beams. In order to make the magnets operate properly and at full capacity, they are cooled to a superconducting state at -271.3°C with a state of the art liquid helium cooling system and trained for months to withstand the enormous electrical currents.

15

To accelerate the particles to the desirable energies in the LHC they first have to pass through a sequence of different accelerators, each increasing the velocity of the particles before passing them to the next one. Since 2020 the Linear Accelerator 4 (Linac 4) is the source for all proton beams and accelerates the proton to 160 MeV before passing them to the Proton Synchrotron Booster (PSB). Then they are accelerated to 2 GeV and injected into the Proton Synchrotron (PS), which further accelerates them to 25 GeV. After that, they are passed to the Super Proton Synchrotron (SPS) and then finally injected into the LHC at 450 GeV. A sketch of the CERN accelerators is shown in Figure 3.1.
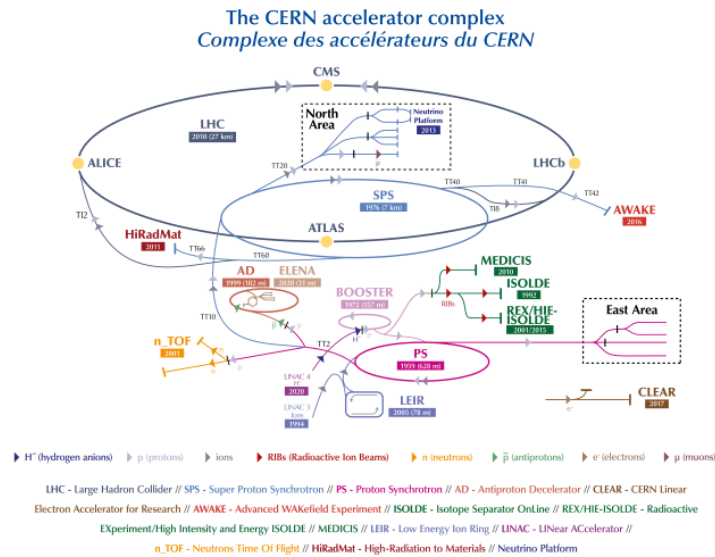
Figure 3.1: The CERN accelerator complex [11].

From December 2018 the operation at CERN was stopped for 3 years, also known as the LS2, to perform major upgrades and maintenance to the LHC injectors. Magnets, beam dumps, solid state power plants as well as extraction systems got replaced. Additionally, as described in the paragraph above, the Linac 4 is now a part of the injection system as CERN's newest machinery and replaced the Linear Accelerator 2 (Linac 2). As a result of the upgraded collision rates, with an emphasis on heavy ions, data rates are increased by up to 100 times [12]. Furthermore the detec-

16

tors located at the interaction points of the LHC took advantage of the opportunity and updated their components as well.

As preparation for Run 3, which started in March of 2022, first pilot beams were injected into the LHC on 19th October 2021 to validate all the components of the accelerator systems and the detectors. In chapter 6 the pilot beam data will be used to carry out a first analysis of the reconstruction efficiency for photon conversions and detector material implementation.

3.2 Detectors at the LHC

The eight interaction points of the LHC ring offer the possibility for installing a wide variety of specialized detectors for different applications and topics of physics. Figure 3.2 gives a brief overview over their location.
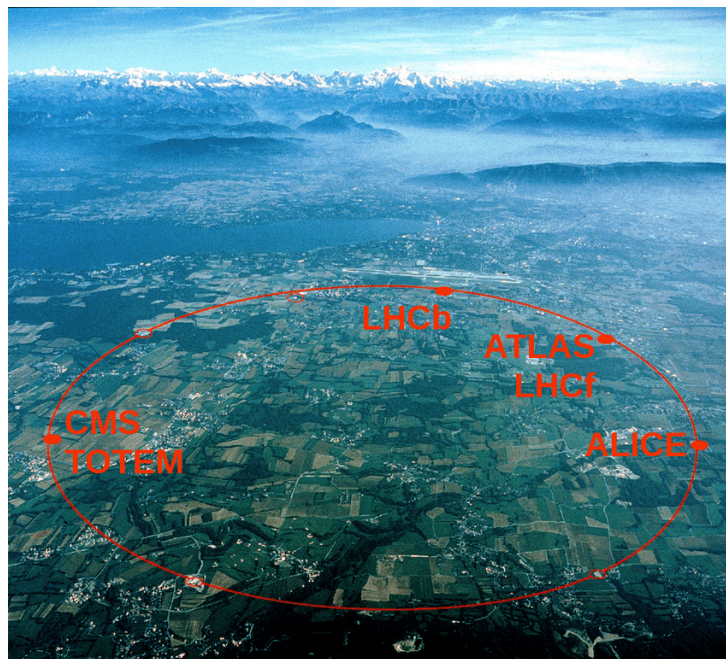
Figure 3.2: Locations of the LHC detectors on the LHC ring [13].

The four biggest experiments at the LHC are A Toroidal LHC ApparatuS (ATLAS), Compact Muon Solenoid (CMS), A Large Ion Collider

Experiment (ALICE) and Large Hadron Collider beauty (LHCb). Furthermore, there are four smaller experiments, namely TOTal Elastic and diffractive cross section Measurement (TOTEM), Large Hadron Collider forward (LHCf), Forward Search Experiment (FASER) and Monopole and Exotics Detector at the LHC (MoEDAL). ATLAS and CMS are general purpose detectors and are primarily used to measure massive particles and were involved in the Higgs discovery. LHCb was primarily designed to study the CP violation in interactions of hadrons containing a bottom quark. TOTEM and LHCf both measure in the forward direction. While TOTEM measures the cross section, elastic scattering and diffraction of particles, LHCf's purpose is to investigate pions. FASER is used to search for weakly interacting particles and MoEDALs primary goal is to search for the magnetic monopole.

The ALICE experiment focuses on the study of strongly interacting matter with the use of heavy-ion collisions. Due to the enormous energy and density of these collisions a fifth state of matter called the QGP gets formed. The QGP is believed to have formed shortly after the Big Bang and is characterized by the fact that quarks exist in a deconfined state [3, 14]. Studying the QGP provides information about the strong interaction and Quantum Chromo Dynamics (QCD). Considering that this thesis uses data from the ALICE experiment, it is inevitable to give a more thorough description of the detector principle, material and geometry in the next section.

3.3 ALICE

ALICE is a collider experiment, which is designed to study heavy ion collisions in which QGP is formed. ALICE stands out for its unique feature to reconstruct tracks of every particle, which grants it its exceptional measuring capability and makes it highly optimized for investigating the QGP. In accordance with the research plan, the collision rate of heavy ion collisions was increased to 50 kHz, which makes it possible to get better statistics for rare events in ALICE. Consequently, several components of the detector had to be replaced to improve the measuring rate.

First, a brief summary of the particle tracking process is given in subsection 3.3.1. After that the center barrel detectors and their upgrades, which are crucial components for the tracking process, are described in subsection 3.3.2, subsection 3.3.3 and subsection 3.3.4 respectively. As a remark it should be mentioned that ALICE is also equipped with calorimeters. But due to the fact that in this thesis the photon conversion method is used, the calorimeters are not needed and thus will not be described.

3.3.1 Tracking of particles

The ALICE experiment is intended to study the QGP and learn more about QCD and the strong interaction by observing particles produced in the QGP. This is done by initially colliding two beams of lead ions, which have been accelerated by the LHC to relativistic velocities. As a result of that, the enormous collision energy facilitates the creation of QGP, where many new particles like e.g. leptons or charmed mesons are created and scattered in all directions. ALICE's goal is to detect, track and analyze these particles using different specialized components, which are arranged in layers around the central beam axis as shown in Figure 3.3. The tracking is mainly done by using the three center barrel detectors, namely the ITS, the Time Projection Chamber (TPC) and the Transition Radiation Detector (TRD). By combining the measurement of each individual component, the trajectory of all produced charged particles can

be reconstructed. Furthermore, ALICE is capable of even reconstructing trajectories of particles with no electric charge, which is impossible with ordinary detectors, by combining the information of measured tracks in order to reconstruct secondary decays. In Figure 3.4 reconstructed tracks inside the ALICE detector are shown.

1 ITS
2 FMD/T0/VO
3 TPC
4 TRD
5 TOF
6 HMPID
7 EMCAL
8 PHOS CPV
9 MAGNET
10 ACORDE
11 ABSORBER
12 TRACKING CHAMBERS
13 MUON FILTER
14 TRIGGER CHAMBERS
15 DIPOLE MAGNET
16 PMD
17 COMPENSATOR MAGNET
18 ZDC
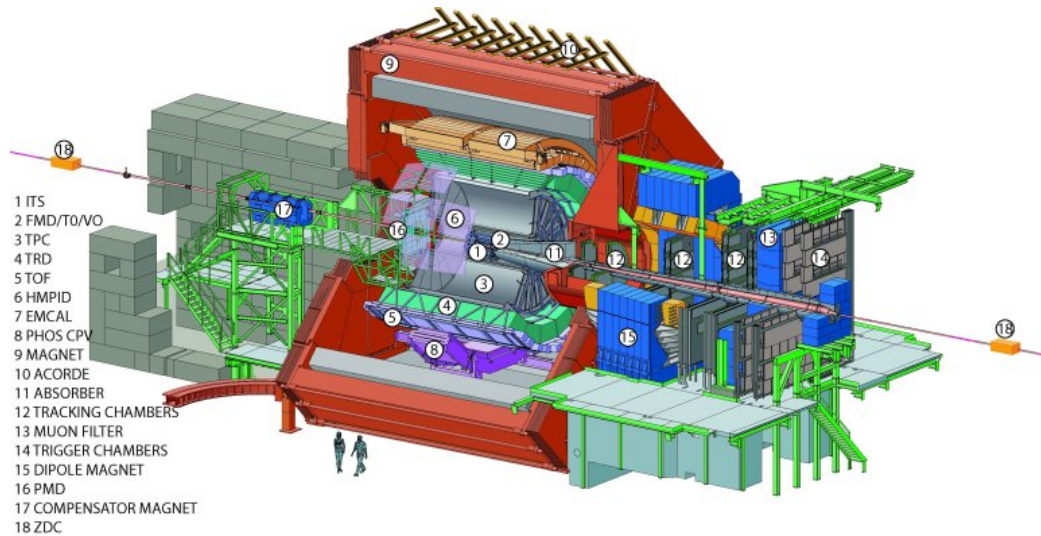
Figure 3.3: ALICE detector [15].
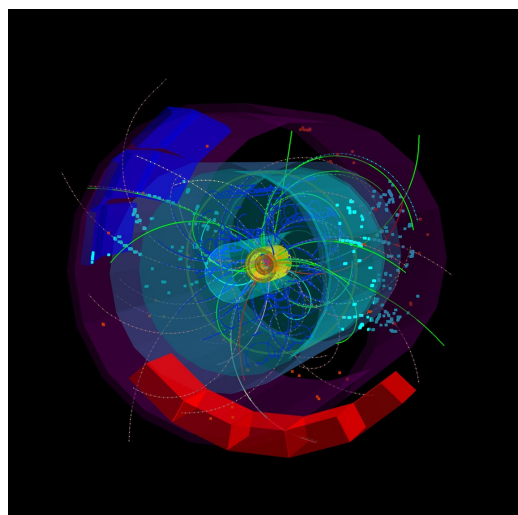
Figure 3.4: Particle tracks inside the ALICE detector from a 7 TeV collision [16].

3.3.2 Inner Tracking System (ITS)

The Inner Tracking System (ITS) is the first detector particles from the primary collision pass through and it's depicted as (1) in Figure 3.3. Its purpose is to determine the primary vertex, reconstruct secondary vertices, use low-momentum particles for tracking and to improve the tracking performance of the TPC.

During the LS2 the ITS was replaced by a better and more sophisticated detector. The new detector, ITS2, has three big improvements. As the first improvement the readout rate of the ITS was increased from 1 kHz to 100 kHz for heavy ion collisions and to 200 kHz for pp collisions. The second improvement is better capacity and higher precision for vertex reconstruction. The resolution of the impact parameter was increased by a factor of 3 in the traverse plane r and ϕ and by a factor of 5 along the beam axis in the z coordinate [17]. As the third improvement the tracking efficiency was increased due to the better silicon chips and more layers. Together, the better tracking efficiency, improved vertex reconstruction and higher collision rate yield a significantly improved high-precision measurement of the low momentum range and a better read out rate.

To achieve the described improvements the new detector has major changes in geometry, silicon chip design and readout electronics. Figure 3.5 shows the new ITS2 geometry.
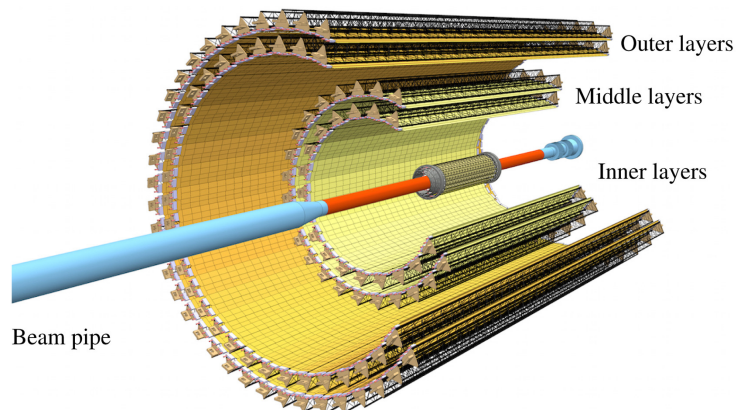
Figure 3.5: Silicon chip layers of the ITS2 with beamline in the center [18].

ITS2 consist of 7 layers of silicon pixel detectors. The Inner Barrel (IB) consist of three layers with the innermost starting at a distance of 23 mm from the interaction point. As a result of the short distance between interaction point and innermost layer, the beamline had to be redesigned and narrowed down. The Outer Barrel (OB) is made up by the Middle Layers (MLs) and the Outer Layers (OLs), which stretch from 198 mm to 395 mm. Table 3.1 summarizes the layer radii of the detector and Table 3.2 summarizes the location of structural components.

Layer No.	R_{min} [mm]	R_{max} [mm]
0	22.40	26.70
1	30.10	34.60
2	37.80	42.10
3	194.40	197.70
4	243.90	247.00
5	342.30	345.40
6	391.80	394.90

Table 3.1: Radii of the different silicon chip layers of the ITS2 [18].

Component	R [mm]
Support cones middle barrel	285
Support cones outer barrel	433
Cylindrical Structural Shell (CYSS)	455
ITS-Muon Forward Tracker (MFT) cage	545

Table 3.2: Structural components of the ITS2 [18].

ITS2 uses 12.5 billion pixels, resulting in an area of about $10\,\text{m}^2$. The new ALPIDE chip consist of CMOS Monolithic Active Pixel Sensors (MAPS), which makes it possible to reduce the material budged of the Inner Layer (IL) to 0.35 % X_0 and OL to 0.8 % X_0. In addition to that, the new MAPS has a significantly reduced pixel size of 29.24 µm × 26.88 µm, which is

mostly responsible for the better resolution of the detector. The ALPIDE chip is able to cover a pseudo-rapidity of $\eta < 1.3$. Using pixel masking a fake hit rate of less than 1×10^{-8} can be achived. Furthermore preliminary results show a detection efficiency of about 99 % [19].

3.3.3 Time Projection Chamber (TPC)

The Time Projection Chamber (TPC), shown in Figure 3.3 as (3), is the main device responsible for tracking and identifying the charged particles. Its radius stretches from 85 cm to 250 cm and it is 500 cm long, excluding the readout chambers at the edges. Furthermore the TPC is separated by a large circular HV electrode into two equally big parts shown in Figure 3.6. Particles originating from the collision pass through one of the two large volumes filled with a gas mixture, consisting of Ne-CO_2-N_2 (85.7 : 9.5 : 4.8) [20]. Charged particles ionize the gas and leave a trace of electrons, which are then accelerated towards the end caps of the TPC by the HV electrode.

Figure 3.6: Schematic sketch of the ALICE Time Projection chamber [21].

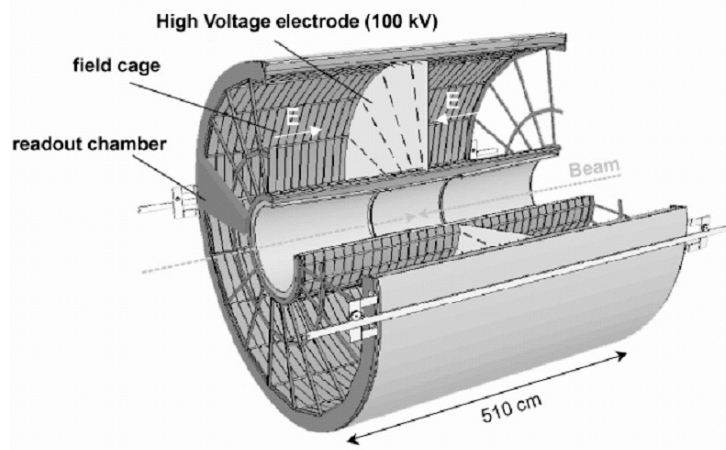In accordance with the change to a 50 kHz collision rate the TPC was also upgraded. Fundamental changes to the way data is read out were made, since the old trigger based system is too slow and a continuous

readout is necessary [20]. To meet these requirements the upgraded TPC is now using Gas Electron Multiplier (GEM) [22], which not only provides the demanded continuous readout of the data, but also have excellent ion blocking and sufficient dE/dx resolution. GEMs are essentially electron multipliers, that are capable of handling a continuous stream of charges. Avalanches of electrons originating at the GEMs hit the readout chambers, where a signal is induced and processed. In the ALICE experiment GEMs are placed in trapezoidal frames called ReadOut Chambers (ROC) at the end caps of the TPC. The ROCs consist of 4 GEMs sequentially arranged with different voltages applied across them. Moreover some optimization strategies like producing GEMs with different hole sizes are used to further optimize the ROC with respect to ion blocking, gain and resolution. The working point used at ALICE is defined by an ion backflow of 0.7 %, resulting in an energy resolution of 12 % $\sigma(^{55}Fe)$ at worst.

3.3.4 Transition Radiation Detector (TRD)

The Transition Radiation Detector (TRD) is a component of the ALICE central barrel and primarily provides electron and positron identification and triggering. Additionally, it contributes to the track reconstruction resulting in a resolution that is up to 40 % better than without the TRD information and is also used to calibrate space charge distortions in the TPC. It is represented as (4) in Figure 3.3.

When a charged particle at relativistic velocity crosses a boundary between two different media, Transition Radiation (TR) occurs. It is a suitable principle of measuring the particle's velocity by observing the particle's scattering angle. Measuring TR works especially well for electrons and hadrons in a momentum range between 1 GeV and 100 GeV, hence a TR detector (TRD) is used in the ALICE experiment.

The TRD used in the ALICE experiment fully encloses the beam line in azimuth, dividing it into 18 sectors. Furthermore, it is composed of five stacks of detectors along the beamline. Each stack consists of six layers, resulting in 540 detectors in total with a radius between 2.90 m and 3.68 m
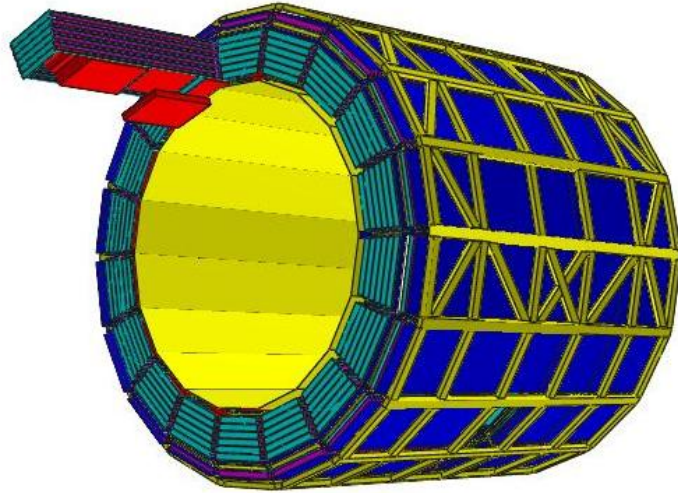
Figure 3.7: Schematic sketch of the ALICE Transition Radiation Detector [23].

and a length in longitudinal direction of 7 m like shown in Figure 3.7. The TRD covers a pseudo-rapidity range of $-0.84 < \eta < 0.84$. Using this many detectors is necessary to get a good resolution, since TR photons are rare and only 0.8 photons on average are detected at a velocity of $\gamma \approx 2000$, where γ is the Lorentz factor.

Besides measuring the velocity the TRD in ALICE is used to differentiate electrons and positrons from other charged particles at momenta above 1 GeV. This is done using the fact that electrons and positrons produce TR and have a higher ionization energy loss dE/dx than other charged particles. A TRD chamber is schematically depicted in Figure 3.8. One can see that the electron ionizes the material in the drift chamber and emits a TR photon, while the pions only ionizes the material. In Figure 3.9 the average pulse height as a function of time is shown. There are two important observations to be made: 1. The energy loss dE/dx of the electron is significantly higher than the energy loss dE/dx of the pion. 2. Including the TR, the pulse height rises over time for the electron resulting in an even better differentiation and discrimination of electrons and pions.
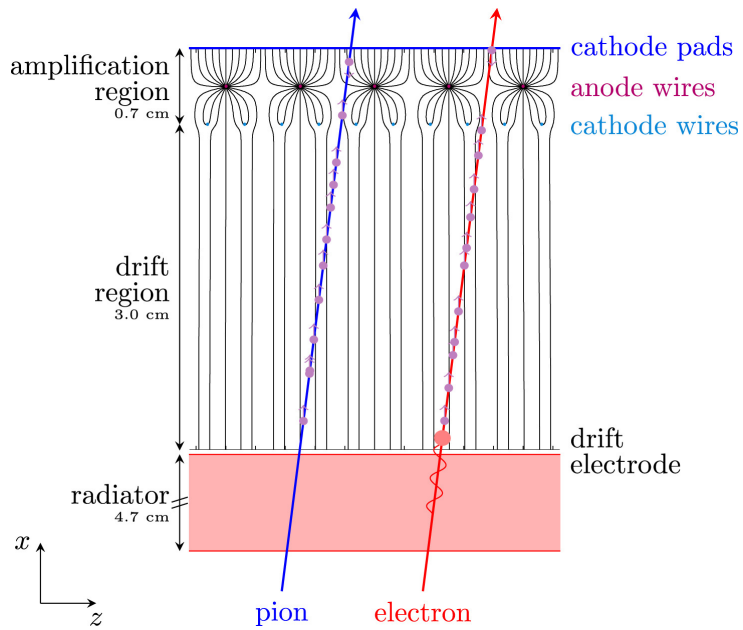
Figure 3.8: π and e^- pass through the TRD [24].
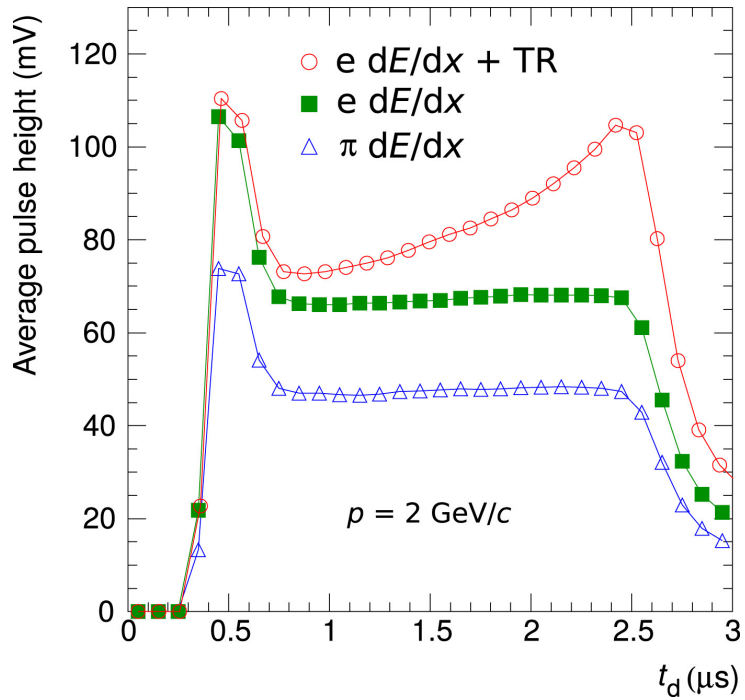
Figure 3.9: Pulse height spectrum of the TRD as a function of time [24].

4 | Interaction processes of photons and electrons

This chapter contains the description of interaction processes of photons and electrons with the detector material. In section 4.1 the interaction between photons and matter is explained. After that, in section 4.2 the processes of how electrons interact with the detector are described.

4.1 Interaction of photons with matter

A photon γ cannot be directly detected, hence we have to rely on interaction processes between photons and matter and detect the resulting products, which are usually electrons. The most common interaction processes are: Rayleigh scattering, photoelectric effect, Compton scattering and Pair-conversion [25]. Since Rayleigh scattering describes a fully elastic effect that provides no possibility of detecting the photon and additionally only occurs for low energies, it will be neglected in the further discussion.
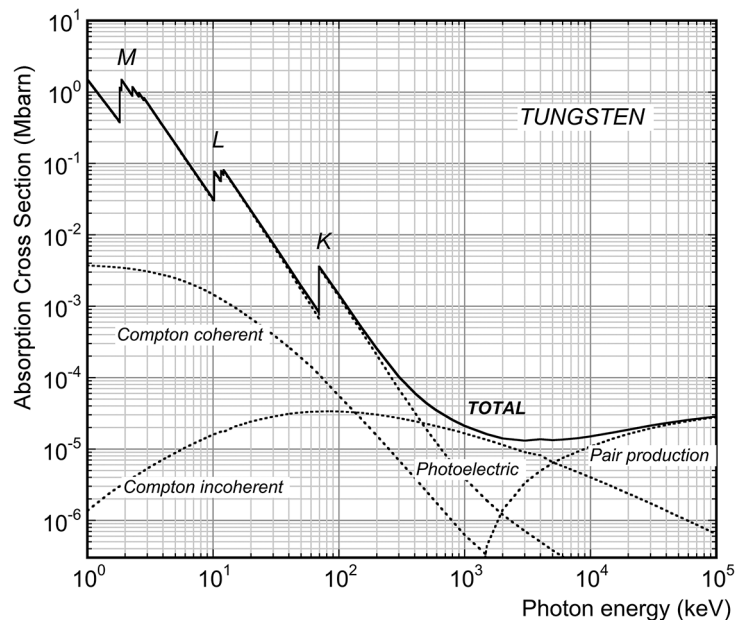
Figure 4.1: Cross section of interaction processes of photons with matter (tungsten) as a function of the energy of the photon [26].

In Figure 4.1 one can see the individual and total cross section of three interaction processes between photons and matter depending on the photon energy. One can clearly see that the photoelectric effect dominates the region below 10^2 keV. In the region from 10^2 to 10^4 keV all processes are relevant for the total cross section, but the main contributor at around 10^3 keV is Compton scattering. For energies above 10^4 keV pair production is the sole contributor.

4.1.1 Photoelectric effect

In the photoelectric effect a photon is fully absorbed by an electron from one of the atoms shells, which is then emitted. The interaction is illustrated in the Feynman diagram in Figure 4.2.
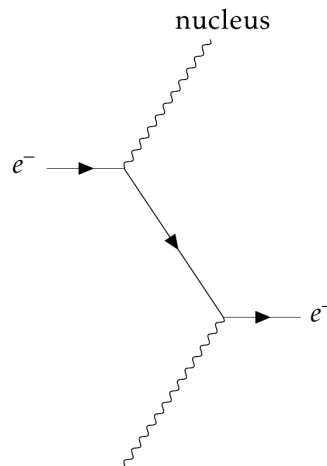
Figure 4.2: Feynman diagram of the photoelectric effect.

The photoelectric effect can only exist if:

$$E_b < h \cdot f \tag{4.1}$$

where E_b is the binding energy of the electron to the atom, h the Planck constant and f the frequency of the photon. If the energy of the photon is higher than the binding energy E_b of the electron, the excess energy is converted into kinetic energy as illustrated by the energy conservation:

$$h \cdot f = E_b + E_{kin} \tag{4.2}$$

28

The total cross section σ_{ph} consists of the sum of cross sections of all the individual electrons in the atom, with the main contributor being the cross section of the electron in the K-shell. For relatively small photon energies E_γ, the cross section strongly depends on the energy of the photon:

$$\sigma_{ph} \propto Z^5 \cdot \left(\frac{m_e \cdot c^2}{E_\gamma}\right)^{\frac{7}{2}} \tag{4.3}$$

where Z is the atomic number, m_e the electron mass and c the speed of light, while for larger E_γ the cross section flattens [25]:

$$\sigma_{ph} \propto \frac{Z^5}{E_\gamma} \tag{4.4}$$

4.1.2   Compton scattering

The Compton effect describes an interaction of a photon with an electron, but unlike the photoelectric effect Compton scattering occurs even without any nucleus present. Furthermore, as a consequence of energy and momentum conservation the absorption of the entire photon is forbidden, as one can see in the Feynman diagram in Figure 4.3.
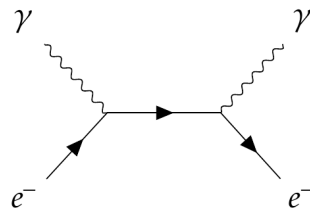
Figure 4.3: Feynman diagram of the Compton effect.

Rather than annihilating the photon, the two exchange energy according to:

$$\lambda_f = \lambda_i + 2 \cdot \lambda_c \cdot \sin^2\left(\frac{\varphi}{2}\right) \tag{4.5}$$

where λ_f is the final wavelength of the γ after the interaction, λ_i is the initial wavelength, λ_c is the Compton wavelength and φ is the scattering

angle. The cross section σ_c of Compton scattering is roughly given by:

$$\sigma_c \propto \frac{Z}{E_\gamma} \tag{4.6}$$

4.1.3   Pair production

For highly energetic photons the third possible interaction with matter is pair production, where the photon transforms into an electron-positron pair in the presence of an atomic nucleus. Figure 4.4 shows one of the possibilities a pair production can occur. Due to energy conservation laws this interaction can only happen if the photon exceeds the minimum rest mass of the electron-positron pair:
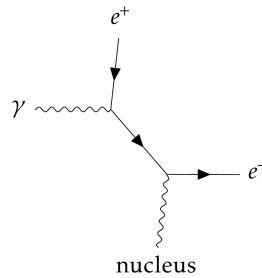
Figure 4.4: Feynman diagram of the pair conversion.

$$E_\gamma > 2 \cdot m_e \cdot c^2 \tag{4.7}$$

Using approximation the formula for the differential cross section is given by:

$$\frac{\mathrm{d}\sigma_p}{\mathrm{d}x} = \frac{A}{X_0 N_A}\left[1 - \frac{4}{3}(1-x)\right] \tag{4.8}$$

where A is the atomic number, X_0 is the radiation length, N_A is the Avogadro constant and x is given by:

$$x = E/k \tag{4.9}$$

where E is the energy of the electron or positron and k the energy of the photon. In Figure 4.5 the normalized differential cross section for different

30

photon energies is shown. It is immediately apparent, that the differential cross section is symmetric in x.
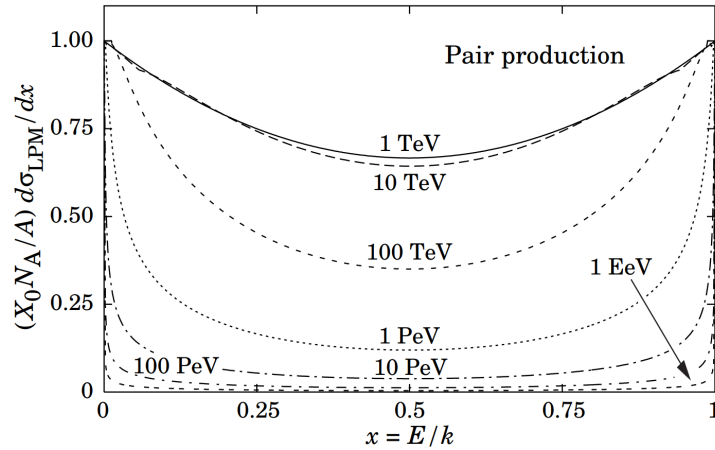
Figure 4.5: The normalized pair production cross section dσ_{LPM}/dx, versus fractional electron energy $x = E/k$ [27].

The high energy limit for the total cross section of the pair production is:

$$\sigma_p = \frac{7}{9}\left(\frac{A}{X_0 N_A}\right) \tag{4.10}$$

In practice Equation 4.10 is very accurate for photon energies higher than 1 GeV [27].

4.2 Interactions of electrons with detector material

All of the interactions that were described in section 4.1 resulted in electrons. By detecting these electrons and analyzing them we can deduce the characteristics of the original photon, like the momentum and the conversion point. Moreover, photons that are detected with the conversion method have directional information of the momentum. This section focuses on the mechanisms that are used in the ALICE experiment to detect electrons.

4.2.1 Ionization

Charged particles traversing through matter ionize electrons from atoms and lose energy in the process, which is known as energy loss by ionization. The energy loss is described by the Bethe-Bloch formula [28]:

$$\frac{\mathrm{d}E}{\mathrm{d}x} = Kz^2\frac{Z}{A}\rho\frac{1}{\beta^2}\left[\frac{1}{2}\ln\left(\frac{2m_ec^2\beta^2\gamma^2 T_{max}}{I}\right) - \beta^2 - \frac{\delta}{2}\right] \qquad (4.11)$$

where Z is the atomic number, z is the charge of the traversing particle, β is the velocity of the traversing particle, ρ the density of the material, I the mean excitation energy of atoms and $\delta/2$ the density correction. Furthermore, K/A is given by:

$$\frac{K}{A} = \frac{4\pi N_A r_e^2 m_e c^2}{A} \qquad (4.12)$$

where N_A is the Avogadro constant, r_e the classical electron radius and A the weight of the atom. The maximum energy transfer in a single collision T_{max} can be approximated by:

$$T_{max} \approx 2m_ec^2\beta^2\gamma^2 \qquad (4.13)$$

It was shown, that the mean excitation energy can be approximated by:

$$I = (10\,\mathrm{eV})\cdot Z \qquad (4.14)$$

where Z is the atomic number. Furthermore, one can substitute β by

$$\beta = \frac{p}{\gamma M c} \qquad (4.15)$$

where M is the mass and p the momentum of the traversing particle. From this substitution it should be clear that different particles will result in different shapes of the Bethe Bloch function. By measuring momentum and energy loss of the particle it is possible to perform a particle identification. This particle identification method will be used in section 5.4 to check the validity and the quality of the performed cuts, which are used to filter electrons from other charged particles like pions.

4.2.2 Bremsstrahlung

Bremsstrahlung occurs when charged particles get decelerated in the electric field of nuclei. Due to energy conservation the lost kinetic energy is converted into radiation in the form of photons. This produces a continuous spectrum of mostly X-ray photons. Bremsstrahlung is primarily important for electrons and positrons in the range of up to a few hundred GeV, since the energy loss of the particle is proportional to E/m^2 [29]. The energy loss function for bremsstrahlung at large energies is:

$$\frac{\mathrm{d}E}{\mathrm{d}x} = \frac{E}{X_0} \tag{4.16}$$

where $\frac{\mathrm{d}E}{\mathrm{d}x}$ is the energy loss of the electron per length, E is the energy of the electron and X_0 is the attenuation length. From this formula one can see that the electron loses energy exponentially the further it travels in the material.

4.2.3 Transition radiation

Ultrarelativistic charged particles with an energy in the range of 1 GeV and 100 GeV produce electromagnetic radiation, when crossing the border between two dielectrics, having different refraction indices. The energy of the produced radiation is in the region of 5 - 15 keV and peaks at an angle of:

$$\theta = \frac{1}{\gamma} \tag{4.17}$$

Transition radiation can be used to produce electrons through processes described in section 4.1, which can be used to measure the angle for the maximum intensity and possibly the deposited energy. Given that the energy of transition radiation is rather small the electrons originate mainly from the photoelectric effect. Finally, it should be mentioned that the number of radiated photons when passing through the border of two materials is very small, thus detectors like the TRD in the ALICE experiment use several layers of material to increase the quantity TR photons and therefore the quality of the measurement.

5 | Data and Monte Carlo analysis chain

In this chapter the processing of data, Monte Carlo and the samples that are used in the analysis are described. The first section focuses on the way and the tools that are used to process the data. Then in section 5.2 the V^0 finder algorithm and the recalculation of the conversion point coordinates are described. After that, in section 5.3 the data sets that are used in the analysis are listed. Finally, in section 5.4 the cuts for filtering electrons and photons from other particles are explained.

5.1 Online-Offline data and Monte Carlo processing framework

The main goal of the upgrades for Run 3 were to increase the collision rate to 50 kHz for Pb–Pb collisions and to 200 kHz for pp collisions, in order to have better statistics for rare events. As a result of the increased collision rates the amount of data increased 100 times and thus the previous data processing system is insufficient, since a continuous readout is required. The TPC for instance would suffer from charge pile ups in the readout electronics and would be rendered useless as a consequence.

The new solution for accommodating huge amounts of data combines online and offline computing to a system called Online-Offline (O²). In Figure 5.1 the data flow from ALICE is shown and briefly summarizes the facilities involved in the data analysis.
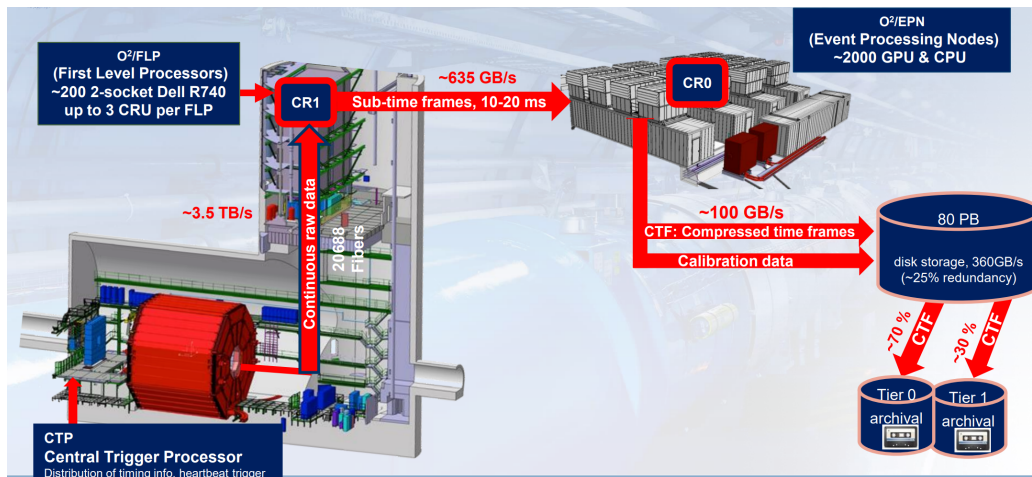
Figure 5.1: Data flow in the ALICE experiment for Run3 [30].

One can see that first all the raw data from the readout electronics is transported to the Counting Room 1 (CR1) via a 3.5 TB/s data stream. The CR1 accommodates the First Level Processors (FLPs), which consist of CPU cores and hardware accelerators like FPGAs. This hardware runs cluster finder algorithms and starts with the synchronous reconstruction process, reducing the amount of data by ~2.5 and organizes the data by time frames of 20 ns. Then the data is forwarded to the newly constructed Counting Room 0 (CR0), where the Event Processing Nodes (EPNs) are located. Due to the high load GPUs are used instead of CPUs for better parallelized processing power, where one GPU approximately replaced 30 CPU cores. In total about 2000 GPUs are used to finish the analysis, the global reconstruction and tracking of the data. Finally, the data is further compressed and then directed to its decentralized storage location on the GRID, where approximately 60 TB/year are stored.

In total the data is reduced by about a factor of 20 [31]. This high compression rate is necessary primarily for the data of the TPC, since it makes up 95 % of the total data. In addition to that it should be mentioned that the calibration is done online during the synchronous processing to avoid additional sweeps over the raw data, which eliminates the need to store or buffer it. The calibration objects are then created in an intermediate

step between synchronous and asynchronous processing and stored in the Condition and Calibration Data Base (CCDB).

5.1.1   Composition of the O^2 software

The analysis software can be separated into several libraries and frameworks, where each library and framework is dedicated to a certain task. The composition of the software can be seen in Figure 5.2.
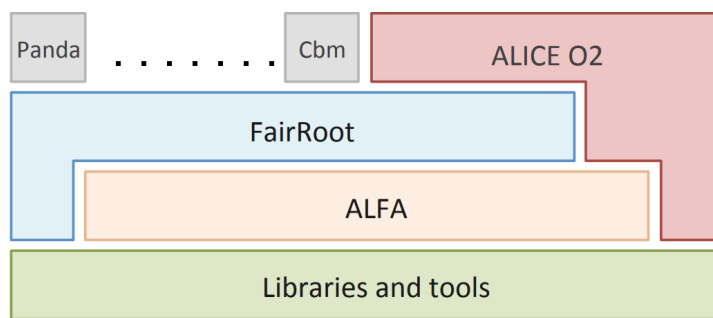
Figure 5.2: O2 software ecosystem [32].

The foundation for the O² software lies in the libraries and tools used for basic calculations and programming, like CERN ROOT and CMake. ALFA is a concurrency framework from ALICE and FAIR, that provides coordination in multithreaded data processing components as well as a messaging framework called FairMQ. FairRoot offers an abstraction layer for the storage. Finally, ALICE O² provides all the necessary algorithms and core functionality for the data analysis and reconstruction. It was recently split into O^2 and O^{2}Physics, where O^{2}Physics contains all the user code for the analysis.

5.1.2   Reconstruction of tracks and particles

The steps of data reconstruction during synchronous processing are depicted in Figure 5.3.

On the left side of the figure the local clustering and tracking of individual components is shown. The produced data is then used to start
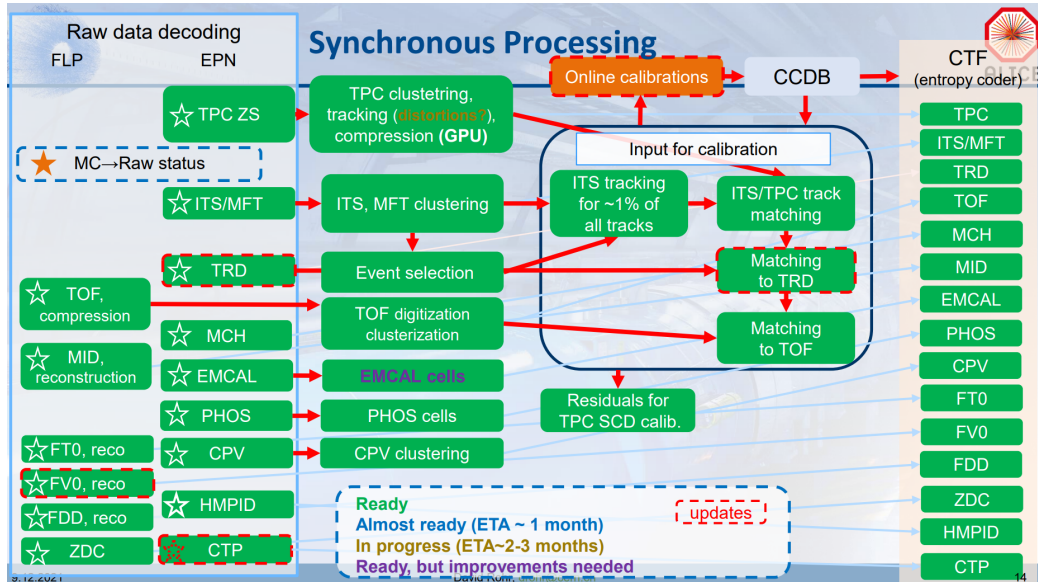
Figure 5.3: The reconstruction steps are shown from local reconstruction to global reconstruction to the final analysis data. The shown progress corresponds to 21.12.2021 [30].

matching the tracks that were reconstructed by different components of ALICE. First the ITS and TPC tracks are matched, then the TRD tracks and finally the TOF matching is performed. Furthermore, the construction of the calibration objects is shown in the top of the figure.

5.2 Reconstructing V^0s from positive and negative tracks

Charged particles can be tracked using the three central barrel detectors of the ALICE experiment as described in section 3.3. These tracks can be used to search for and reconstruct V^0s, which are neutral particles that cannot be detected directly like e.g. γ, K_S^0, Λ and $\overline{\Lambda}$. The reconstruction of V^0s begins with the matching of tracks. First an arbitrary track with a large enough impact parameters b is chosen. Then all the tracks of oppositely charged particles are matched with this track. Through various

selection criteria and algorithms matching pairs of tracks are created as shown in Figure 5.4.
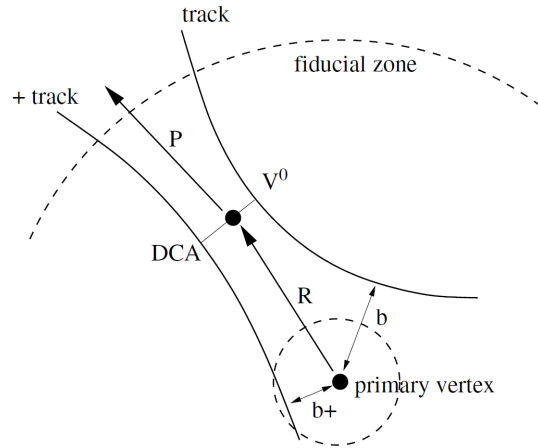
Figure 5.4: Geometrical selections for secondary vertex reconstruction [33].

Selection criteria for matched tracks and reconstructed V^0s are e.g.:

- Impact parameter b large enough. This impact parameter corresponds to the distance between track and primary vertex.

- Distance of Closest Approach (DCA) is smaller than a given value between the two tracks

- vertex is inside fiducial volume

- momentum of the V^0 points back to the primary vertex

5.2.1 Recalculating the photon conversion point

At the ALICE experiment we deal mostly with photons in an energy region of MeV or higher, thus pair conversion is the dominant interaction process and the others are negligible. This means, that the V^0 reconstruction method will in theory be able to reconstruct a big portion of the photons from the QGP or particle decays. Since V^0s can correspond to different particles the V^0 finder algorithm has to be as generic as possible

for the sake of maximizing the reconstruction efficiency for every particle. Consequently, some properties of certain decays have to be overlooked, because they might conflict with other decays. When calculating the conversion point of the photon conversion this causes the resolution to be worse than theoretically possible. Knowing this, an additional recalculation for the coordinates of the conversion point was implemented in the analysis chain. The mathematical foundation for this recalculation will be discussed in this section.

In pair conversion with high energy photons the momenta of the electron and positron are almost parallel at the conversion point due to energy and momentum conservation. This opens up the possibility to use the parameters of the helical flight path of the electron and positron to improve the spacial resolution of the conversion point. The rough idea is to deduce the position of the V^0, which is represented by the black dot in Figure 5.4, by calculating the intermediate point between the points, where the tracks are closest. Therefore the helix centers are determined and then the mean is calculated.

First of all it should be noted that all calculation happen in a local frame of reference with respect to one of the 18 GEM elements in the TPC. Figure 5.5 shows the relation between the local and global coordinate system.
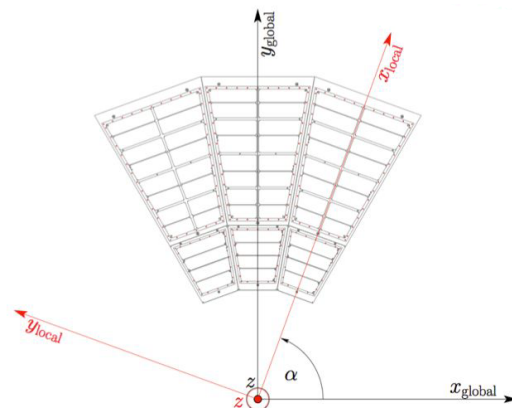
Figure 5.5: Relation between global and local coordinate system [34].

Points between the two coordinate systems can be transformed using the following relations:

$$x_{\text{global}} = x_{\text{local}} \cdot \cos{(\alpha)} - y_{\text{local}} \cdot \sin{(\alpha)} \qquad (5.1)$$

$$y_{\text{global}} = x_{\text{local}} \cdot \sin{(\alpha)} + y_{\text{local}} \cdot \cos{(\alpha)} \qquad (5.2)$$

Further calculations will be based on the local coordinate systems. After the calculations are done, results are transformed to the global coordinate system.

The calculation of the helix centers is based on Figure 5.6, where the track is indicated by the solid black line. From this we calculate the helix center:

$$x_{hc} = x_{ftp} - \sin{(\varphi)} \cdot r_h \qquad (5.3)$$

$$y_{hc} = y_{ftp} + \cos{(\varphi)} \cdot r_h \qquad (5.4)$$

where x_{hc} and y_{hc} refer to the coordinates of the helix center, x_{ftp} and y_{ftp} give the coordinates of the first tracked point, φ describes the angle between the x-axis and the momentum vector at the first tracked point and r_h is the radius of the helix. Note that variables are signed depending on the charge of the track's particle.

Figure 5.6: Track of a charged particle in the local coordinate system of a GEM [34].

In order to get the coordinates of the recalculated conversion point the middle point between the helix of the positively and negatively charged

40

particle is determined:

$$x_{rc} = \frac{x_{hc,pos} \cdot r_{h,neg} + x_{hc,neg} \cdot r_{h,pos}}{r_{h,neg} + r_{h,pos}} \qquad (5.5)$$

$$y_{rc} = \frac{y_{hc,pos} \cdot r_{h,neg} + y_{hc,neg} \cdot r_{h,pos}}{r_{h,neg} + r_{h,pos}} \qquad (5.6)$$

where rc represents coordinates of the recalculated conversion point.

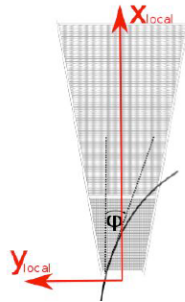Finally it is necessary to recalculate the Z coordinate of the conversion point. For this we first want to get the point on the track in the transverse plane that is closest to the recalculated conversion point in the transverse plane. The angle α_{pos} and α_{neg} between the x-axis and the vector of this point can be calculated with:

$$\alpha_{pos} = \pi + \text{atan2}\left(-y_{rc} - y_{hc,pos}, x_{rc} - x_{hc,pos}\right) \qquad (5.7)$$

$$\alpha_{neg} = \pi + \text{atan2}\left(-y_{rc} - y_{hc,neg}, x_{rc} - x_{hc,neg}\right) \qquad (5.8)$$

Note that α_{pos} and α_{neg} are not related to the angle of coordinate transformation α. In order to calculate the closest point on the track to the conversion point in the transverse plane these two equations are used:

$$x_{v,pos} = x_{hc,pos} + r_{h,pos} \cdot \cos\left(\alpha_{pos}\right) \qquad (5.9)$$

$$y_{v,pos} = y_{hc,pos} + r_{h,pos} \cdot \sin\left(\alpha_{pos}\right) \qquad (5.10)$$

Similarly, the coordinates of the point are calculated with the respective variables for the track of the negatively charged particle. After that the Track Propagation algorithm is applied to $x_{v,pos}$, $y_{v,pos}$, $x_{v,neg}$, $y_{v,neg}$ and the respective tracks and calculates the best Z coordinate on the tracks for the conversion point. Finally, the weighted mean is calculated:

$$z_{rc} = \frac{z_{pos} \cdot r_{h,neg} + z_{neg} \cdot r_{h,pos}}{r_{h,neg} + r_{h,pos}} \qquad (5.11)$$

5.3 Data and Monte Carlo

5.3.1 Used datasets

The analysis in chapter 6 is carried out using Pilot Beam data of October 2021 and LHC22c5 Monte Carlo, which are pp collisions at 900 GeV. Furthermore, several other datasets were analyzed, which differ mainly in the collision energy and in the number of collisions. Plots and diagrams for them can be found in the appendix. For each dataset a dedicated Monte Carlo simulation with the same collision energy is chosen, in order to compare the results. In addition to that the Monte Carlo can be used to validate the state of the implementation of the detector in the O^2 software. It should be noted, that only pp collisions were analyzed and no attention was dedicated to Pb–Pb collisions, since these types of collision were not available yet for Run 3. In Table 5.1 the used datasets and Monte Carlo simulations are summarized.

5.3.2 Objective of analysis

After the completed upgrades to the LHC injection system and detectors during LS2 a first test in October of 2021 was performed. On the 19th of October 2021 first pilot beams were circulating at the LHC. This was followed up with low intensity collisions at an injection energy of 450 GeV on the 26th of October 2021 and stable collisions were performed on the 27th October 2021 [35]. The data from this pilot beam is used to check the performance of photon measurements in the upgraded ALICE experiment and especially the data processing framework, since the software is still under construction as it was built from scratch.

Tag	Run numbers	Pass	Date	Collision energy [GeV]	#collisions	#reconstructed photons
Data						
LHC22c	519041 - 519908	1	May / June 2022	900	11 217 426	492
LHC22d	518541 - 518547	1	May / June 2022	900	618 031	27
LHC22e	517616 - 517767	1	May / June 2022	900	-	-
PilotBeam	505548 - 505673	5	Oct 2021	900	20 901 975	9984
Monte Carlo						
LHC22c5	505548 - 505673	4		900	860 697	2086
LHC21k6	302044 - 302053	2		13 000	600 486 854	1 758 829

Table 5.1: Properties of the datasets and Monte Carlo simulations used in the analysis. Only pp collisons.
LHC22e cannot be used in analysis yet due to missing calibration files.

5.3.3 Analysis chain

The analysis in chapter 6 was carried out using the O² framework and CERN ROOT. Data and Monte Carlo were processed and skimmed using the following O² and O² Physics tasks:

- *trackselection*

- *fdd-converter*

- *event-selector*

- *multiplicity-table*

- *timestamp*

- *trackextension*

- *lf-lambdakzerobuilder*

- *pid-tpc*

- *skimmerGammaConversions*

- *gammaConversions*

The first six tasks and the *pid-tpc* task are helper tasks that provide generic information on collisions, tracks and Monte Carlo information as tables. In the *lf-lambdakzerobuilder* tables of V^0s are constructed. After that in the *skimmerGammaConversions* task collisions, V^0s and tracks are associated and tables with information on the reconstructed V^0s are build. Additionally, the recalculation of the conversion point is performed here. Finally the resulting tables are evaluated and the data is put into histograms by the *gammaConversions* task. This analysis chain is performed for both Monte Carlo simulations and data sets and can be regarded as the analysis chain that provides information on the reconstruction of the V^0s.

In addition to the previous analysis chain, Monte Carlo simulations are processed by an additional analysis chain that consists of *skimmerGamma-ConversionsTruthOnlyMC* and *gammaConversionsTruthOnlyMC* in order to

extract all the parameters of all the generated photons, like number of generated photons and number of converted photons.

5.3.4 Modified tasks and tables

In the course of the thesis parts of *skimmerGammaConversions*, *gammaConversions*, *skimmerGammaConversionsTruthOnlyMC* and *gammaConversionsTruthOnlyMC* were modified and added. In this section my personal contribution and additions are explained.

As already mentioned the analysis chain uses many tables that are first created in helper tasks and then processed and put into different, more compact and useful tables by the user tasks. One should differentiate between MCTrue, MCVal, Rec and MCTruthOnly. MCTrue uses the true Monte Carlo information of the generated particle to reconstruct the V^0, while Rec uses "measured" data in Monte Carlo simulations and real data to reconstruct the track. MCVal is a mix of both. While the information that is used to reconstruct the V^0 is the same as in Rec, it has to relate to a MCTrue V^0, to make sure it is indeed a photon conversion. MCTruthOnly is pure Monte Carlo data that is not reconstructed in any way, but directly used from the generated particles. This can be used to e.g. get the number of produced or converted particles. MCTrue and Rec are stored in user made tables, while MCVal is deduced on the fly from MCTrue and Rec and MCTruthOnly is also first stored in a user table. The most important tables that are produced by the user tasks are the V0DaughterTracks tables, that store information like e.g. momenta, crossed rows and TPCSignal for the energy loss for every track that is part of Rec. Information on the V^0 in Rec is stored in V0Datas. McGammasTrue stores information of MCTrue V^0s. The mentioned tables are filled in *skimmerGammaConversions* and *skimmerGammaConversionsTruthOnlyMC* and then evaluated in *gammaConversions* and *gammaConversionsTruthOnlyMC*.

To carry out the analysis several additional tables had to be defined to store needed information. The recalculated coordinates of the conversion point are computed in the *skimmerGammaConversions* task and then stored

in V0Recalculated, which can be joined with V0Datas. Furthermore a table to store MCTrue information for tracks called V0DaughterMcParticle was added. This table can be related through the index table MCParticleIndex to the corresponding V0DaughterTracks table. The last table that was added is the McDaughterTrue table, which stores the track momentum for a V^0 in McGammasTrue and is related through index columns, but this is only used in the *skimmerGammaConversionsTruthOnlyMC* task. After all these tables are filled in the skimmer tasks they get handed to the *gammaConversions* and *gammaConversionsTruthOnlyMC* task. In these two tasks information from the created tables is taken and put into histograms which are stored in ROOT files.

To automate the local processing bash scripts were written that are capable of processing an entire data set in parallel. Utilizing the full power of the PI Server at Karls Ruprecht Universität Heidelberg it was possible to process the full LHC22c5 data set in less than 4 minutes. For much larger data sets and Monte Carlo simulations the ALICE Hyperloop train system [36] was used.

Finally, all the plots that can be seen in chapter 6 come from 12 ROOT macros that had to coded from scratch. In Figure 5.7 one can see a summary of the work.
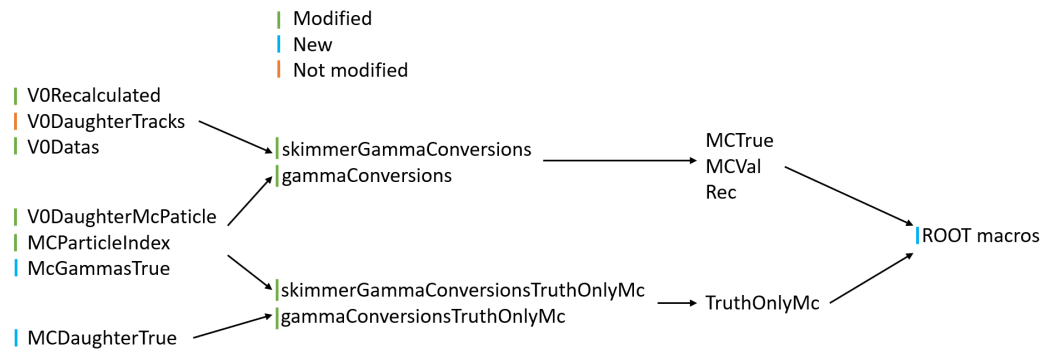

Figure 5.7: Modified, not modified and new tasks implemented in the course of the analysis.

5.4   Electron and photon PID cuts

In order to get reconstructed photons from electron-positron pairs it is absolutely essential to remove other charged particles and V^0s that are not photons from the data, otherwise conversions that are physically impossible or from other unrelated decays might get used in the analysis. To filter the data a set of cuts and settings, that restricts certain values for different properties of the particles, is used. Since the analysis is done in different tasks, the cuts are assigned to their corresponding analysis task. In Table 5.2 cuts of the *lamdakzeroBuilder* task, in Table 5.3 cuts of the *gammaConversion* task and in Table 5.4 cuts of the *gammaConversion-TruthOnlyMC* task are listed.

cut	value
Min. DCA of neg. track to primary vertex [cm]	0.1
Min. DCA of pos. track to primary vertex [cm]	0.1
Minimum crossed rows	30
Magnetic field B_z	-999 (CCDB)
Minimum cosinus of the pointing angle	0.85
DCA for V^0 daughters [cm]	2
V^0 radius [cm]	1

Table 5.2: Cuts for *lambdakzeroBuilder*

cut	value
V^0	
Minimum cosinus of the pointing angle	0.85
Angle between XY and particle momentum plane $\psi_{pair,max}$	-0.1
Maximum pseudo-rapidity $\lvert\eta_{\max}\rvert$ for MC photon validation	0.8
Minimum conversion radius $R_{\min}$ [cm]	0
Maximum conversion radius $R_{\max}$ [cm]	180
Line cut Z_0 [cm]	12
Line cut ZR slope	$\tan\left(2\cdot\arctan\left(\exp\left(-\eta_{\max}\right)\right)\right)$
Track selection and quality	
Maximum pseudo-rapidity $\lvert\eta_{\max}\rvert$	0.8
Minimum transverse momentum $p_{T,\min}$ [GeV/c]	0.04
Minimum ratio of $\frac{\text{found clusters}}{\text{findable clusters}}$	0.3
Minimum ratio of $\frac{\text{crossed rows}}{\text{findable clusters}}$	0
Electron selection	
σ below e^- line in $\frac{\mathrm{d}E}{\mathrm{d}x}$	-3
σ above e^- line in $\frac{\mathrm{d}E}{\mathrm{d}x}$	3
Pion rejection	
Minimum track momentum p to apply π-rejection [GeV/c]	0.4
Border between low and high momentum p π-rejection [GeV/c]	8
σ to be above π-line in $\frac{\mathrm{d}E}{\mathrm{d}x}$ for low p	-10
σ to be above π-line in $\frac{\mathrm{d}E}{\mathrm{d}x}$ for high p	-10
Photon selection	
Maximum Photon asymmetry	1
p_T multiplicator for q_T cut	0.125
$q_{T,\max}$ for q_T cut [GeV/c]	0.05

Table 5.3: Cuts for *gammaConversionTask*

cut	value
is a physical primary	false
Maximum pseudo-rapidity $\lvert \eta_{max} \rvert$	0.8
Minimum conversion radius $R_{\min}$ [cm]	0
Maximum conversion radius $R_{\max}$ [cm]	180
Number of daughter particles	2
Line cut Z_0 [cm]	12
Line cut ZR slope	$\tan\left(2 \cdot \arctan\left(\exp\left(-\eta_{\max}\right)\right)\right)$

Table 5.4: Cuts for *gammaConversionTruthOnlyMC*

In the following paragraph the meaning of the cuts is clarified. In Table 5.2 the maximum DCA, between the track and reconstructed vertex and the minimum number of crossed rows is set, where crossed rows refer to the rows in the pad plane of the TPC. The magnetic field is taken from the calibration object in the CCDB. Furthermore the cosine of the minimum pointing angle, which is the angle between the momentum of the V^0 and the vector to the collision point, is defined. Then the minimum DCA for V^0 daughters and the V^0 radius is set. In Table 5.4 the Monte Carlo specific cuts are listed. The cut for Physical Primaries [37] is turned off, since this is not available for data and would make comparing data with Monte Carlo simulations impossible. The maximum measurable pseudo-rapidity as well as the range, where a conversion of a photon is accepted, is set. Particles that convert outside of this range can not be tracked properly. The line cut refers to Figure 6.1 and is used to remove particles that are outside of the measurement range. This is done by removing all particles, that don't meet the selection criteria:

$$Z > Z_0 + R \cdot \tan\left(2 \cdot \arctan\left(\exp\left(-\eta_{max}\right)\right)\right) \tag{5.12}$$

In Table 5.3 similar cuts are defined in order to further select photons. The idea behind using the same cuts in multiple tasks several times is to be able to select V^0s with open cuts and then select photons depending on the analysis. The maximum angle $\psi_{pair,max}$ between the transverse plane

and the plane defined by the momentum of the electron and positron is set to a negative value, which means that the cut is deactivated. In Track selection and quality there are additionally cuts that specify the quality of the detected tracks by removing tracks that didn't leave enough measurable clusters or didn't cross enough rows. This can happen for e.g. charged particles that come from conversions that took place in the outer radial regions of the detector. To filter electrons and positrons from other particles a 3 σ cut around the electron line in the Bethe Bloch function is made. Furthermore, there are cuts for additional pion rejection, which work similar to the electron selection. Particles that are several σ below the pion line in the energy loss dE/dx diagram are removed. This cut is currently deactivated by only removing particles that are lower than 10 σ below the pion line. The asymmetry cut on the Armenteros-Podolanski distribution removes particles, with $|\alpha|$ beyond 1, which means that no particles are removed by this cut. α is defined by:

$$\alpha = \frac{p_L^+ - p_L^-}{p_L^+ + p_L^-} \tag{5.13}$$

where p_L^+ is the longitudinal momentum of the positive daughter particle and p_L^- is the longitudinal momentum of the negative daughter particle. The p_T multiplicator and q_T cuts are line cuts that can be seen in Figure 6.12. They are defined by:

$$q_T < 0.125 p_T \tag{5.14}$$

$$q_T < 0.05 \text{GeV/c} \tag{5.15}$$

where q_T is the transverse momentum of the daughter particle.

6 | Analysis of photon conversions in ALICE

For the main part of the analysis the Pilot beam of October 2021 and the corresponding Monte Carlo simulation LHC22c5 were chosen, since they showed the best statistics for the reconstruction and were easily accessible at the time of the analysis. Reconstructed photon conversions in the Pilot Beam data are refereed to as Rec, which stands for reconstructed and are the only type of data available for the real measurement. For the Monte Carlo simulation there are four types of data: MCTrue, MCVal, Rec and TruthOnlyMc. Rec is obtained by simulating the measurement process of generated particles. This type of data can be directly compared to the real measurement. MCTrue uses the real Monte Carlo information of particles for the reconstruction algorithm and is used as a reference. MCVal is in principle the same as Rec, but for this data the photon conversion is verified, as it is matched with MCTrue. This can be useful when analyzing Rec, but not wanting to deal with contamination. Lastly TruthOnlyMc are all generated Monte Carlo particles and can be used to research e.g. the conversion probability in the detector. For this kind of data no reconstruction is necessary, since the data comes directly form the generated Monte Carlo particles. As a general remark it should be mentioned that PID and photon selection cuts were applied to every plot, except where it is explicitly stated otherwise. Furthermore, cuts for the V^0s as described in Table 5.2 are always used.

First in section 6.1 the implementation of the detector material in the Monte Carlo simulation is evaluated. Then in section 6.2 the conversion probability is analyzed. After that the purity of the data is validated in section 6.3. This is followed by the analysis of the spacial and transverse momentum resolution of the reconstructed photons in section 6.4 and section 6.5. Then the reconstruction efficiency is computed and discussed in section 6.6. At the end of the analysis the electron momentum distribution is researched in section 6.7 and then the LHC22c5 and the Pilot Beam data are compared in section 6.8.

6.1 Implementation of the detector material in Monte Carlo simulations

In this section the implementation of the detector material in the Monte Carlo simulation is investigated. Since photon conversions only happen in the presence of a nucleus due to conservation laws, the location of the detector material can be examined by looking at the conversion points. To do so the LHC22c5 dataset was examined with the *gammaConversions-TruthOnlyMC* task, which creates plots of the true conversion points for all the generated photons TruthOnlyMc in the simulation. In Figure 6.1 and Figure 6.2 the photon conversion vertices can be seen.
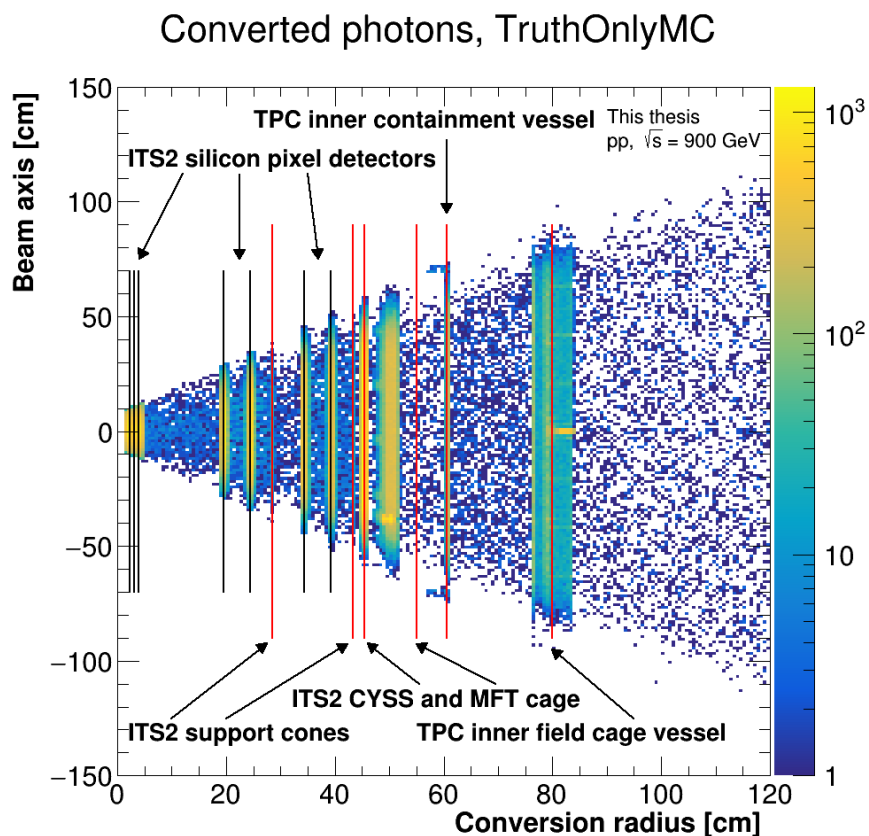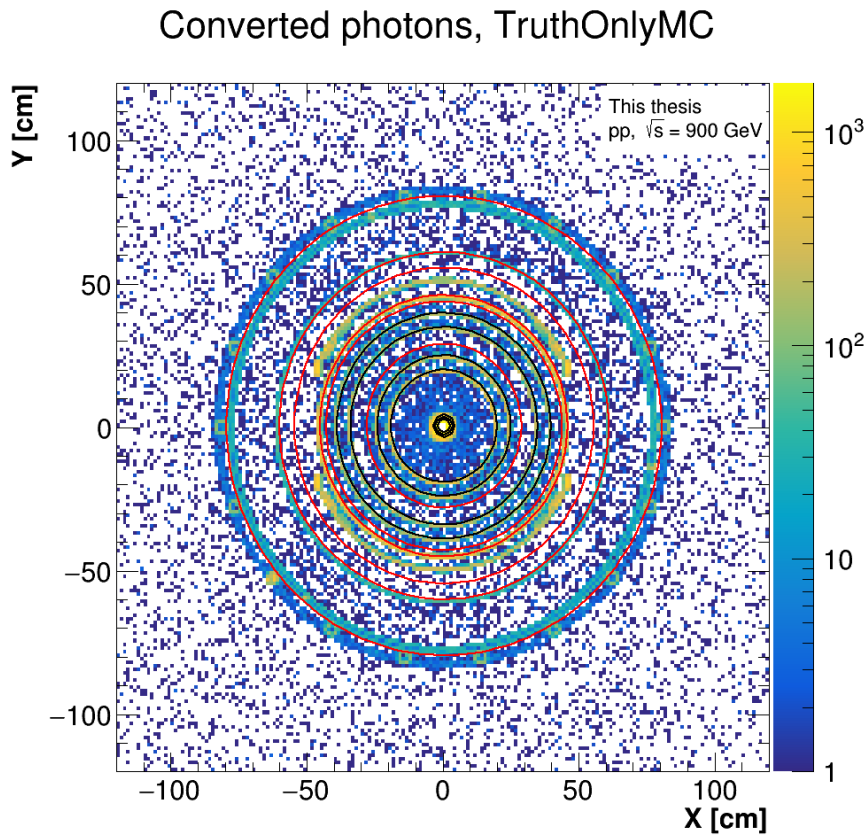

Figure 6.1: Conversion point coordinates *Z* vs. *R* for all TruthOnlyMc photons. Lines represent locations of ALICE components.

In Figure 6.1 a distinctive pattern of conversion points can be observed. To make the interpretation easier the radial locations of detector components are depicted in the form of lines. Black lines represent silicon pixel detector layers of the ITS2 as listed in Table 3.1, while red lines represent locations of structural components, which are listed in Table 3.2. Almost all the spots of high conversion probability match the lines, except the ITS-MFT cage, which is misplaced by about 5 cm according to the experts. This result was communicated to the responsible personnel for the implementation of the detector material.

Figure 6.2: Conversion point coordinates *Y* vs. *X* for all TruthOnlyMc photons. Lines represent locations of ALICE components.

In Figure 6.2 the radial structure of the detector is visible. Just like in the previous plot almost all areas of high conversion probability match the

components represented by the lines. One can see, that the ITS-MFT cage, which is located at a radius of approximately 50 cm, is not fully enclosed in φ, as it should be. This issue was cleared up after some communication with the implementer of the material budged in Monte Carlo simulations. It turns out that the ITS-MFT cage was not fully implemented at the time of the creation of the LHC22c5 dataset.

6.2   Conversion probability

To conduct an analysis on the conversion probability the LHC22c5 Monte Carlo simulation was processed with the analysis chain and the TruthOnlyMC photons were evaluated. In Figure 6.3, the amount of produced photons and converted photons over the p_T range is shown.
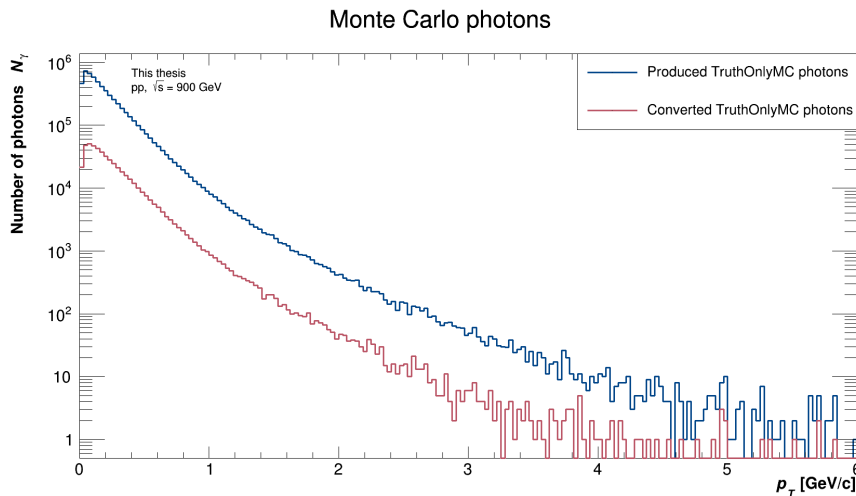
Figure 6.3: Amount of TruthOnlyMC produced photons and converted photons are plotted over p_T for LHC22c5.

As expected the amount of converted photons is much smaller than the amount of produced photons. By dividing the distributions the conversion probability depending on p_T can be calculated:

$$p_{\text{conv}}(p_T) = \frac{N_{\text{conv}}(p_T)}{N_{\text{prod}}(p_T)} \tag{6.1}$$

where $p_{conv}(p_T)$ is the conversion probability, $N_{conv}(p_T)$ is the number of converted photons and $N_{prod}(p_T)$ is the number of produced photons as a function of p_T respectively.
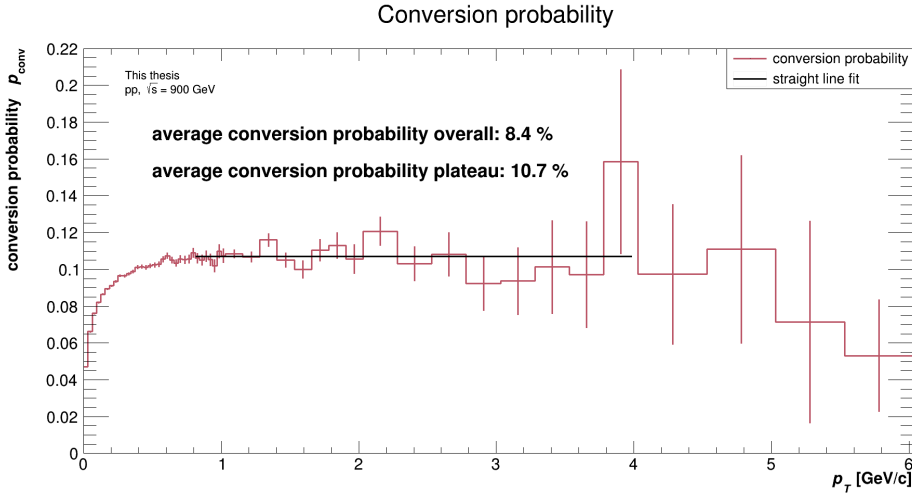

Figure 6.4: Conversion probability of photons, calculated by dividing the amount of converted photons by the amount of produced photons for the range of $0\,cm < R < 180\,cm$ for LHC22c5.

In Figure 6.4 the conversion probability for low momenta rises until it reaches its maximum at around $1\,GeV/c$. This is more or less what is expected in theory, where the cross section begins rising at around $1\,MeV/c$ until it converges at around $1\,GeV/c$. A straight line fit was performed at the plateau for a range of $0.8\,GeV/c < p_T < 4\,GeV/c$. From this a conversion probability of $10.7\,\%$ was determined. For the whole momentum range a conversion probability of $8.4\,\%$ was calculated.

Additionally, R_{max} in Table 5.3 was set to $42\,cm$ to only account for conversions that happen in the ITS2. This results in a significantly lower conversion probability of $4.2\,\%$ for the plateau and $2.2\,\%$ in total as one can see in Figure 6.5. This result seems plausible when compared to the claimed material budged of $4.038\,\%$ [38]. An error was not calculated because the systematic error from the not completely implemented material in the Monte Carlo simulation is unclear.
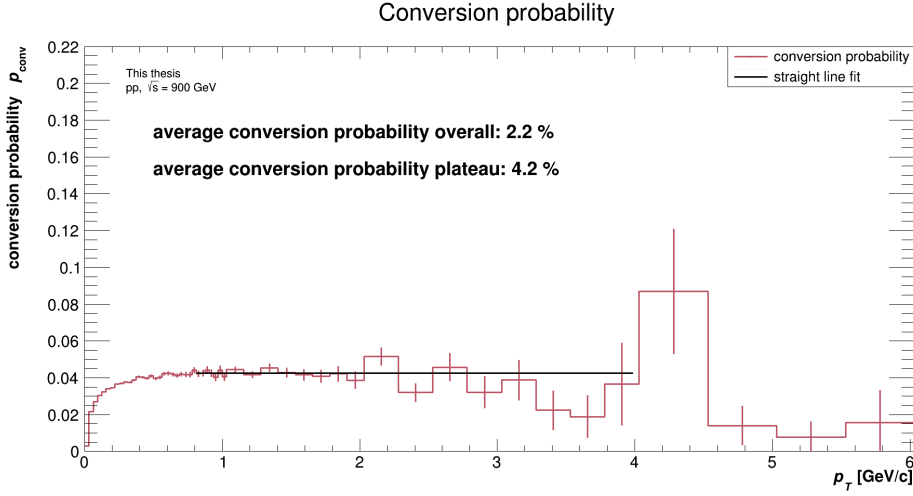
Figure 6.5: Conversion probability of photons for the range of $0\,\mathrm{cm} < R < 42\,\mathrm{cm}$ for LHC22c5.

6.3 Purity of the electron and photon sample

First of all it is mandatory to select photons among all V^0 candidates while keeping the efficiency as high as possible. Therefore PID and photon selection cuts, described in Table 5.3, are applied to the data sets. In order to evaluate the result, different distributions of reconstructed photon conversions are plotted before and after applying the PID and photon selection cuts. For the plots Rec data is used. This is done for LHC22c5, as well as for the Pilot Beam data.

In Figure 6.6 and Figure 6.7 one can see the energy loss by ionization $\mathrm{d}E/\mathrm{d}x$. It is clearly visible, that the cuts remove the pions, kaons and protons, but leave the electrons.

In addition to that in Figure 6.8 and Figure 6.9 $\mathrm{d}E/\mathrm{d}x$ in terms of numbers of sigma with respect to the electron line is shown. Here it is clearly visible that the contamination from pions, kaons and protons is removed. However, it should be noted that the plots after cuts are not centered around zero. This discrepancy is occurring most likely due to the fact, that the TPC calibration is still ongoing.
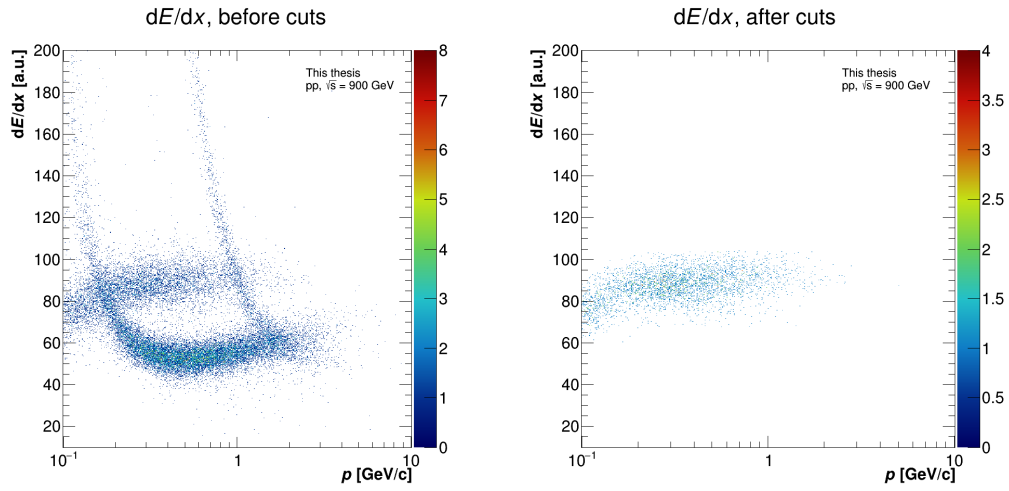
Figure 6.6: Ionization energy loss for both tracks belonging to a V^0 candidate. LHC22c5 before and after applying track quality, PID and photon selection cuts.
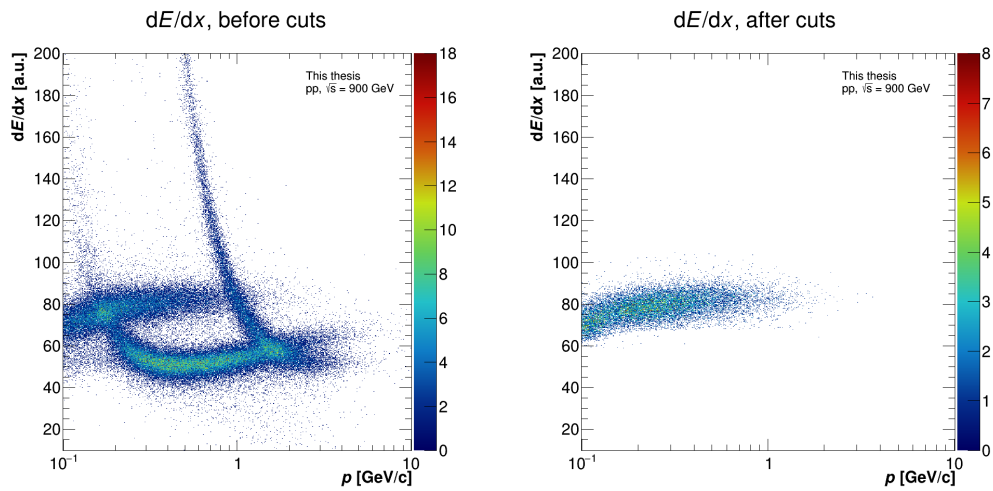

Figure 6.7: Ionization energy loss for both tracks belonging to a V^0 candidate. Pilot Beam before and after applying track quality, PID and photon selection cuts.
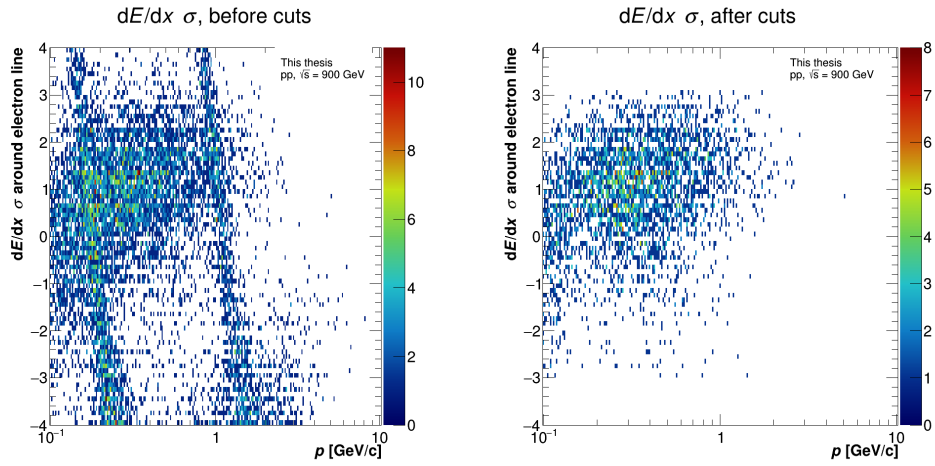
Figure 6.8: Track quality around the electron line for LHC22c5 before and after applying track quality, PID and photon selection cuts.
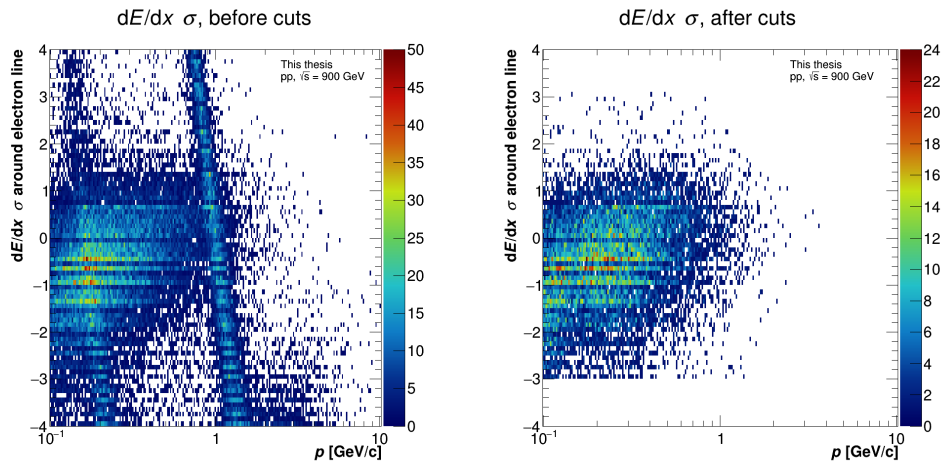

Figure 6.9: Track quality around the electron line for Pilot Beam before and after applying track quality, PID and photon selection cuts.

In Figure 6.10 and Figure 6.11 the Armenteros-Podolanksi plots are shown. Before the track quality, PID and photon selection cuts are applied, Λ, $\overline{\Lambda}$, K_S^0 and γ are visible in the form of lines and areas. After the cuts are applied only the area with photons is visible, which indicates, that the photon selection is working well.
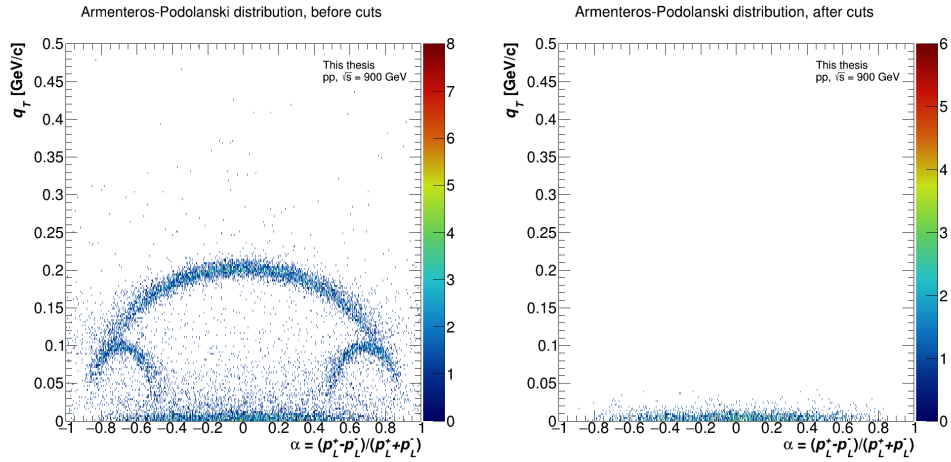
Figure 6.10: Armenteros-Podolanski distribution for LHC22c5 before and after applying track quality, PID and photon selection cuts.
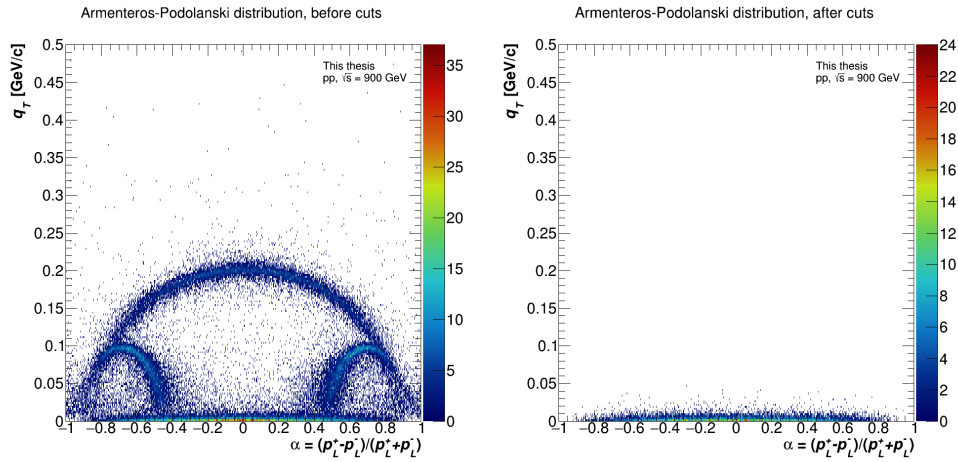

Figure 6.11: Armenteros-Podolanski distribution for Pilot Beam before and after applying track quality, PID and photon selection cuts.

In the next plots Figure 6.12 and Figure 6.13 cuts on the Armenteros-Podolenski distribution are further investigated. To do so q_T is plotted over p_T, where q_T represents the transverse momentum of the track and p_T represents the transverse momentum of the V^0. Lines represent two of the photon selection cuts.
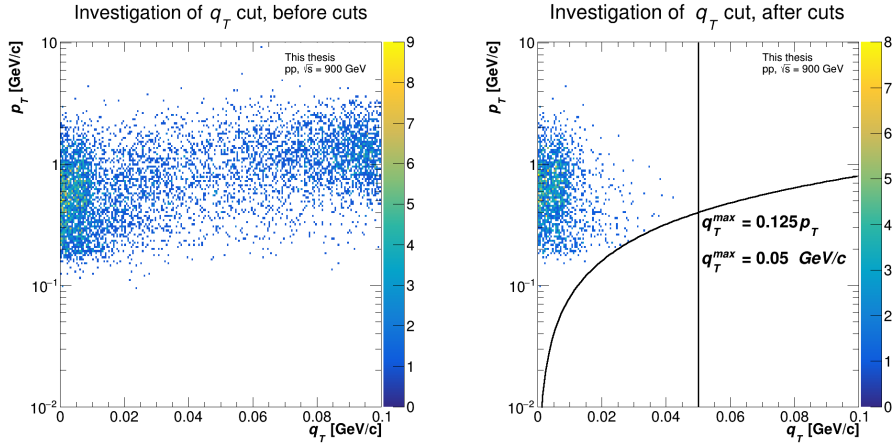
Figure 6.12: Transverse momentum p_T of the two tracks vs. transverse momentum q_T of the V^0 for LHC22c5. Black lines are the cuts that were used to eliminate contamination.
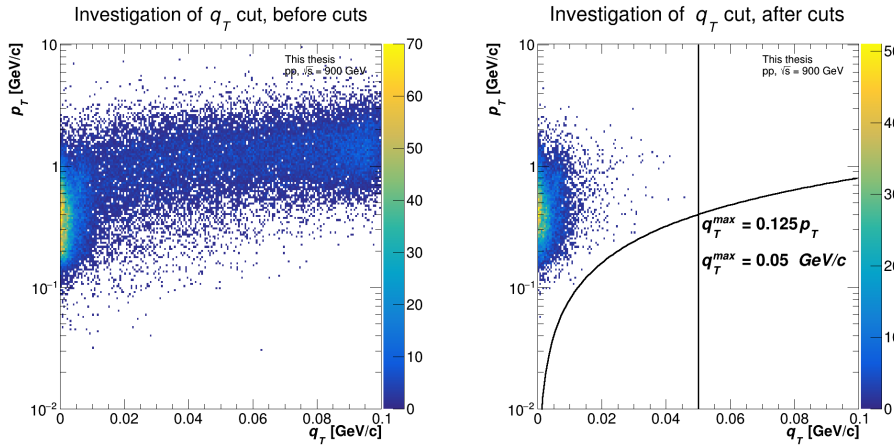

Figure 6.13: Transverse momentum q_T of the two tracks vs. transverse momentum p_T of the V^0 for Pilot Beam. Black lines are the cuts that were used to eliminate contamination.

These cuts are applied in the first place to remove any unwanted contamination, which originates from the reconstruction of V^0s from pairs other than e^+e^-. Figure 6.12 shows clearly, that there are no more reconstructed particles beyond the cut values. Skipping ahead we can see in

Figure 6.15, that most of the contamination is eliminated.

6.3.1 Quantitative analysis on the effects of the cuts

For a quantitative analysis on the photon purity after applied track quality, PID and photon selection cuts, the reconstructed V^0s and daughter particles Rec in LHC22c5 are researched. When a Monte Carlo particle is generated the PDG Code, along some other values are stored in the McParticles table. After the particle went through the detector simulation and "measured" values Rec are saved, the Rec values can be compared to the original PDG Code of the particle. By doing this, it is possible to find out how many and which V^0s particles pass the cuts apart from photons.

In Figure 6.14 different combinations of PDG Code for the daughter tracks of reconstructed V^0s in Rec are shown on the horizontal axis and the transverse momentum p_T on the vertical axis before and after applying the track quality, PID and photon selection cuts. In Figure 6.15 one can see the same histogram, but with projected transverse momentum.

Figure 6.14: Monte Carlo daughter track combinations of reconstructed V^0s as a function of the transverse momentum p_T before and after applying track quality, PID and photon selection cuts for LHC22c5.

61

Figure 6.15: Monte Carlo daughter track combinations of reconstructed V^0s before and after applying track quality, PID and photon selection cuts for LHC22c5.

In Figure 6.15 one can see, that most of the selected V^0 candidates after applied cuts come from $e^+ e^-$ pairs that have the same mother particle, while before applying the cuts the main contributor is $\pi^+ \pi^-$. Furthermore, two main sources of contamination after applied cuts can be identified:

- The largest contamination comes from matching of $e^+ e^-$, that don't belong to the same mother particle.

- The second-largest contamination is represented by the "other" bin. After an investigation it was found that most track combinations in this bin come from tracks with the same charge like e.g. $e^- e^-$. This source of contamination is highly questionable and should be investigated further in a consecutive analysis, since this could provide valuable information on the V^0 finder algorithm and on the analysis chain.

In total 2088 reconstructed V^0 were considered as photons in Rec. Out of these particles 1689 have $e^+ e^-$ as daughter tracks. Checking the PDG Code

of the V^0 results in 1638 photons. So there are 51 e^+e^-, whose mother is not a photon. These tracks most likely come from Dalitz decays.

The purity ϵ_{purity} can be determined by dividing the number of particles that are truly photon conversions N_γ by the number of reconstructed V^0 candidates that are considered as a photon conversion $N_{V^0,\gamma}$:

$$\epsilon_{purity} = \frac{N_\gamma}{N_{V^0,\gamma}} \tag{6.2}$$

This results in a purity of:

$$\epsilon_{purity} = 78 \text{ %}.$$

6.4   Spacial resolution

In order to achieve the best resolution possible and eliminate any biases, the conversion point was recalculated according to section 5.2. The results of this recalculation will be presented here in the form of several plots. Due to the symmetry of the detector the plots are categorized in R, which represents the radial distance in the XY plane and Z. Figure 6.16 and Figure 6.19 show ΔR over R and ΔZ over Z, where ΔR and ΔZ are the differences between the true conversion point using MCTrue and the corresponding reconstructed value from MCVal. The areas for the one dimensional projections, marked by the dotted lines in Figure 6.16 and Figure 6.19, are chosen such that there is a relevant amount of entries in each area while still differentiating between different parts of the detector. The one dimensional projections can be found in the appendix in Figure A.2 and Figure A.3.

6.4.1   Resolution of R
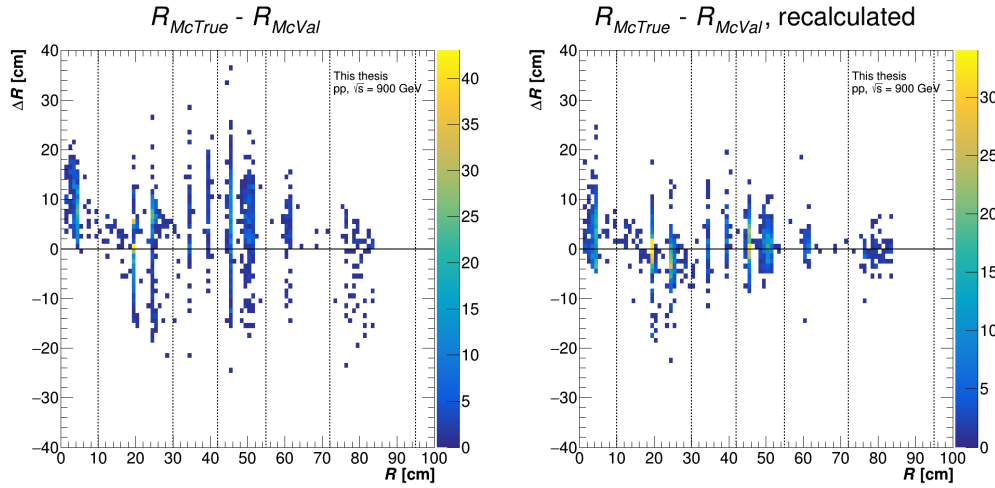
Figure 6.16: ΔR v.s. R before and after recalculation for LHC22c5 dataset after applying PID and photon selection cuts. Lines represent areas that are projected to in the corresponding one dimensional plot Figure A.2.

64

In Figure 6.16 it is already visible, that the deviation is a lot smaller and ΔR is a lot more centered around $0\,\text{cm}$ after the recalculation of the conversion point coordinates. To quantify these observations entries between dotted lines were projected onto the ΔR axis, resulting in 6 R ranges. After that Gaussian functions were fitted to the ΔR distributions. Plots of the projections of the different ranges and their Gaussian fits can be found in the appendix in Figure A.2. The parameters of the Gaussian fits were evaluated and plotted in Figure 6.17.
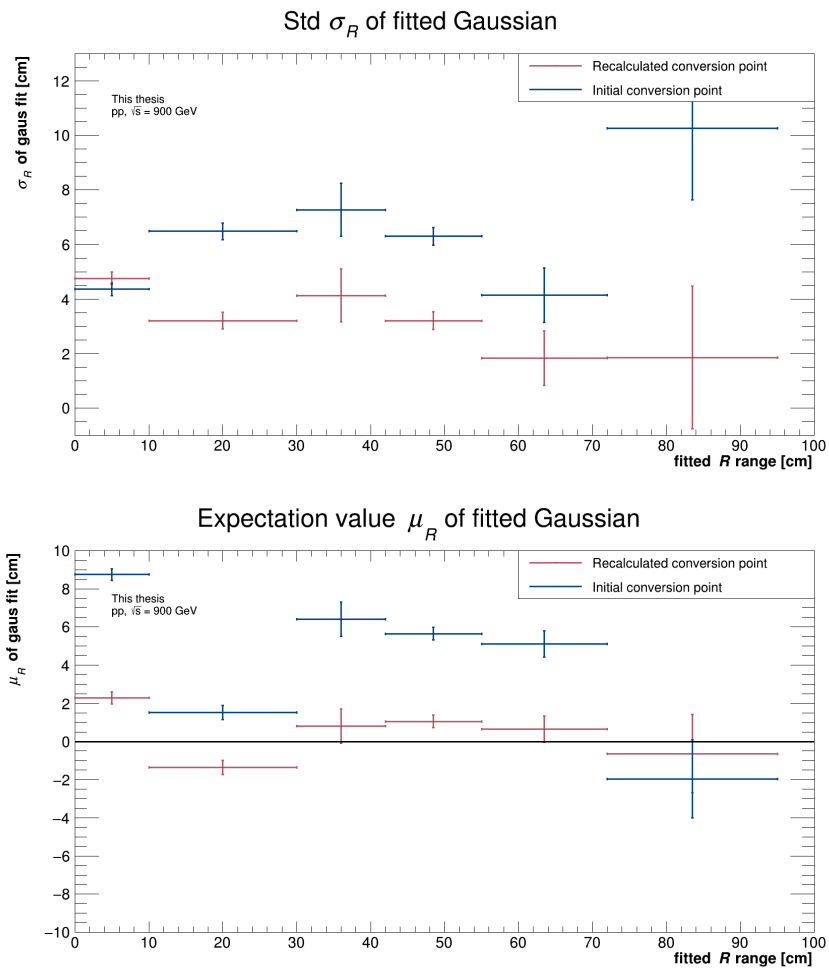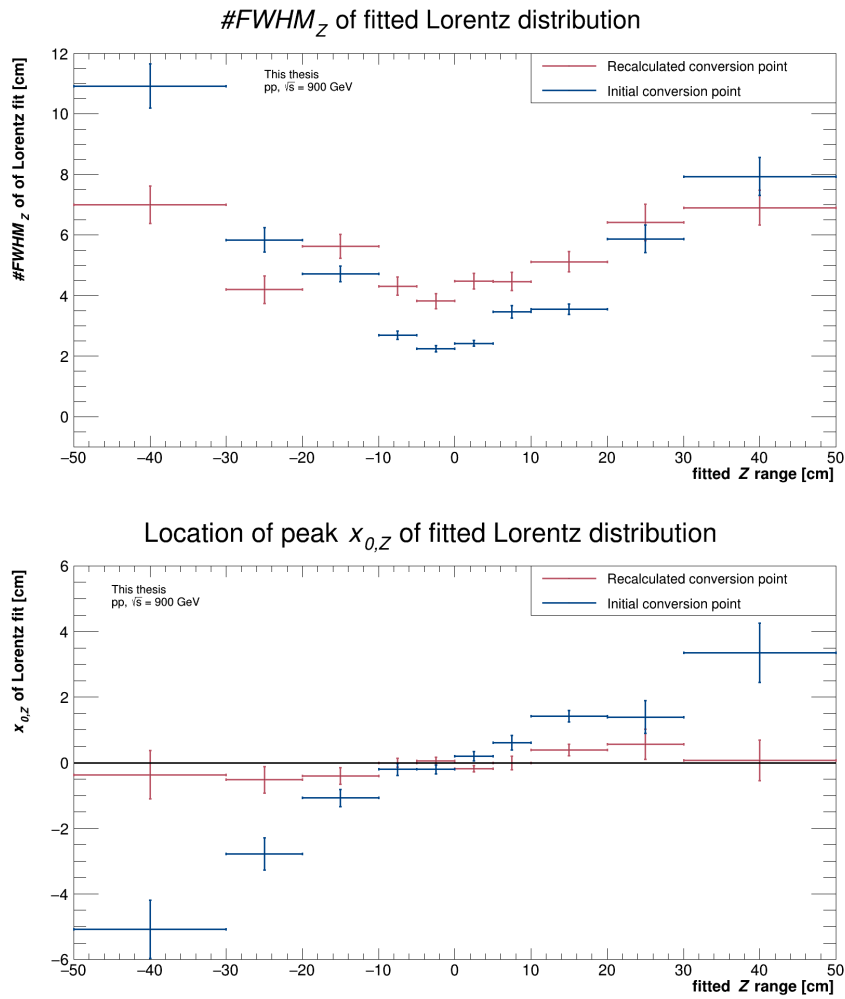

Figure 6.17: Fit parameters for Gaussian fits, that were performed for different R ranges. Horizontal bars represent the fit range and vertical bars represent the error of the fit parameter.

65

In the upper plot in Figure 6.17 it can be observed that the recalculation of the conversion point clearly decreases the width of the Gaussian function, which means that the resolution was improved. The fits for the range of $0\,\mathrm{cm} < R < 180\,\mathrm{cm}$ resulted in:

$$\sigma_{\mathrm{initial},R} = (6.5 \pm 0.2)\,\mathrm{cm}$$

$$\sigma_{\mathrm{recalculated},R} = (3.75 \pm 0.09)\,\mathrm{cm}$$

This corresponds to an improvement of factor (1.73 ± 0.05). Furthermore, one can see that the means are much more centered around $0\,\mathrm{cm}$. The fits for the range of $0\,\mathrm{cm} < R < 180\,\mathrm{cm}$ resulted in:

$$\mu_{\mathrm{initial},R} = (4.89 \pm 0.18)\,\mathrm{cm}$$

$$\mu_{\mathrm{recalculated},R} = (0.38 \pm 0.10)\,\mathrm{cm}$$

Despite the big improvement there are still some ranges like for instance $0\,\mathrm{cm} < R < 10\,\mathrm{cm}$ that deviate significantly from $0\,\mathrm{cm}$. Possible causes for this are:

- Problems with the reconstruction of the tracks

- Statistical selection bias of tracks due to limited measurement capability or cuts

Furthermore the recalculated conversion point distribution R in MCVal is compared to the distribution of the true location of the conversion point R in MCTrue. In Figure 6.18 it is visible that the reconstructed recalculated conversion point R still deviates greatly from the true conversion point R. Nonetheless one can still observe that the general structure of the distribution of MCVal tends to have a similar shape as MCTrue. The bad resolution is most likely caused by the weak magnetic field of $0.2\,\mathrm{T}$ in $900\,\mathrm{GeV}$ runs. It would be beneficial to investigate the conversion point R for higher collision energies, where a stronger magnetic field of $0.5\,\mathrm{T}$ is used, which would result in a better resolution.
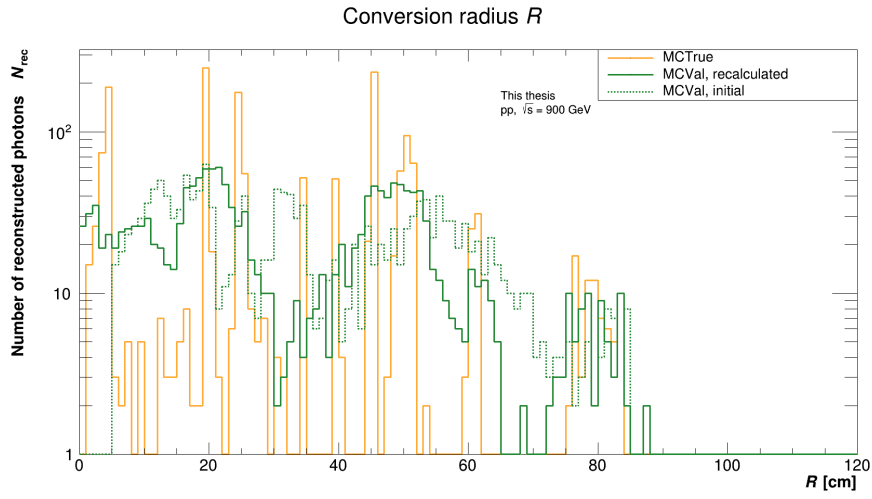
Figure 6.18: Distribution of conversion point R for MCTrue and MCVal recalculated for LHC22c5.

6.4.2 Resolution of Z
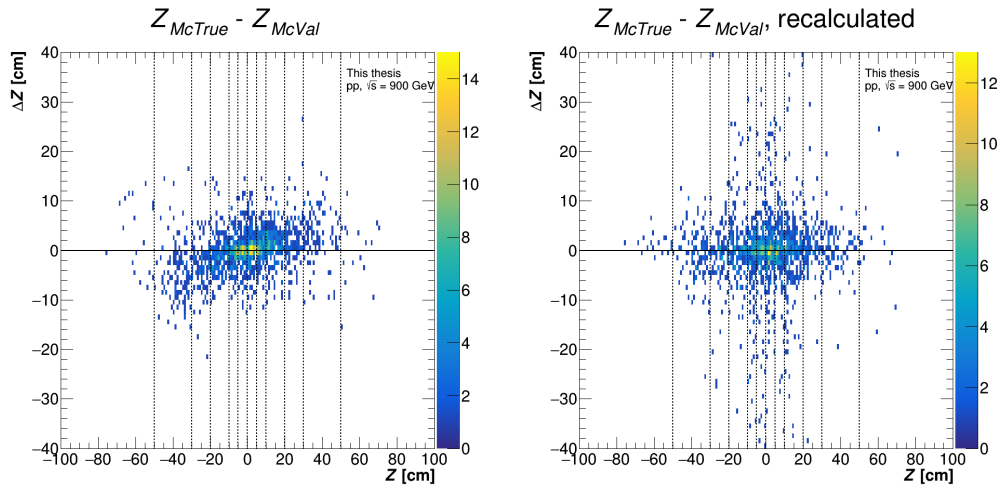
Figure 6.19: ΔZ vs. Z before and after recalculation for LHC22c5 dataset after applying PID and photon selection cuts. Lines represent areas that are projected to in the corresponding one dimensional plot Figure A.3.

In Figure 6.19 it seems like although the recalculation does not improve the width of the ΔZ distribution, it is much more centered around $0\,\text{cm}$. Analogues to R the entries between dotted lines were projected onto the ΔZ axis, which results in 10 Z ranges. After that Lorentz functions were fitted to the ΔZ distributions. The reason the distributions differ is most likely due the symmetry of the detector. Since the benefit of investigating this any further is too small compared to the effort, no consecutive investigation was made. Plots of the projections and the fitted Lorentz functions can be found in the appendix in Figure A.3. The parameters of the Lorentz function were also evaluated and plotted in Figure 6.20.

In Figure 6.20 the FWHM vary a lot depending on the fitted Z range, making it unclear whether there is an improvement or not. For the range of $-50\,\text{cm} < Z < 50\,\text{cm}$ the FWHMs of the Lorentz fits are:

$$FWHM_{\text{initial},Z} = (3.84 \pm 0.15)\,\text{cm} \tag{6.3}$$

$$FWHM_{\text{recalculated},Z} = (4.62 \pm 0.18)\,\text{cm} \tag{6.4}$$

The difference of these two FWHM values is $\Delta FWHM = (0.8 \pm 0.2)\,\text{cm}$ and thus deviates by 4σ from $0\,\text{cm}$.

The location of the peak of the fitted Lorentz function for the range of $-50\,\text{cm} < Z < 50\,\text{cm}$ are:

$$x_{0,\text{initial},Z} = (0.08 \pm 0.06)\,\text{cm} \tag{6.5}$$

$$x_{0,\text{recalculated},Z} = (-0.07 \pm 0.08)\,\text{cm} \tag{6.6}$$

However despite the good centering of the initial resolution around $0\,\text{cm}$ for the whole range there is still clearly a bias visible in Figure 6.19 as well as in Figure 6.20: for lower Z values the center of the Lorentz function tends to be negative and for higher Z values it tends to be more positive. This problem is completely gone for the recalculated distributions. As stated before it would be beneficial to investigate this property further with better statistics and higher collision energy.
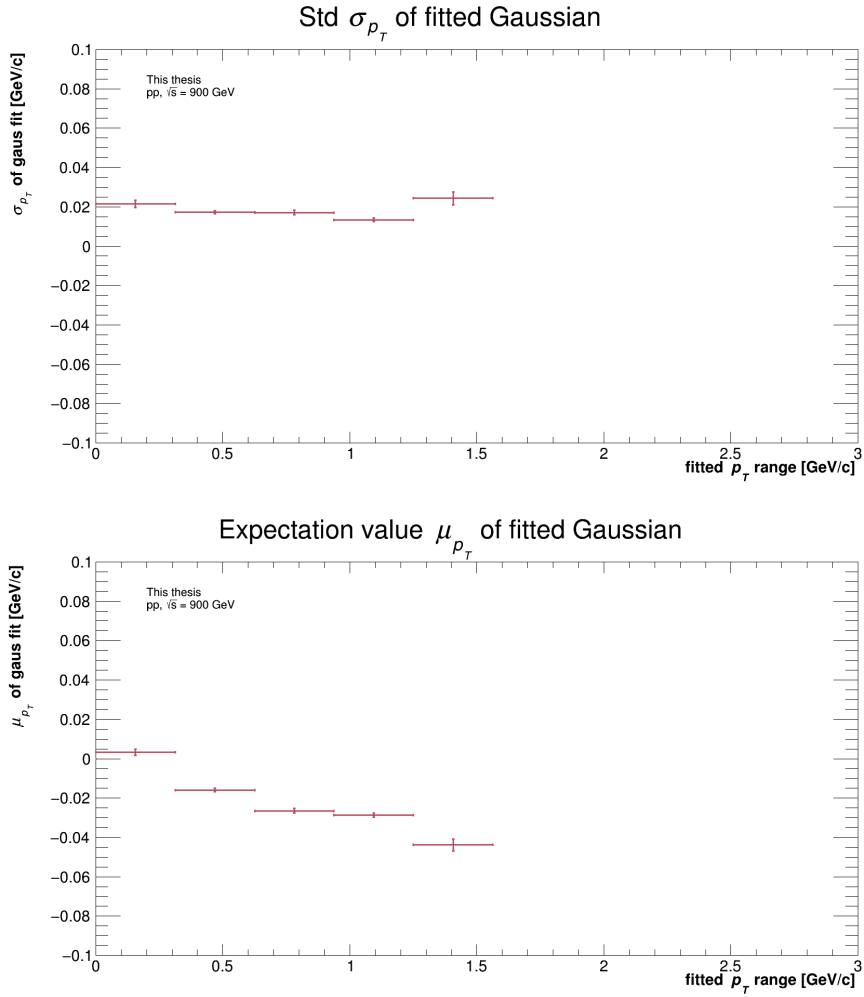
Figure 6.20: Fit parameters for Lorentz fits, that were performed for different Z ranges. Horizontal bars represent the fit range and vertical bars represent the error of the fit parameter.

In order to investigate the deterioration of the resolution further in the range between $-50\,\mathrm{cm}$ and $50\,\mathrm{cm}$ the initial and recalculated distribution of Z for MCVal is compared to MCTrue. The results can be seen in Figure 6.21.
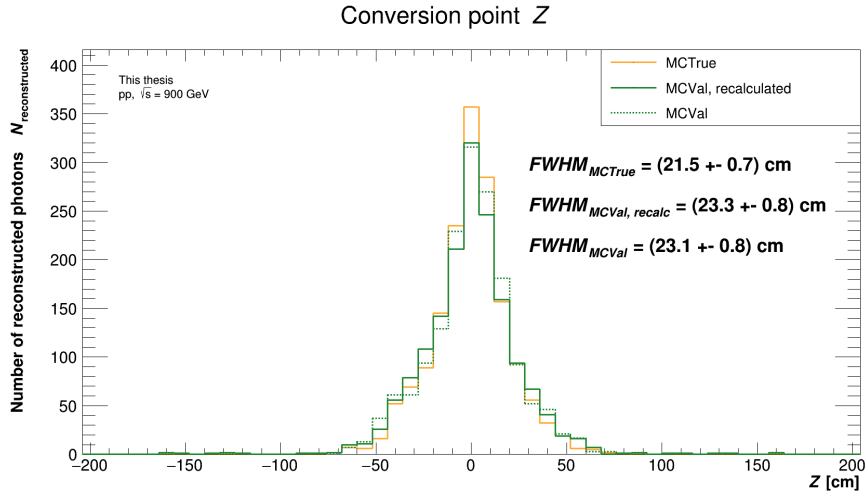
Figure 6.21: Distribution of Z for MCTrue, MCVal and MCVal recalculated for LHC22c5. For each distribution a Lorentz function is fitted and the $FWHM$ is printed out.

One can observe, that both the $FWHM$ of the initial MCVal and the recalculated MCVal for the Z distribution are slightly larger than the $FWHM$ of the MCTrue. However, since there are no significant deviations between the initial and recalculated MCVal, it is concluded that a slight decrease in the resolution doesn't affect the Z distribution in any significant way. Nevertheless, for larger statistics this might become significant and thus reasons for the decrease of the resolution need to be investigated in a consecutive analysis.

6.5 Transverse momentum resolution

In this section the transverse momentum resolution is researched, since this will be important in section 6.6. The transverse momentum resolution Δp_T is the difference between the true transverse momentum $p_{T,\text{MCTrue}}$ and the measured transverse momentum $p_{T,\text{MCVal}}$. In Figure 6.22 the resolution was plotted against the transverse momentum in order to see whether the resolution is worse for lower p_T than for higher.
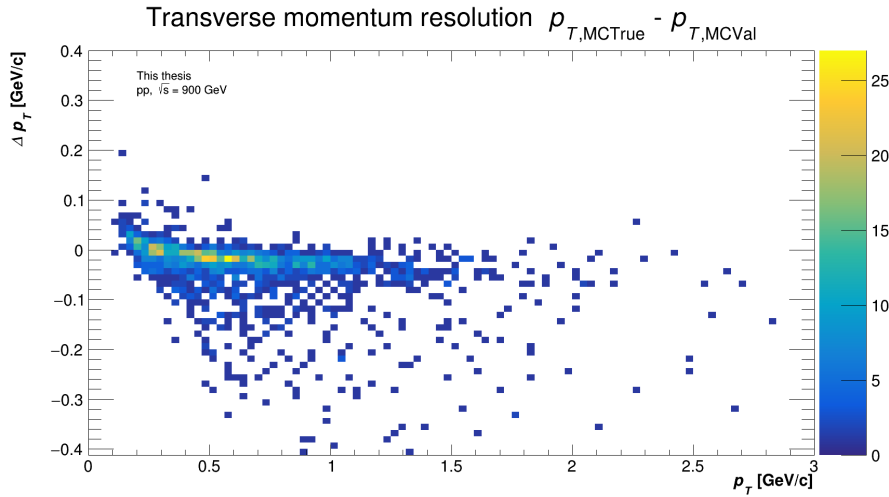
Figure 6.22: Resolution Δp_T vs. transverse momentum p_T of reconstructed photons for LHC22c5.

One can see that the resolution is approximately in between $-0.1\,\text{GeV/c}$ and $0.1\,\text{GeV/c}$ for the most part. A more precise evaluation is carried out by projecting different transverse momentum p_T ranges onto the Δp_T axis. Furthermore, Gaussian fits to the distributions were fitted similar to the spacial resolutions. These plots can be found in the appendix in Figure A.1. The parameters of the Gaussian fits are plotted in Figure 6.23.

Figure 6.23: Fit parameters for Gaussian fits, that were performed for different p_T ranges. Horizontal bars represent the fit range and vertical bars represent the error of the fit parameter.

In Figure 6.23 one can see that the width of the Δp_T distributions is approximately the same for all transverse momentum ranges. This is a good indicator that differences in the photon reconstruction and photon reconstruction efficiency for low and high transverse momenta p_T do not come from the momentum resolution. The resolution as an average for the whole transverse momentum range is:

$$\sigma_{p_T} = (0.0245 \pm 0.0008)\,\text{GeV/c}$$

6.6 Reconstruction efficiency

The reconstruction efficiency of photons is carried out using the *skimmerGammaConversionsTruthOnlyMC*, *skimmerGammaConversions*, *gammaConversions* and *gammaConversionTruthOnly* tasks. Just like in section 6.2 the TruthOnly tasks provide the amount of produced and converted photons. In addition to that the amount of reconstructed photons is computed by the regular tasks. The combined results can be seen in Figure 6.24 over the p_T range.
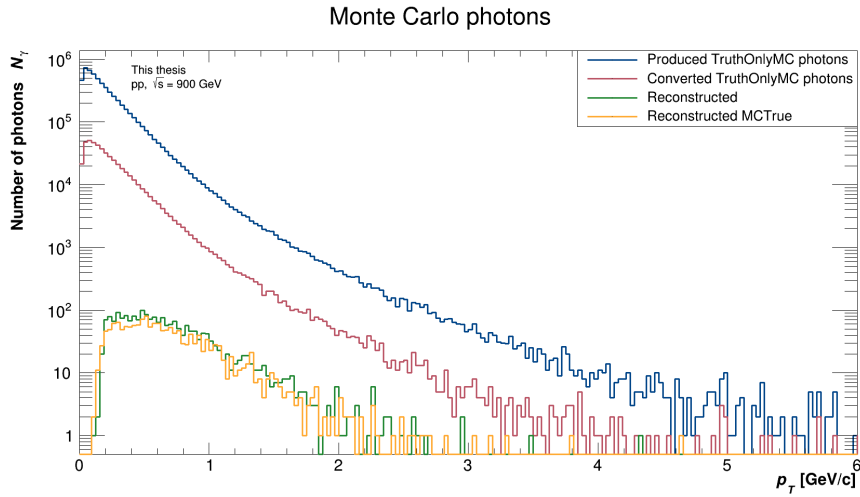
Figure 6.24: Amount of photons for the respective distribution is shown over p_T. The distribution for total and converted photons come from the *gammaConversionTruthOnly* task, whereas the distribution for the reconstructed and MCTrue photons is provided by the *GammaConversion* task. LHC22c5 Monte Carlo used.

The reconstruction efficiency as a function of p_T is calculated by dividing the number of reconstructed photons $N_{\mathrm{rec}}(p_T)$ by the number of converted photons $N_{\mathrm{conv}}(p_T)$:

$$\epsilon_{\mathrm{rec}} = \frac{N_{\mathrm{rec}}(p_T)}{N_{\mathrm{conv}}(p_T)} \tag{6.7}$$

73
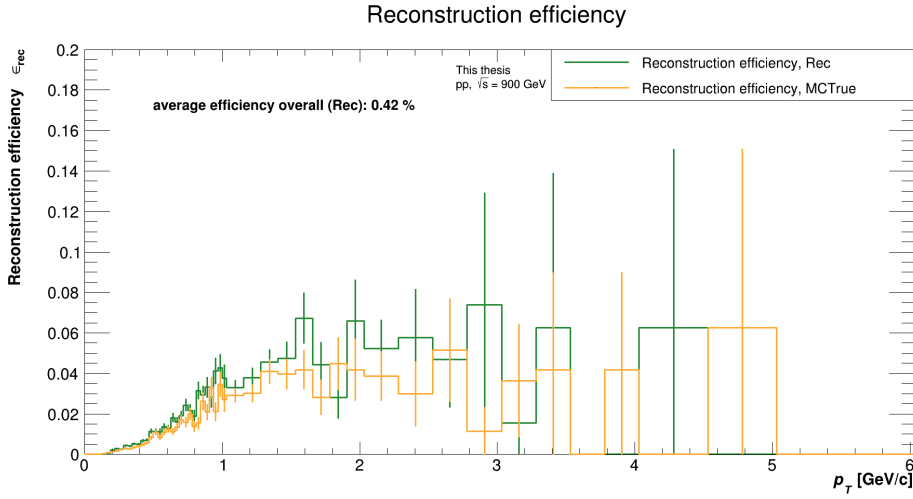
Figure 6.25: Reconstruction efficiency for photons. Calculated by dividing the amount of reconstructed photons by the amount of converted photons.

In Figure 6.25 the reconstruction efficiency is small for low p_T and rises for larger p_T. Just like for the conversion probability a straight line fit was performed for MCRec for a range of $1.5\,\text{GeV/c} < p_T < 3\,\text{GeV/c}$, which yielded an average value of 4.76 % around the plateau. The reconstruction efficiency for the total momentum range is 0.42 %. Both of these values are very small in contrast to the reconstruction efficiency of Run 2, which is on average higher than 80 % [39].

The source of this problem is currently being intensely investigated. Previous plots can be used for this research, since they can provide valuable information on the reconstruction. The low reconstruction efficiency at small p_T in Figure 6.25 lets one speculate, that the reconstruction is either highly negatively affected by the lower resolution for the track parameters of lower momenta, since the curvature of the track is much smaller, or the reconstruction works worse for higher radii, since low momentum photons are usually only reconstructed in an outer part of the detector. This effect can be studied more intensely by considering the distribution in Figure 6.26 and Figure 6.27.
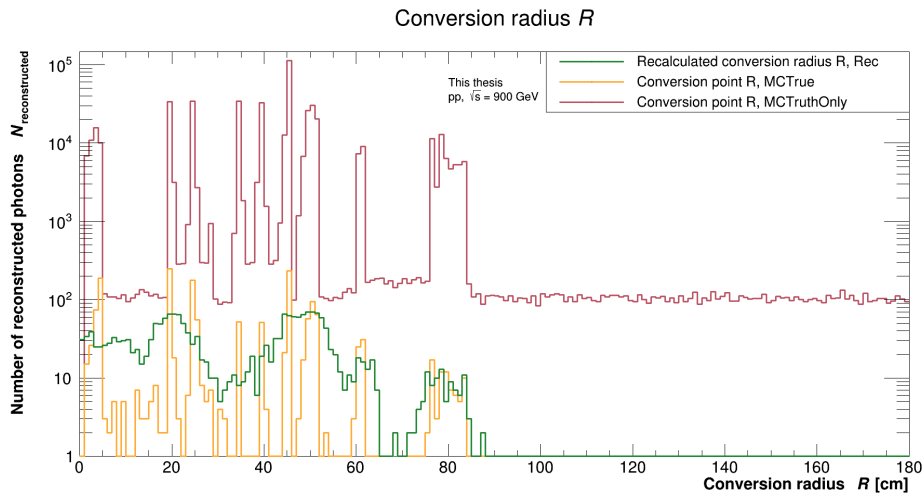
Figure 6.26: Amount of converted and reconstructed photons as a function of R.
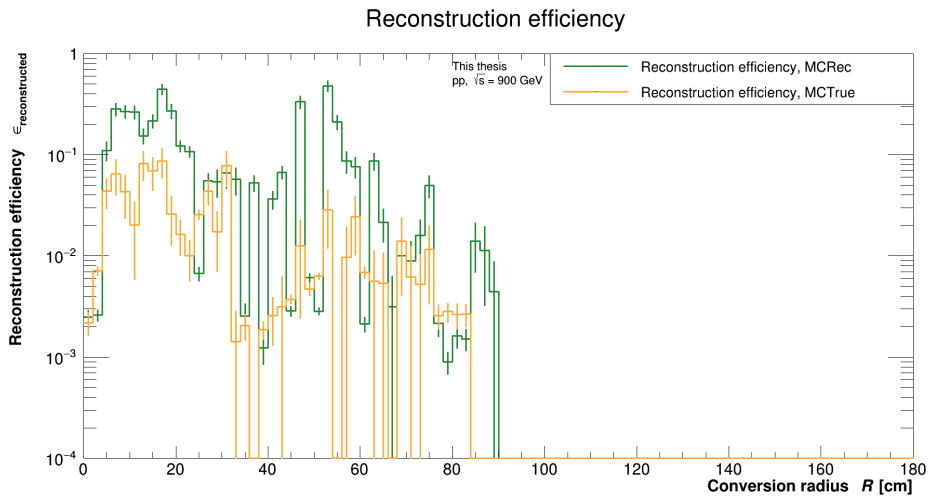
Figure 6.27: Reconstruction efficiency of MCRec and MCTrue as a function of R. Calculated by dividing the respective distribution by the amount of converted photons.

For small radii of less than 60 cm the reconstruction efficiency fluctuates a lot, with certain radii even peaking up to 50 % and other being as low as 0.001 %. For radii bigger than roughly 90 cm there are zero recon-

structed photons. However, photon conversions mainly happen at radii smaller than 80 cm as Figure 6.2 and Figure 6.26 show. Moreover, in Figure 6.26 it is visible, that MCTrue photons are several magnitudes below the converted photons at the peaks and there are approximately zero reconstructed MCTrue photons at radii, where the conversion rate is low like e.g. $R = 70$ cm. So for radii higher than 90 cm it is not unreasonable to assume that there are no photon reconstructions expected due to the low conversion rate at the current reconstruction efficiency. For now the problem of the low reconstruction efficiency cannot be linked to problems in the reconstruction of photons at higher radii.

Furthermore, it is also unlikely that the low reconstruction rate comes from a bad resolution at low p_T. Foremost the reconstruction efficiency is slightly higher at higher p_T, but still much lower than expected. Additionally, Figure 6.22 shows, that the momentum resolution is similar throughout the whole p_T range.

More statistics and higher magnetic field strengths of 0.5 T at higher collision energies are needed for a conclusive result. For now the most plausible reason is a problem in the V^0 finder algorithm or some kind of deficiency in the calibration.

6.7 Momentum asymmetry of electron-positron pair

Lastly the momentum asymmetry is analyzed. Since the electron mass is negligibly small in contrast to the kinetic energy, it is expected, that the fractional electron momentum distribution looks similar to Figure 4.5. In Figure 6.28 and Figure 6.28 one can see the fractional electron momentum $p_{T,e}/p_{T,\gamma}$ plotted against the transverse momentum p_T of the photon for all reconstructed photons Rec in LHC22c5 and the Pilot Beam data.
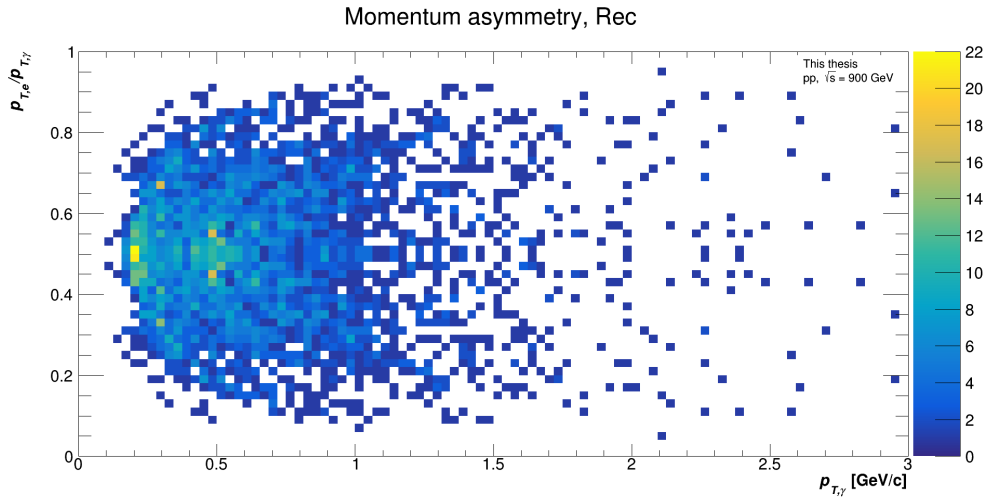
Figure 6.28: Fractional electron transverse momentum vs. transverse momentum for all reconstructed photons in LHC22c5.
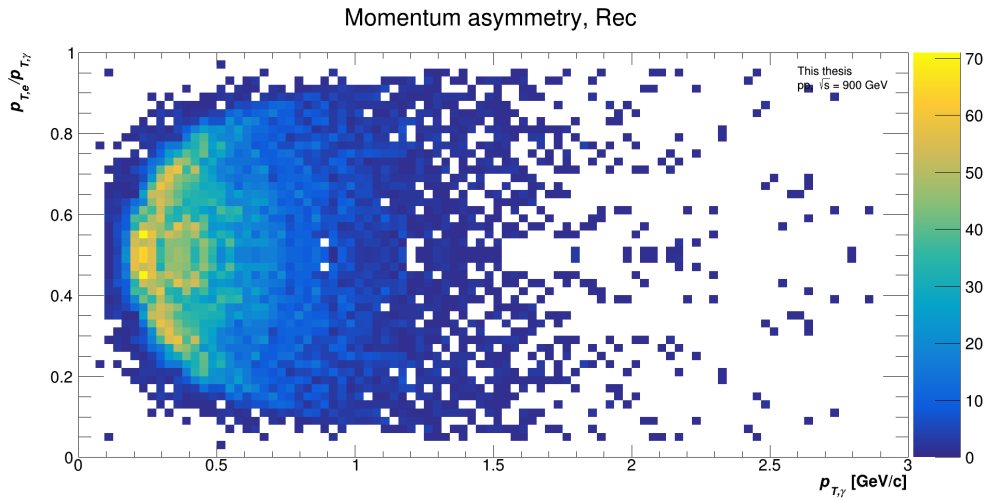
Figure 6.29: Fractional electron transverse momentum vs. transverse momentum for all reconstructed photons in Pilot Beam.

By comparing the two distributions one can see, that the momentum asymmetry of the LHC22c5 and the Pilot Beam seem reasonably similar and conclude that the reconstruction of photon conversions works equally well for real data and Monte Carlo in regard to the momentum asymmetry.

Additionally the fractional electron transverse momentum $p_{T,e}/p_{T,\gamma}$ was plotted for all converted photons TruthOnlyMc. The distribution can be seen in Figure 6.30.
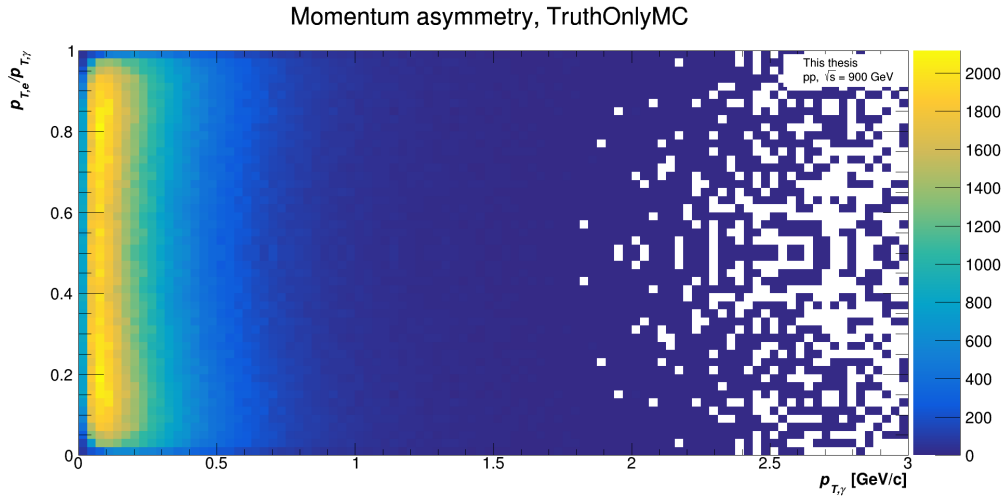
Figure 6.30: Fractional electron transverse momentum vs. transverse momentum of all converted photon in LHC22c5.

One can see that Figure 6.28 and Figure 6.30 look very different. This means, that there is a selection bias when reconstructing photons conversions, since there are proportionally more reconstructed photons with symmetric electron momentum, then with asymmetric electron momentum, when compared to the electron momentum distribution of all converted photons.

To investigate this further the distributions in Figure 6.28, Figure 6.29 and Figure 6.30 were projected onto different ranges of the photon momentum $p_{T,\gamma}$ in order to investigate the behavior of the reconstruction. The resulting distributions can be seen in Figure 6.31.
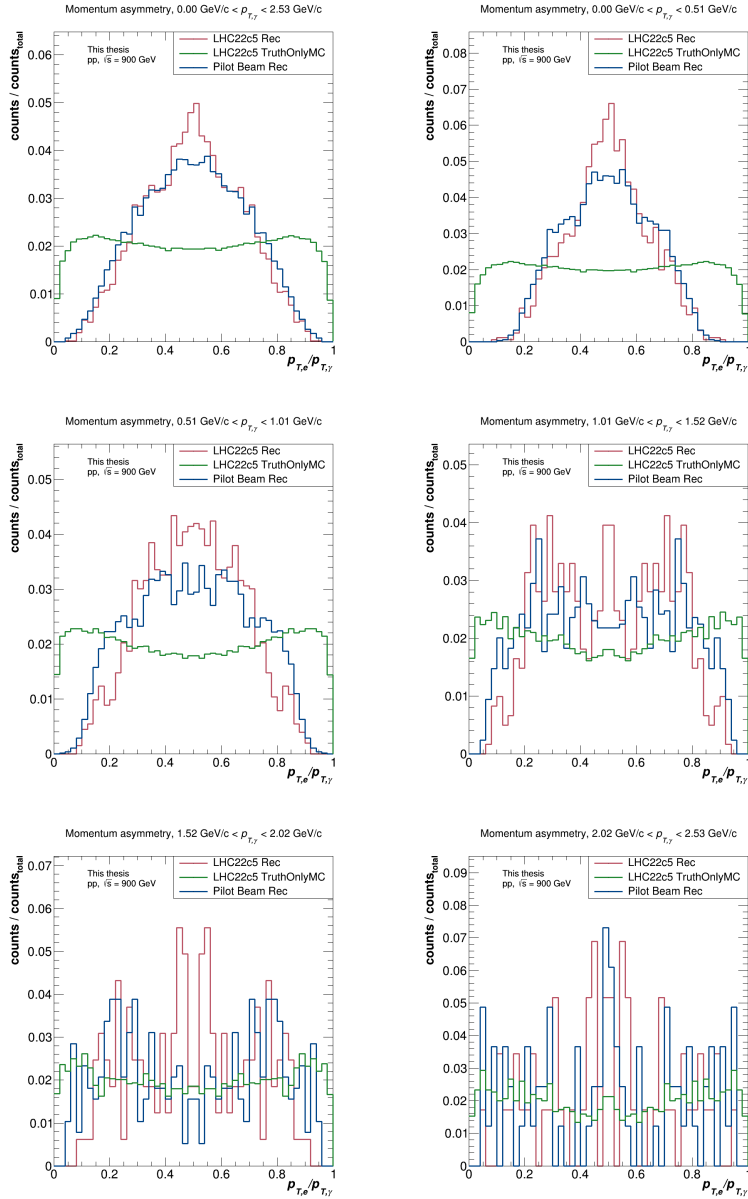
Figure 6.31: Distribution of the electron transverse momentum fraction for different transverse momentum ranges. All reconstructed photons Rec from LHC22c5 and the Pilot Beam as well as all converted photons TruthOnlyMC are shown. The distributions are normalized by the number of reconstructed and converted photons respectively.

The photons that are reconstructed in the Pilot Beam and Monte Carlo simulation have very similar distributions in all $p_{T,\gamma}$ ranges. However, they have significantly different shapes compared to the distribution of all converted photons. This effect is especially visible for low transverse momenta $p_{T,\gamma}$, while for higher momenta $p_{T,\gamma}$ it seems like the shapes of the distributions become more similar. Unfortunately there is only little statistical data available for higher momenta, which makes it hard to evaluate what is happening for high p_T. For low p_T it can be concluded, that the reconstruction of the photon conversion point works better with symmetric momenta of the electron positron pair and is therefore there are proportionally more reconstructed photon conversions with symmetric daughter transverse momentum than there should be.

6.8 Comparison of the Pilot Beam data and the anchored Monte Carlo simulation LHC22c5

Finally the Monte Carlo simulation LHC22c5 and the Pilot Beam data are compared to see if the measured data matches the expectation. For the comparison three variables are chosen:

- Conversion radius R

- Radial angle φ

- Transverse momentum p_T

Since LHC22c5 and the Pilot Beam have a different amount of collisions, the following distributions are normalized by the number of collisions $N_{\text{collisions}}$ in order to make them comparable. In Figure 6.32 one can see the conversion radius R of photons. As shown in subsection 6.4.1 the recalculated coordinates of the conversion point in the transverse plane provide a better resolution and thus will be used.
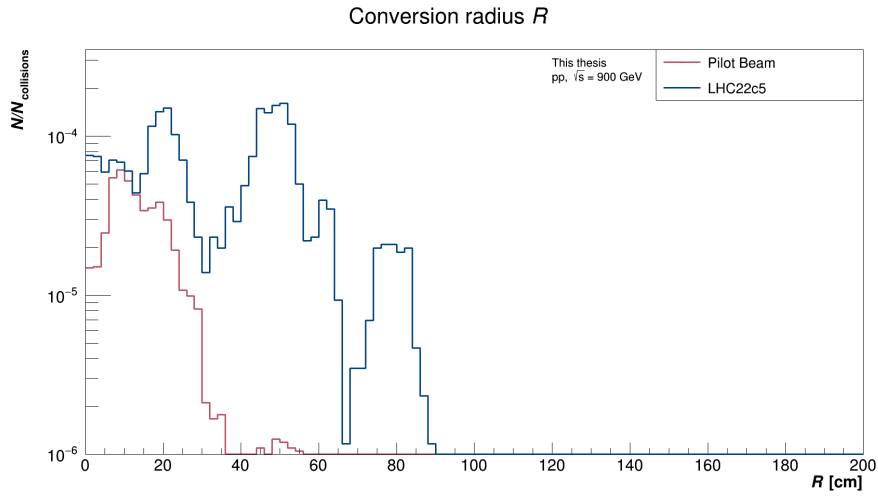
Figure 6.32: Recalculated conversion radius of the photon for LHC22c5 and Pilot Beam.

In the distribution of the conversion radius R in Figure 6.32 the distribution of the Monte Carlo is very different from the distribution of the Pilot Beam. First of all it is noticeable that there are a lot more reconstructed events per collision in the LHC22c5 data set. Moreover, there are almost no reconstructed photon conversions beyond a conversion radius of $R = 40\,\text{cm}$ for the Pilot Beam, whereas the distribution of LHC22c5 goes up until a conversion radius of $R = 90\,\text{cm}$. In Figure 6.33 the ratio of the Pilot Beam and LHC22c5 is shown.

One can see that the ratio first is at 0.2 for $R < 7\,\text{cm}$, then it rises nearly to 1 and then drops again to almost 0. The most probable causes for this discrepancy are:

- Incorrect calibration of the detector

- Problems with the matching of ITS and TPC tracks, given that the amount of reconstructed conversion points rapidly decline approximately where the border of the two detectors is at 40 cm. This can also be a result of calibration issues

81

- Problems with the reconstruction of the photon conversion point as discussed in previous chapters.

Ratio of LHC22c5 and Pilot Beam for conversion point
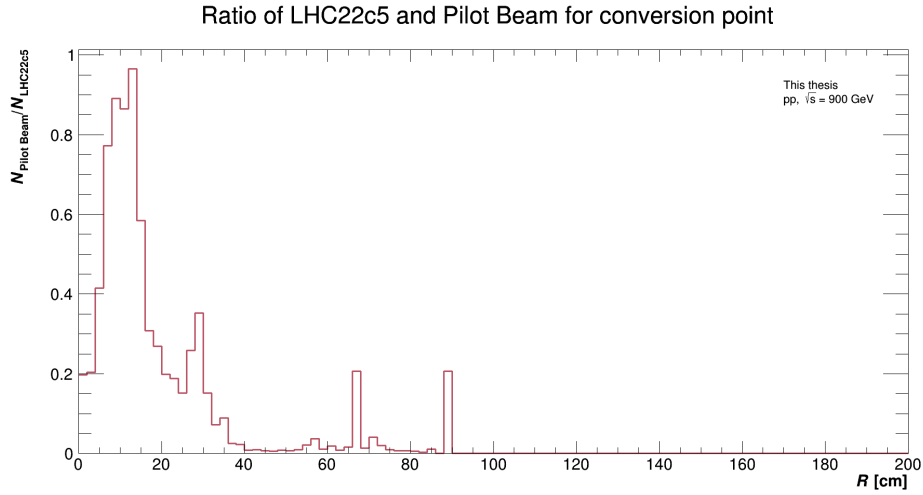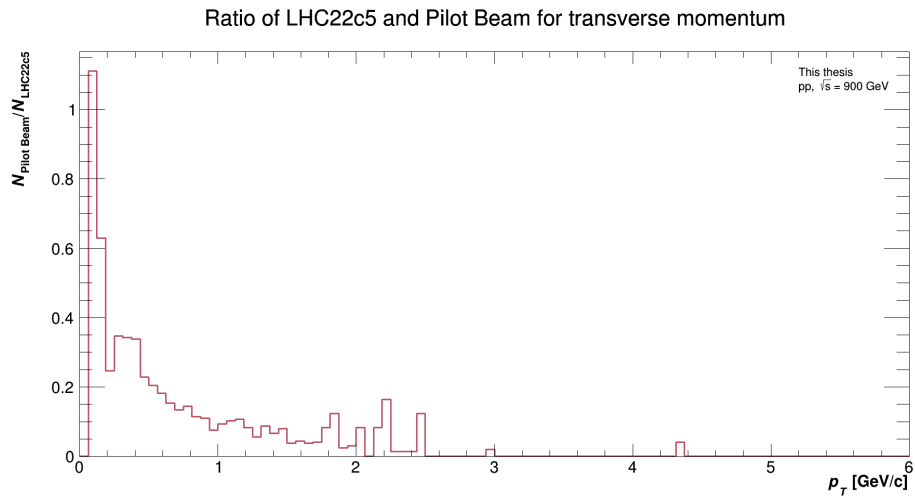

Figure 6.33: Ratio of Pilot Beam and LHC22c5 as a function of the recalculated conversion radius. The amounts of Pilot Beam and LHC22c5 photons are normalized by the number of corresponding collisions.

In Figure 6.34 the azimuth distribution is shown.

Radial angle φ
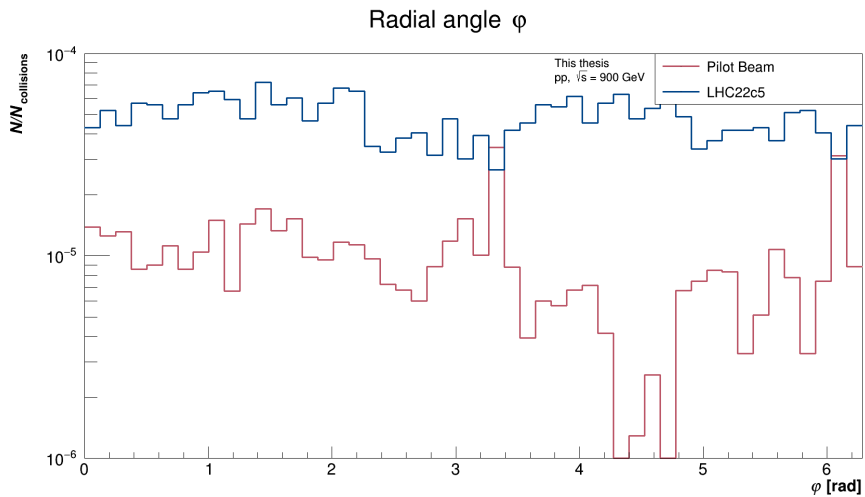
Figure 6.34: Azimuth distribution of the reconstructed photon conversion point for LHC22c5 and Pilot Beam.

Apart from the obvious difference in the number of reconstructed photons per collision the two distributions seem to be very similar in shape. However, the Pilot Beam data shows a dip at approximately $\varphi = 4.5\,\mathrm{rad}$ that the LHC22c5 does not contain. This might be the result of bad resolution due to the flawed reconstruction of the conversion point or the result of non-functional areas in the detector during the Pilot Beam that are not properly included in the Monte Carlo simulation.

In Figure 6.35 the distribution of the transverse momentum can be seen.
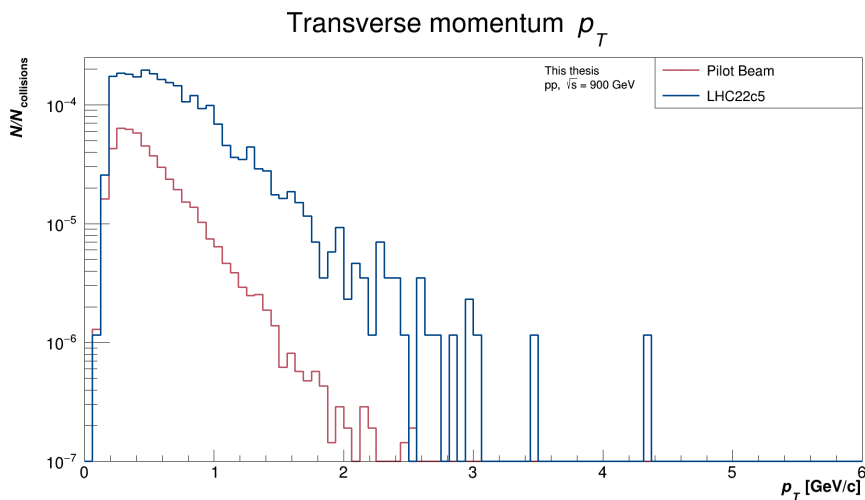
Figure 6.35: Transverse momentum distribution for reconstructed photons in LHC22c5 and Pilot Beam.

The distributions for the transverse momenta not only seem to differ in the number of events like already mentioned but also in the shape. In order to verify this the ratio was calculated and can be seen in Figure 6.36. One can see that the ratio is not constant throughout the whole transverse momentum range, which endorses the fact that there is a difference in the reconstruction of the Pilot Beam data and the LHC22c5 Monte Carlo simulation. It would be very beneficial to compare real data with Monte Carlo for a larger data sample and for stronger magnetic field strengths.

Figure 6.36: Ratio of Pilot Beam and LHC22c5 as a function of the transverse momentum. The amounts of Pilot Beam and LHC22c5 photons are normalized by the number of corresponding collisions.

7 | Conclusions and Outlook

The work of this thesis consists for the most part in further developing the O²Physics software for photon reconstruction and writing macros for analyzing and validating the state of the photon reconstruction using the photon conversion method. Based on the provided results it was demonstrated that the established analysis chain can be successfully used to research photon conversions for different data sets and Monte Carlo simulations using the official Hyperloop system. Furthermore, a recalculation of the photon conversion point in the photon conversion method was successfully implemented.

In the analysis chapter 6 the Monte Carlo simulation LHC22c5 and the Pilot Beam data were researched. First the implementation of the detector material was evaluated. It was concluded that, while most of the detector material is implemented correctly, there are some missing major parts like the full azimuth implementation of the ITS-MFT cage, which is in addition to that misaligned.

A conversion probability of on average 8.4 % for the total transverse momentum range and 10.7 % for a range of $1\,\mathrm{GeV} < p_T < 4\,\mathrm{GeV}$ were calculated for the radial range of $0\,\mathrm{cm} < R < 180\,\mathrm{cm}$. Taking only the range of the ITS2 into account, which corresponds to a range of $0\,\mathrm{cm} < R < 42\,\mathrm{cm}$, the conversion probability was determined to be 2.2 % for the whole momentum range and 4.2 % for the momentum range of $1\,\mathrm{GeV} < p_T < 4\,\mathrm{GeV}$.

In section 6.3 the effects of track quality, PID and photon selection cuts were studied. It was found that after applying the cuts 78 % of the V^0s that pass these cuts are true photon conversions. Most contamination comes from electron positron pairs that were matched but don't belong to the same mother particle and matching of tracks of particles with the same charge. The second source of contamination seemed to be relatively large and should be further investigated in a consecutive analysis.

In the spacial resolution subsection 6.4.1 it was concluded that the recalculation of the conversions point coordinates is benefiting the resolution as a whole. On the one had it improves the resolution of the conversion radius R by a factor of (1.73 ± 0.05) and eliminates biases in the Z

coordinate, but on the other hand it makes the resolution worse for the Z coordinate. However, it was determined that this decrease in resolution is insignificant for the Z coordinate as a whole, since the Z distribution of the conversion point is proportionally very wide. Nevertheless, it should be noted that the resolution of R is still insufficient to match conversion points that were reconstructed using true Monte Carlo information. It would be beneficial to further investigate this with more data and higher magnetic field strengths of $0.5\,\text{T}$ compared to the $0.2\,\text{T}$ used in the pilot beam.

Furthermore, the reconstruction efficiency in section 6.6 was calculated to 0.42 % for the whole transverse momentum range and to 4.76 % for the range of $1.5\,\text{GeV} < p_T < 3\,\text{GeV}$, where it is the highest. After a thorough investigation it was concluded that the most likely cause for the low reconstruction efficiency lies in V^0 finder algorithm or in the calibration.

From the studies of the fractional electron momentum distribution it was observed that for lower transverse momenta p_T the reconstruction seems to work better for more symmetrical distributed transverse momenta of the electrons. This information can provide further clues in the investigation of the low reconstruction efficiency.

Finally, the LHC22c5 Monte Carlo simulation was compared to the Pilot Beam data. It was found that there are less reconstructed photon conversions per collision in the Pilot Beam than in the simulation by approximately an order of magnitude. This big difference comes from the rapid loss of efficiency for $R > 15\,\text{cm}$.

The work carried out in this thesis can be extended by analyzing more data sets at higher collision energies with better statistics and stronger magnetic fields of $0.5\,\text{T}$. This might give clues why the $FWHM$ is increasing for the recalculation of the Z conversion point coordinate. Furthermore, the next step in photon analysis using the photon conversion method should be to improve to V^0 finder to increase the amount of found V^0s. Additionally, the KFParticle package should be implemented in the photon conversion method for Run 3 as it was done in Run 2. The KFParticle package provides the χ^2 as an additional selection criteria and

can be used to recalculate the momentum of V^0 particle at the conversion point. After that the photon conversion method can provide a basis in the reconstruction of mesons that decay into photons.
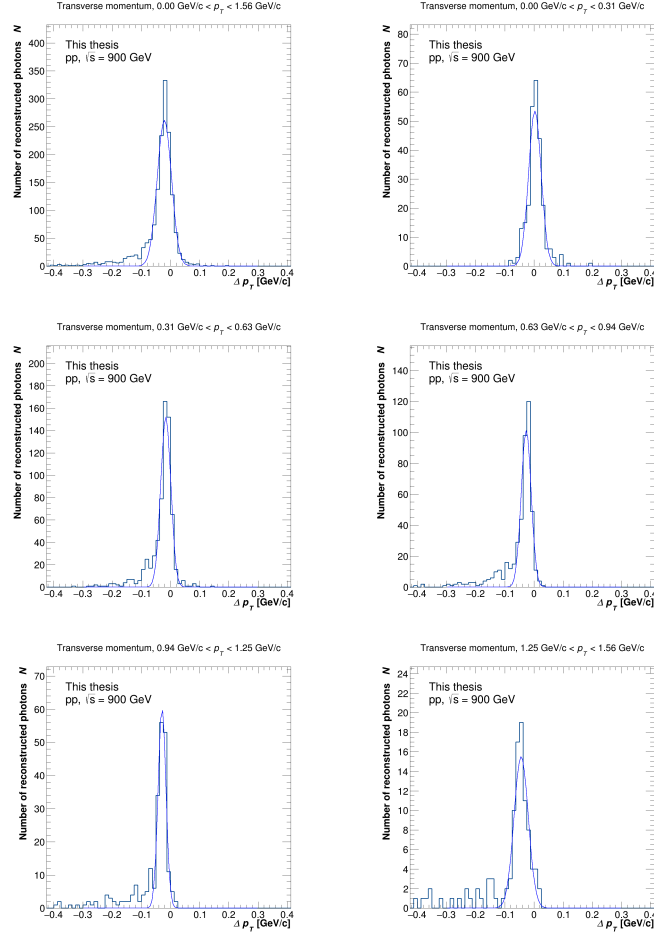
A | Appendix

Figure A.1: Projections of the Δp_T distributions for different ranges of p_T. Gaussian fits were performed to evaluate the distributions. The fit range was limited to ignore the contribution of the tail, which comes from Bremsstrahlung of tracks. LHC22c5 used.
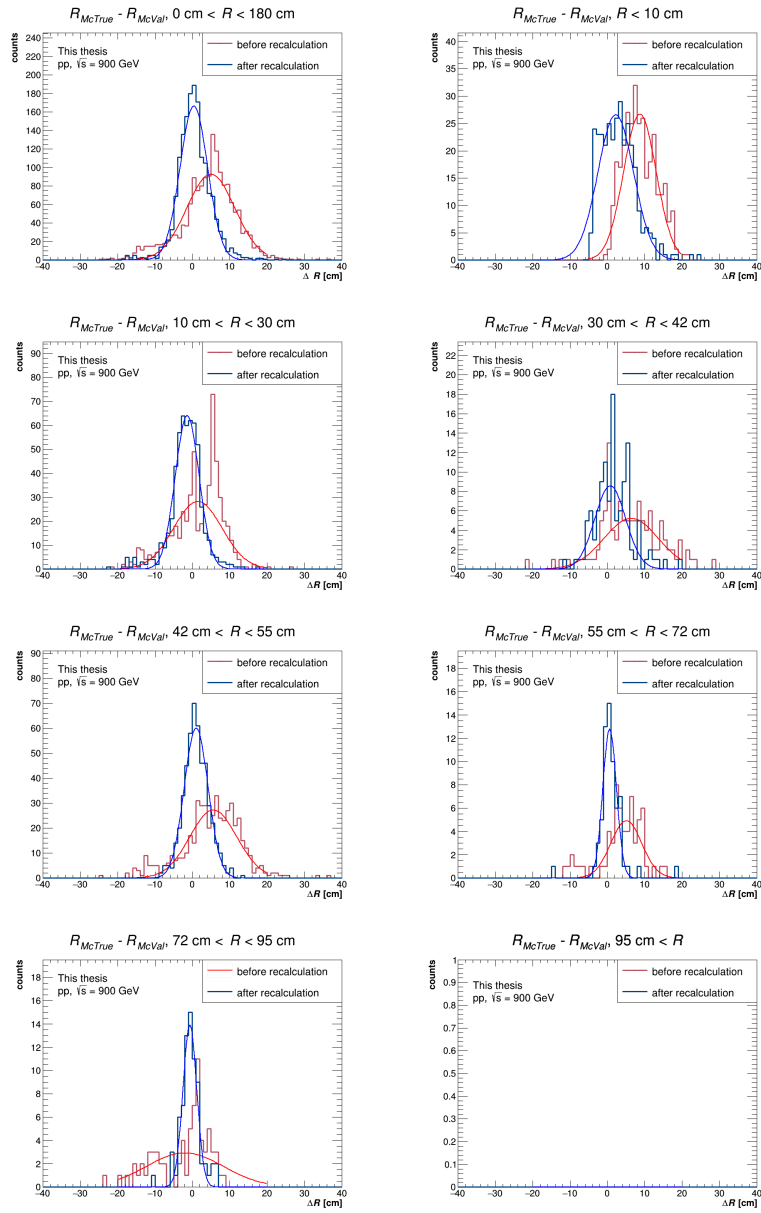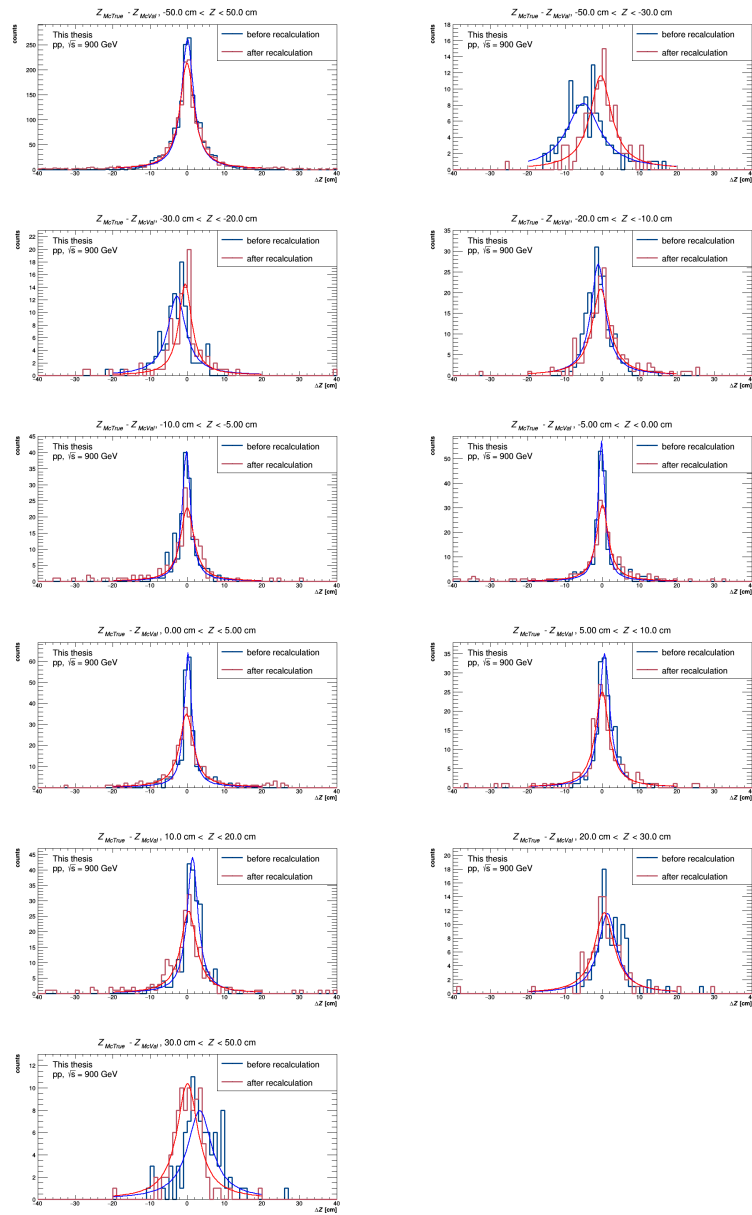
Figure A.2: Projections of the ΔR distributions for different ranges of R. Gaussian fits were performed to evaluate the distributions. LHC22c5 used.

Figure A.3: Projections of the ΔZ distributions for different ranges of Z. Lorentz function fits were performed to evaluate the distributions. LHC22c5 used.
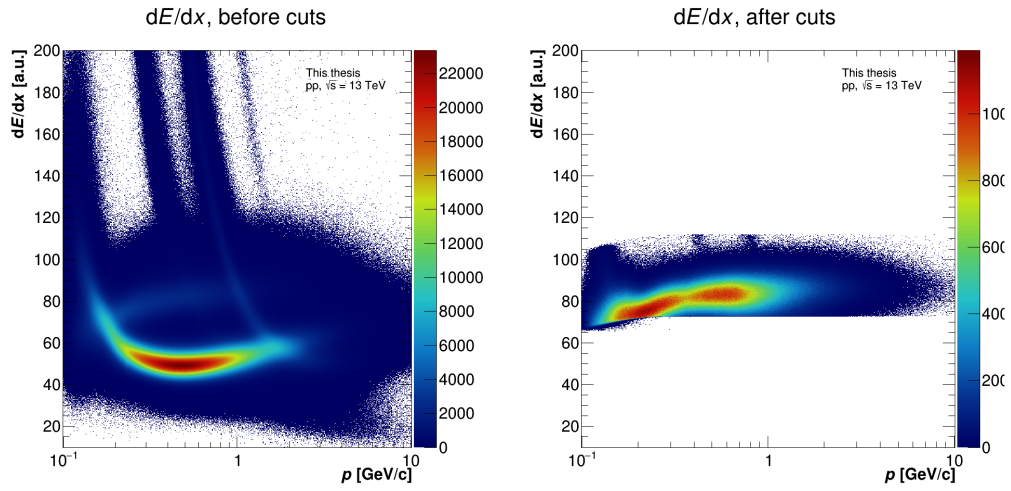
Figure A.4: Ionization energy loss for both tracks belonging to a V^0 candidate. LHC21k6 before and after applying track quality, PID and photon selection cuts.
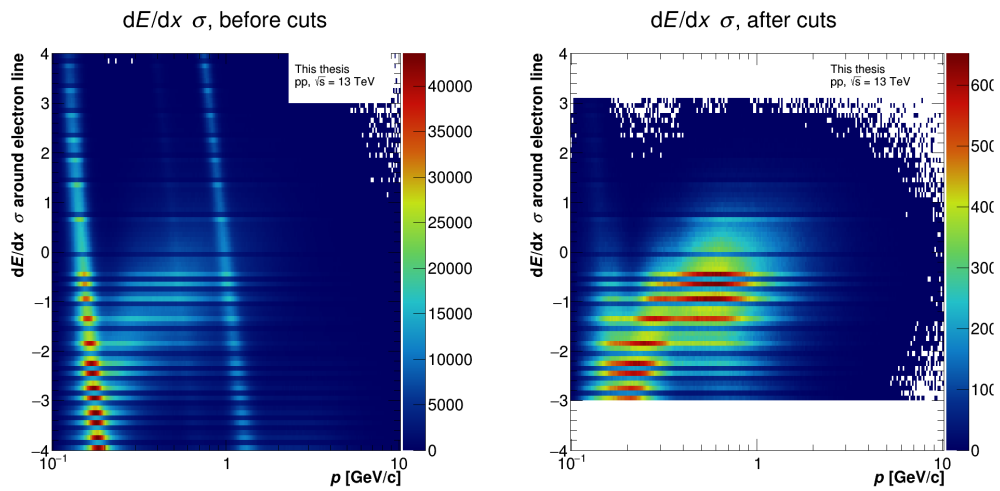
Figure A.5: Track quality around the electron line for LHC21k6 before and after applying track quality, PID and photon selection cuts.
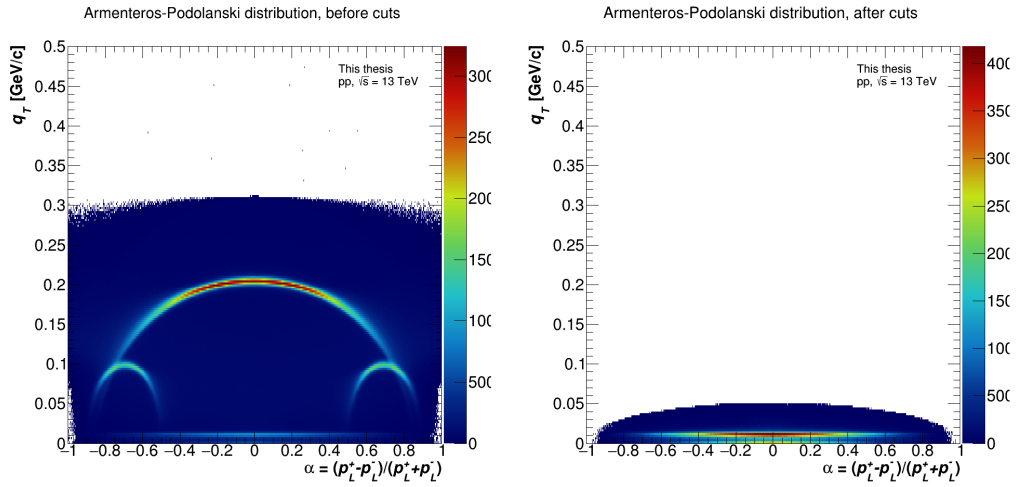
Figure A.6: Armenteros-Podolanski distribution for LHC21k6 before and after applying track quality, PID and photon selection cuts.
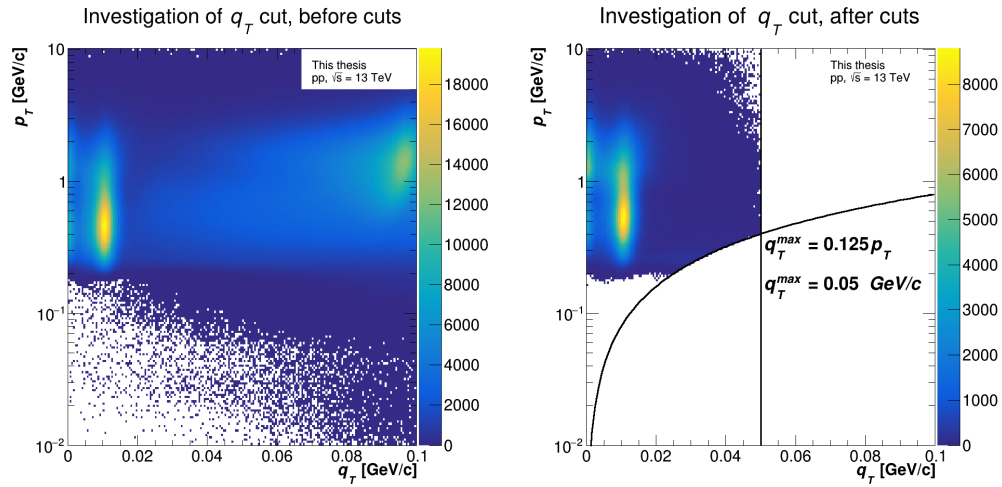
Figure A.7: Transverse momentum q_T of the two tracks vs. transverse momentum p_T of the V^0 for LHC21k6. Black lines are the cuts that were used to eliminate contamination.
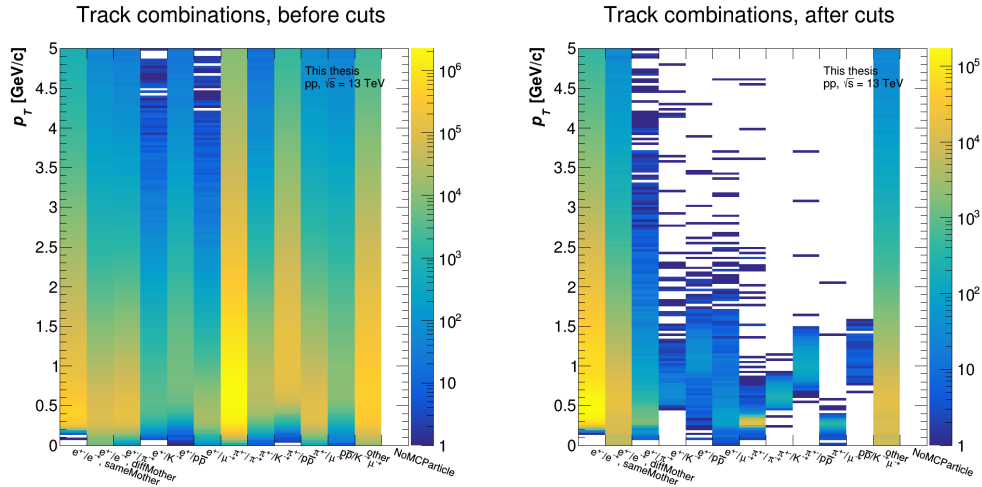
Figure A.8: Monte Carlo daughter track combinations of reconstructed V^0s as a function of the transverse momentum p_T before and after applying track quality, PID and photon selection cuts for LHC21k6.
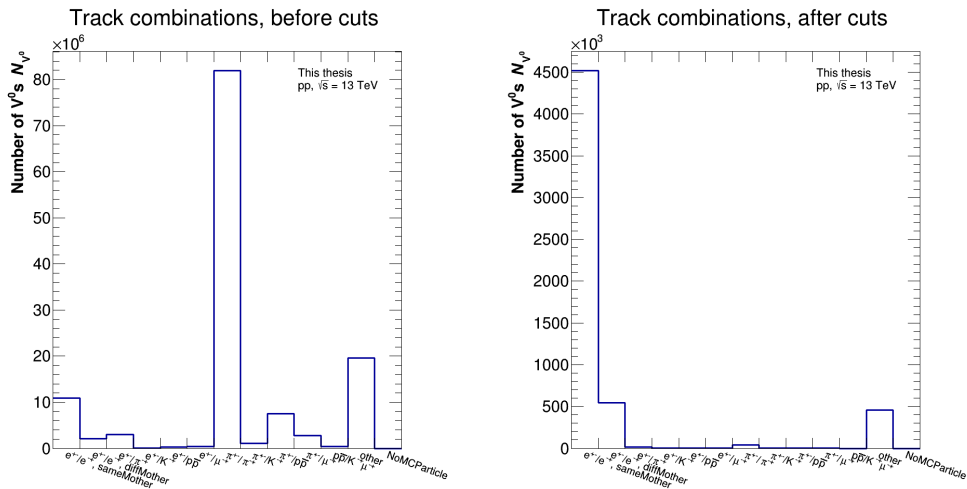
Figure A.9: Monte Carlo daughter track combinations of reconstructed V^0s before and after applying track quality, PID and photon selection cuts for LHC21k6.
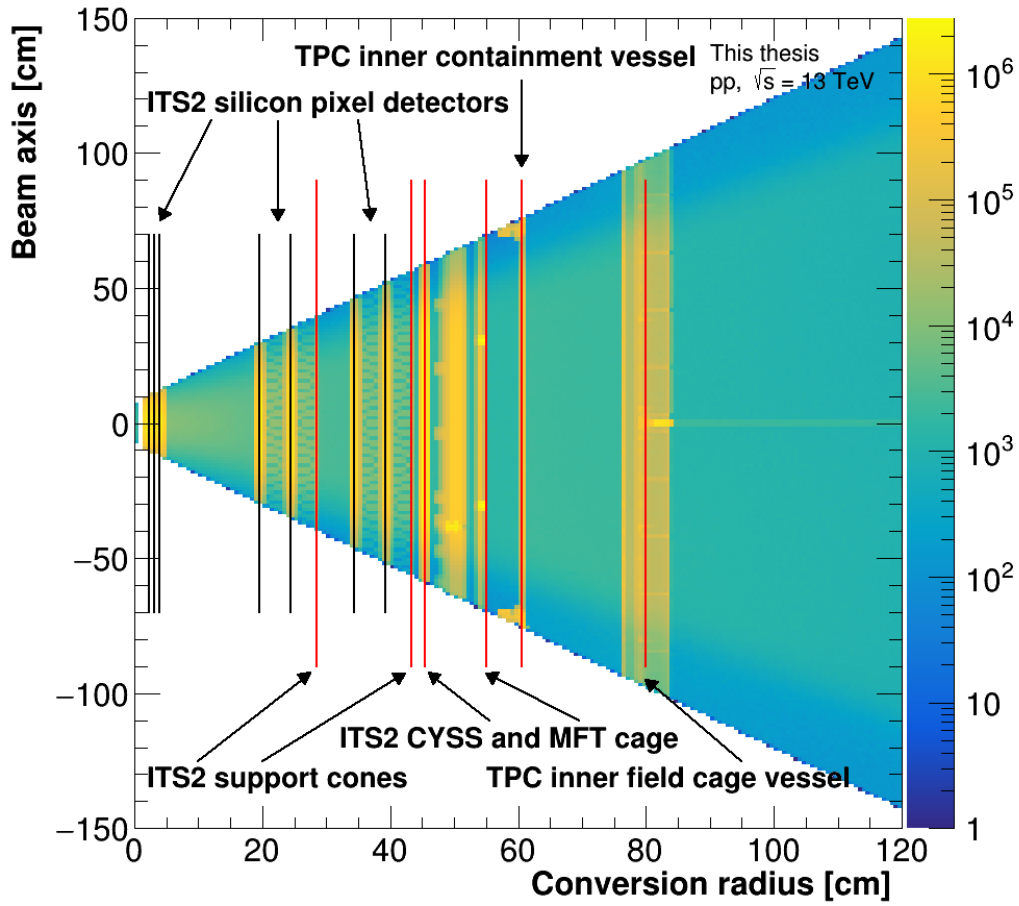
Figure A.10: Conversion point coordinates Z vs. R for all TruthOnlyMc photons in LHC21k6. Lines represent locations of ALICE components.
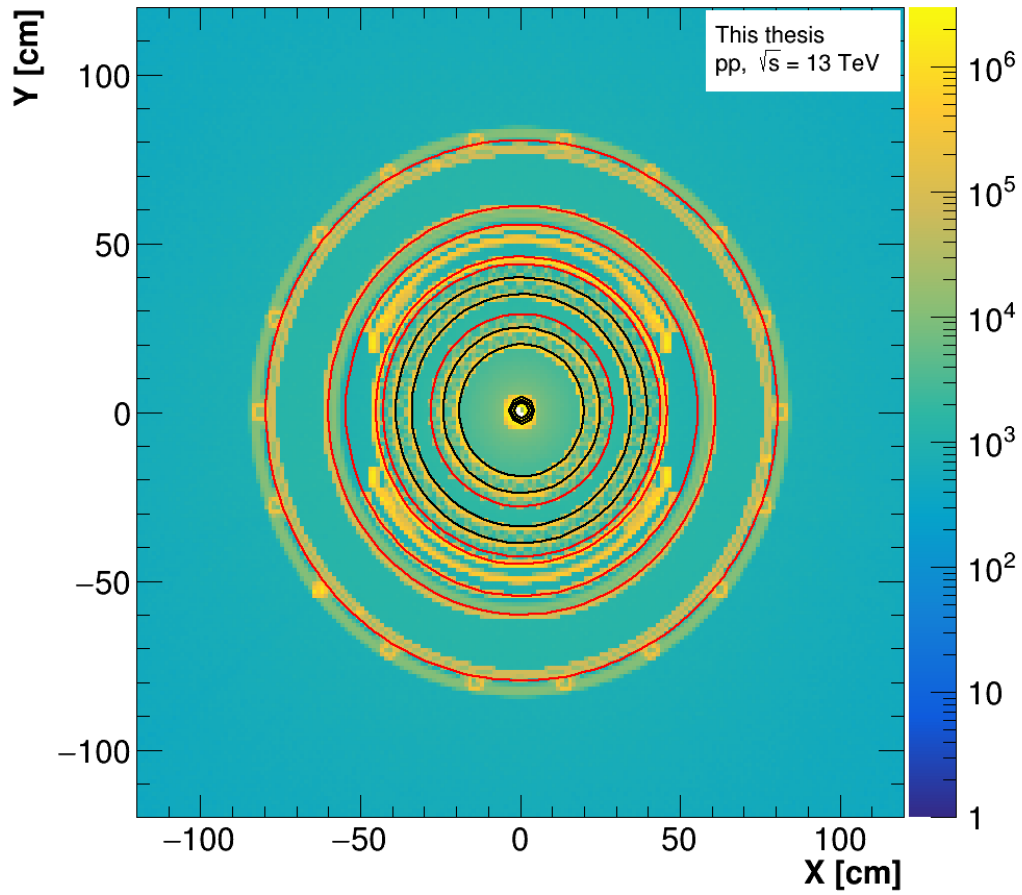
Figure A.11: Conversion point coordinates *Y* vs. *X* for all TruthOnlyMc photons in LHC21k6. Lines represent locations of ALICE components.
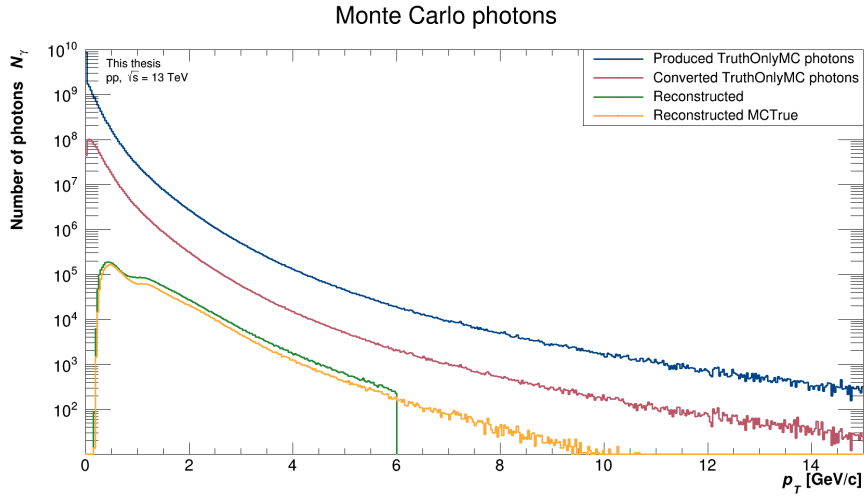
Figure A.12: Amount of photons for the respective distribution is shown over p_T. The distribution for total and converted photons come from the *gammaConversionTruthOnly* task, whereas the distribution for the reconstructed and MCTrue photons is provided by the *GammaConversion* task. LHC21k6 Monte Carlo used.
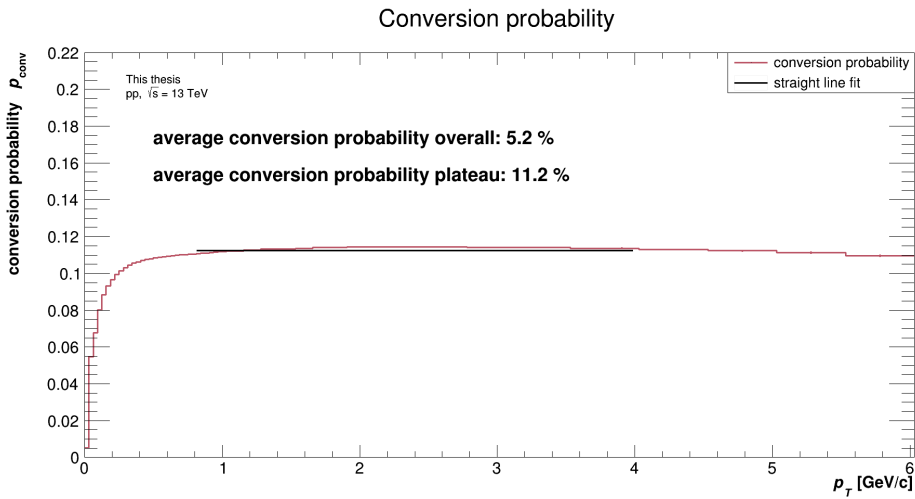
Figure A.13: Conversion probability of photons, calculated by dividing the amount of converted photons by the amount of produced photons for the range of $0\,\mathrm{cm} < R < 180\,\mathrm{cm}$ for LHC21k6.
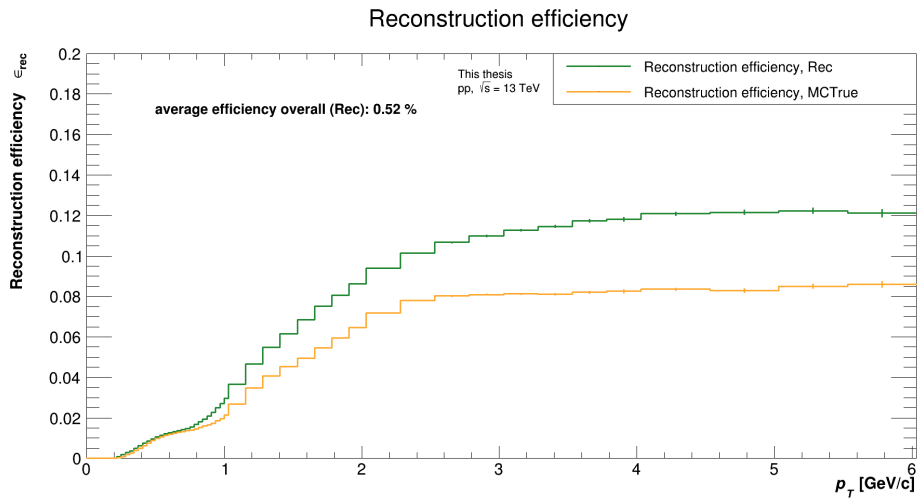
Figure A.14: Reconstruction efficiency for photons. Calculated by dividing the amount of reconstructed photons by the amount of converted photons for LHC21k6.
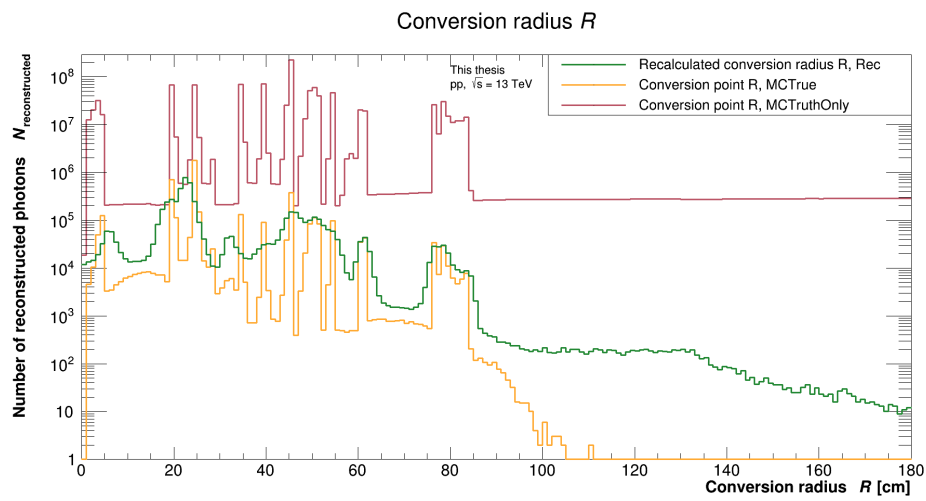

Figure A.15: Amount of converted and reconstructed photons as a function of R for LHC21k6.
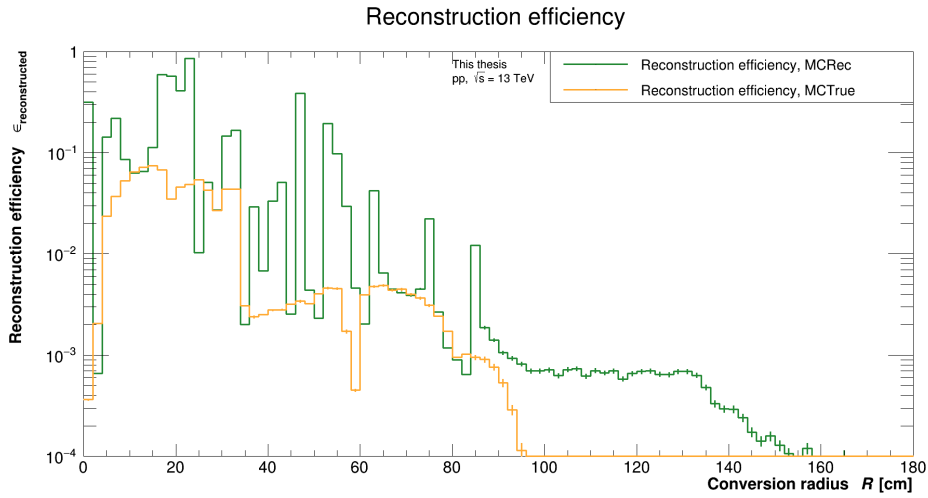
Figure A.16: Reconstruction efficiency of MCRec and MCTrue as a function of R. Calculated by dividing the respective distribution by the amount of converted photons for LHC21k6.
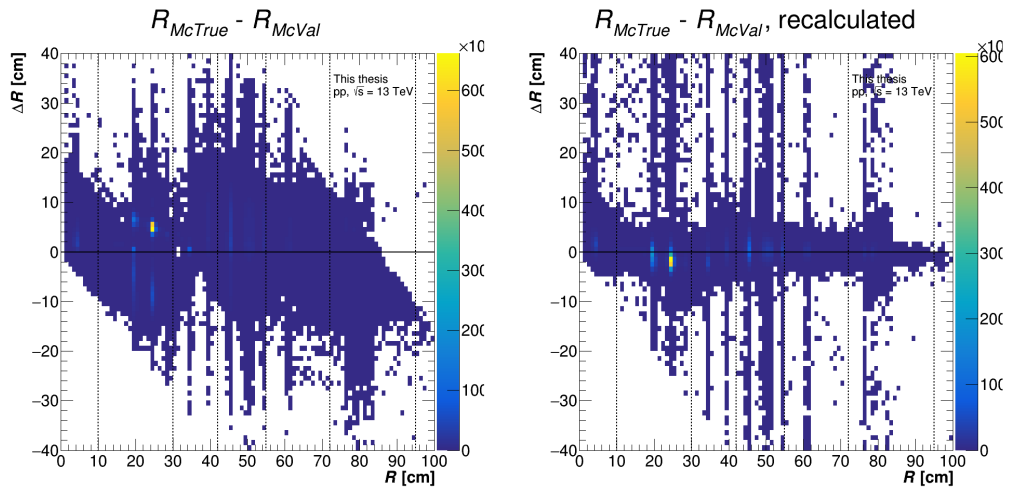

Figure A.17: ΔR v.s. R before and after recalculation for LHC21k6 dataset after applying PID and photon selection cuts. Lines represent areas that are projected to in the corresponding one dimensional plot Figure A.18.
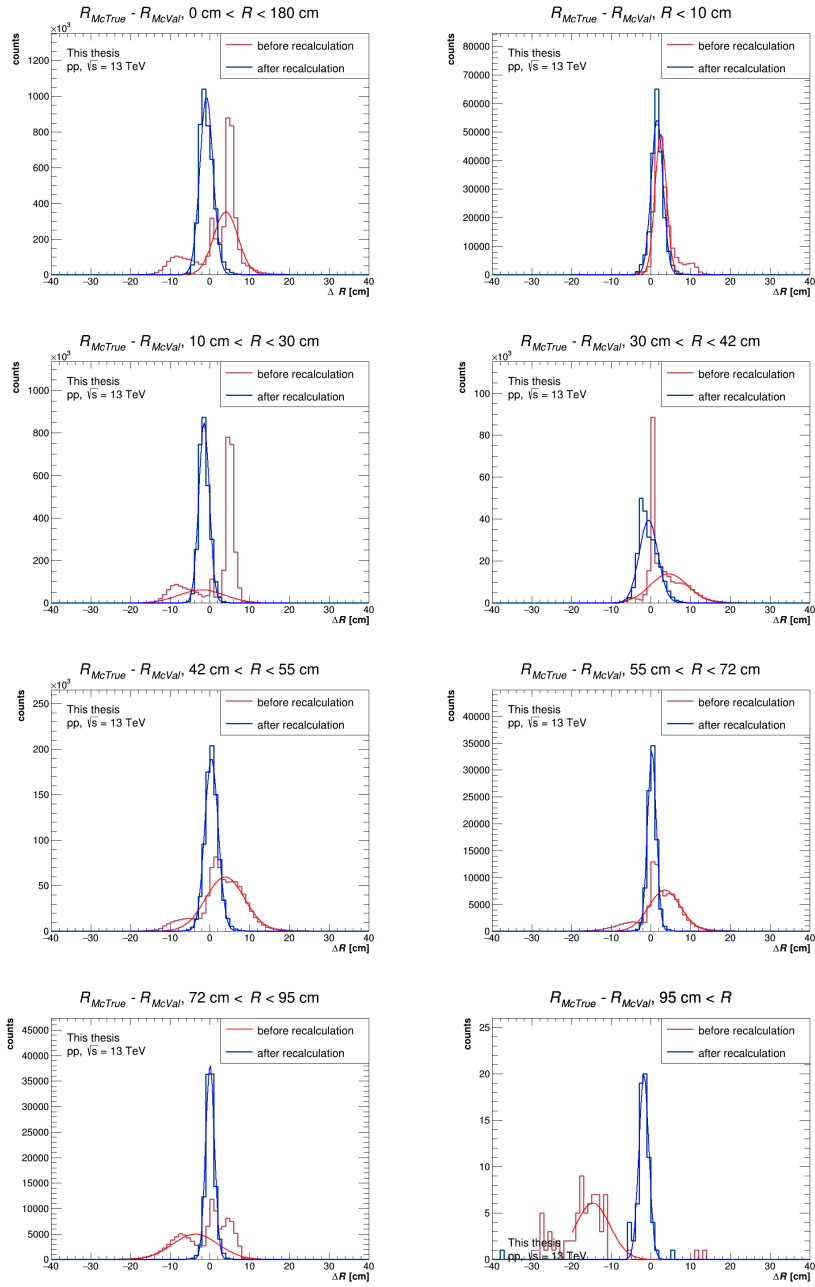
Figure A.18: Projections of the ΔR distributions for different ranges of R. Gaussian fits were performed to evaluate the distributions. LHC21k6 used.
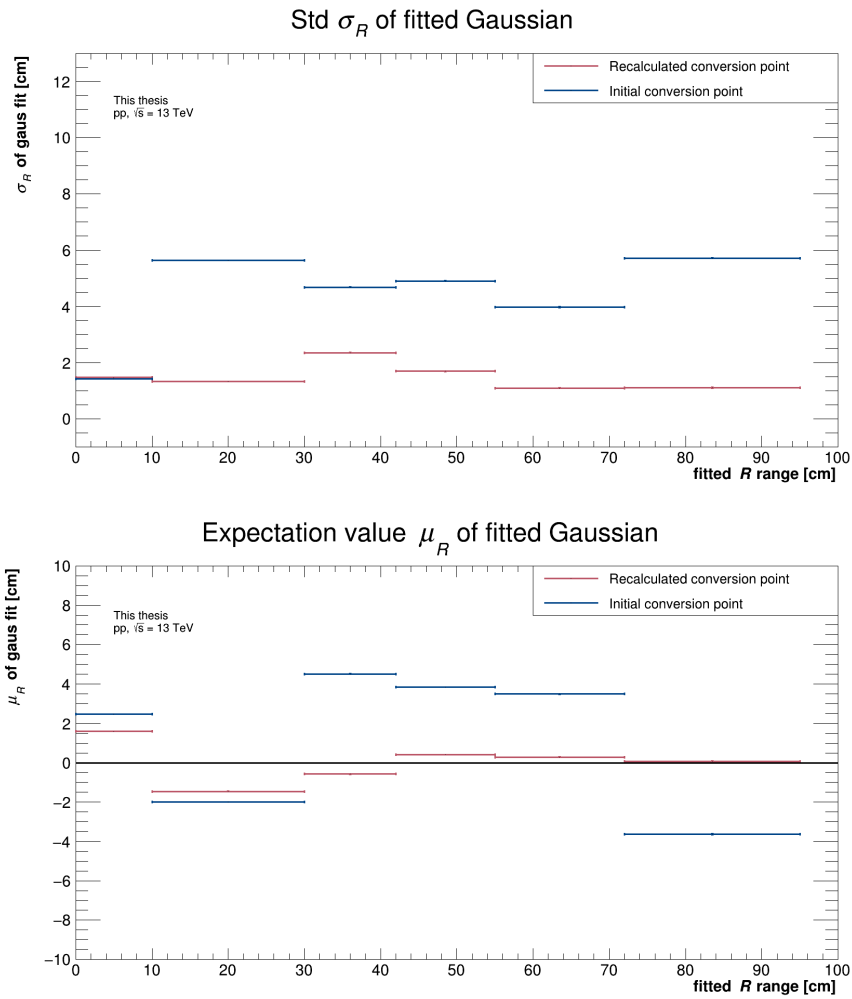
Figure A.19: Fit parameters for Gaussian fits, that were performed for different R ranges. Horizontal bars represent the fit range and vertical bars represent the error of the fit parameter. LHC21k6 used.
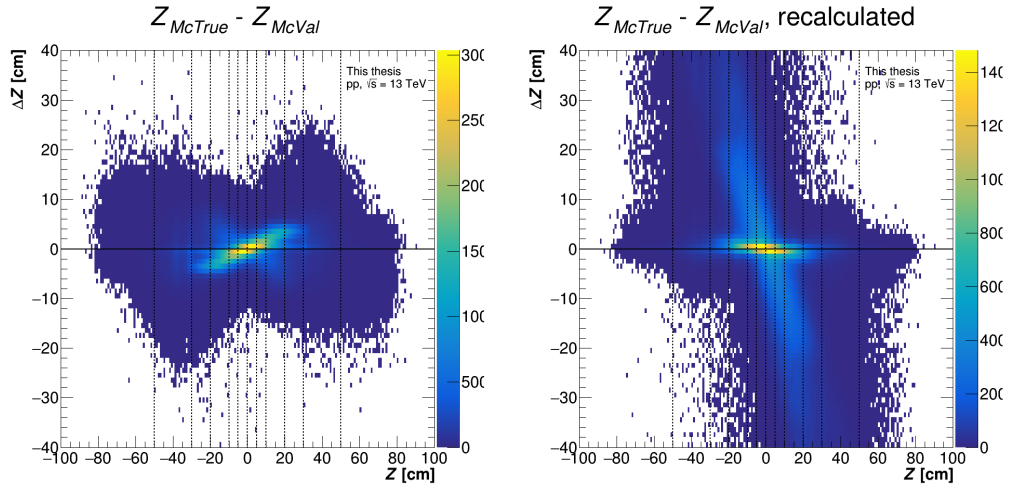
Figure A.20: ΔZ vs. Z before and after recalculation for LHC21k6 dataset after applying PID and photon selection cuts. Lines represent areas that are projected to in the corresponding one dimensional plot Figure A.22.
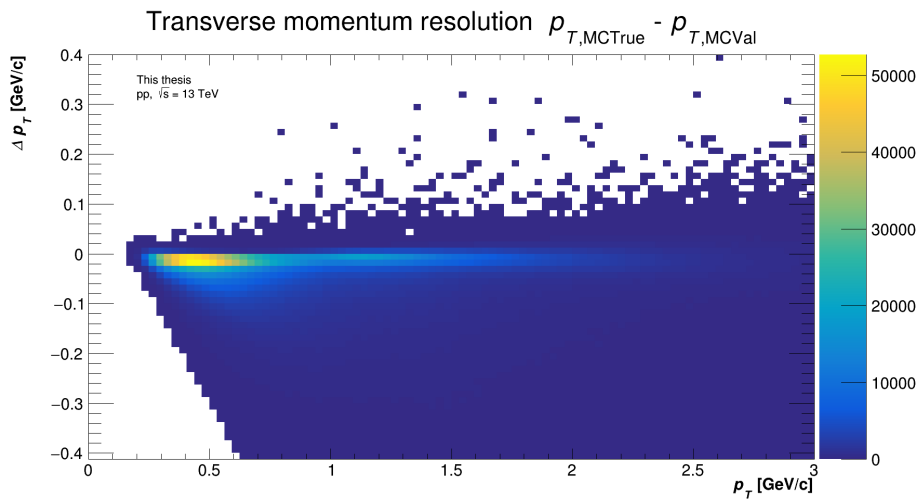

Figure A.21: Resolution Δp_T vs. transverse momentum p_T of reconstructed photons for LHC21k6.
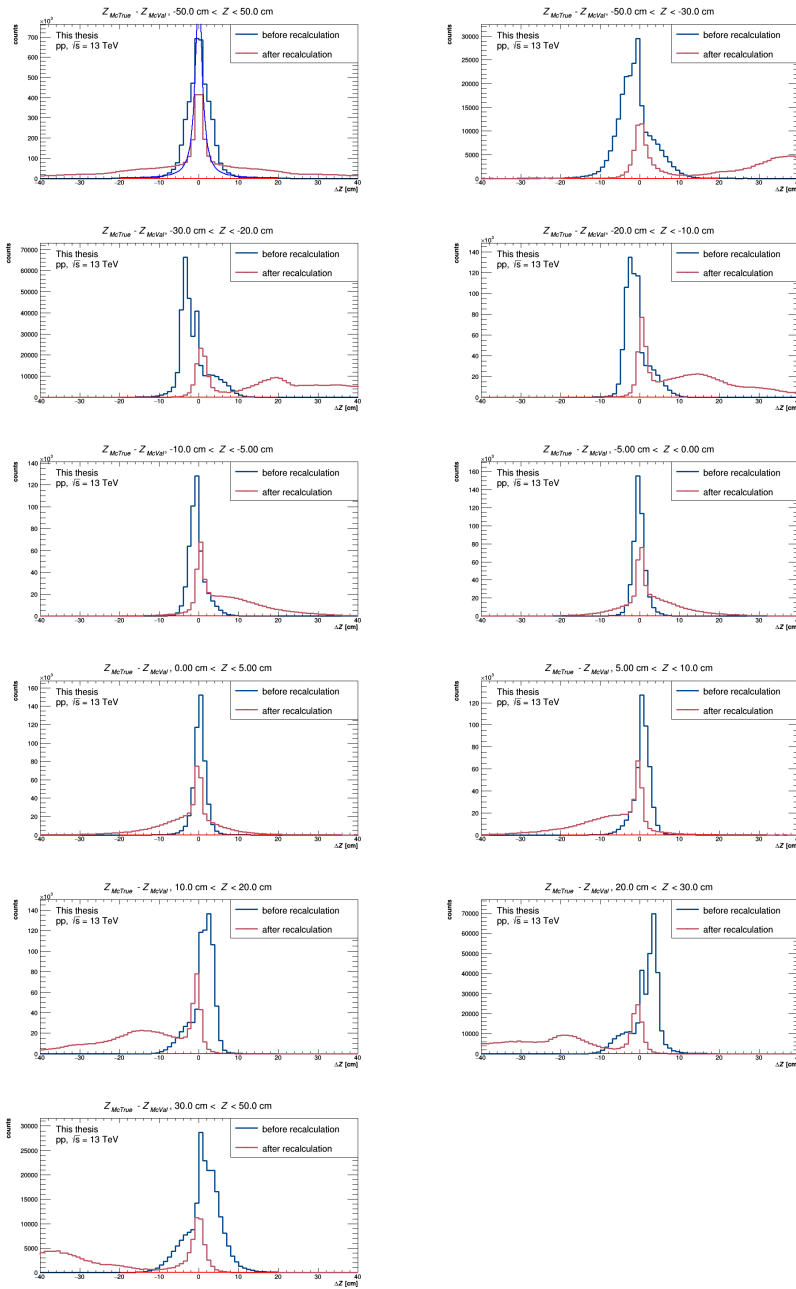
Figure A.22: Projections of the ΔZ distributions for different ranges of Z. Lorentz function fits were performed to evaluate the distributions. LHC21k6 used.
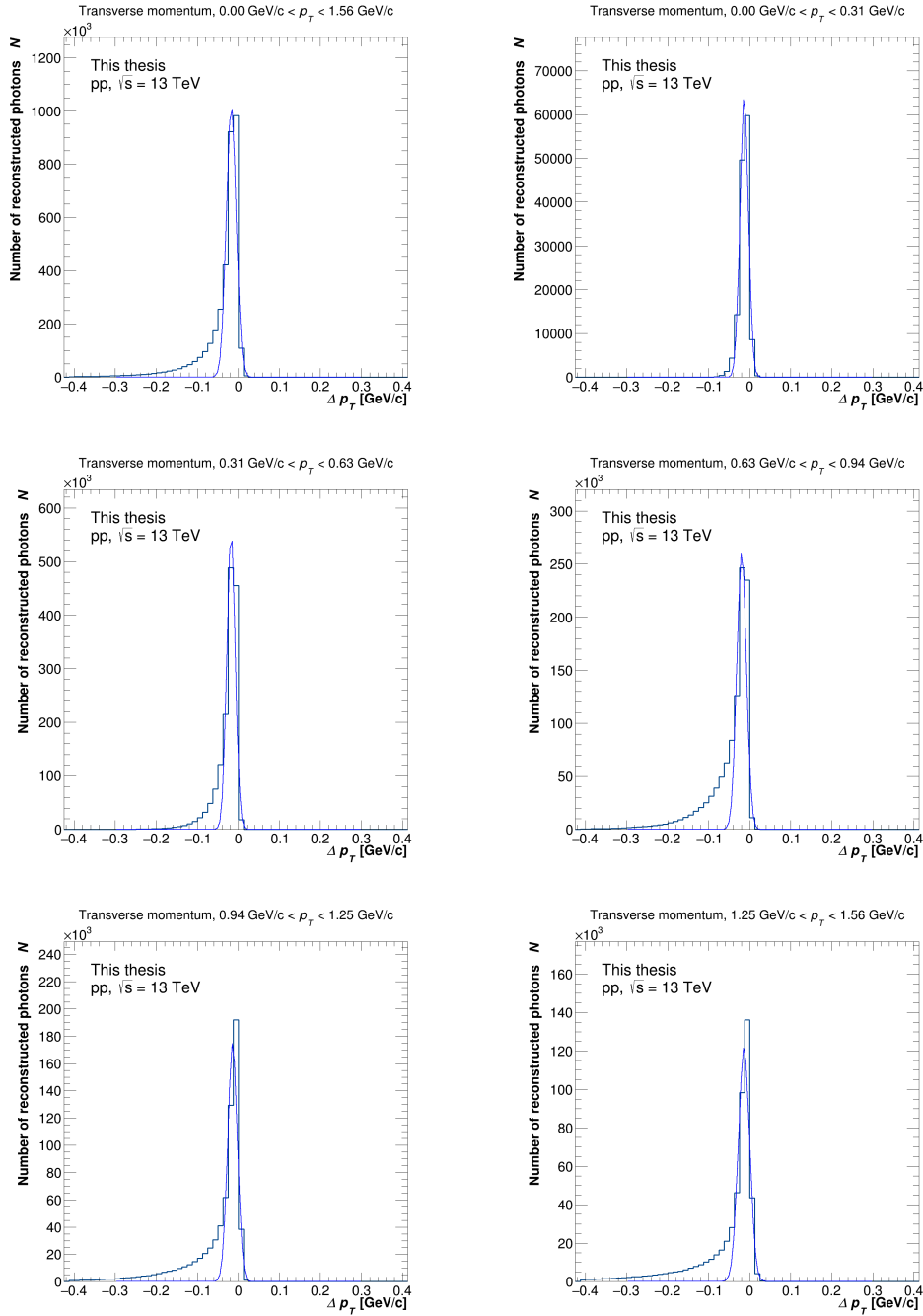
Figure A.23: Projections of the Δp_T distributions for different ranges of p_T. Gaussian fits were performed to evaluate the distributions. The fit range was limited to ignore the contribution of the tail, which comes from Bremsstrahlung of tracks. LHC21k6 used.
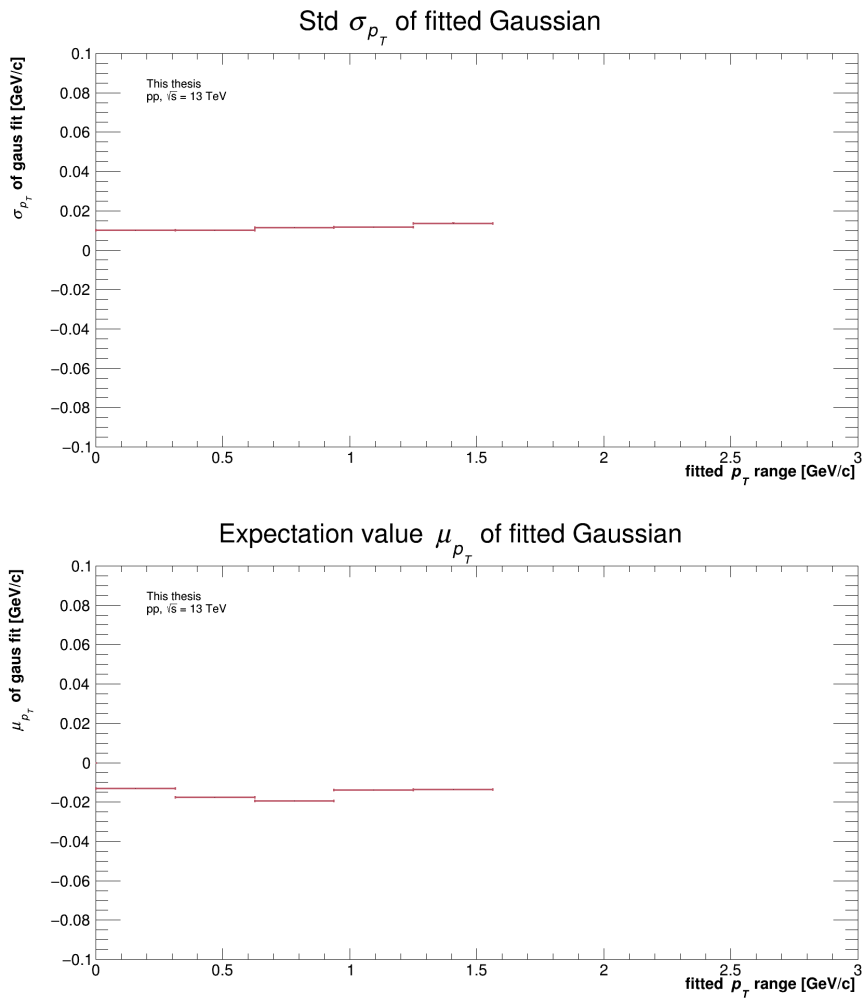
Figure A.24: Fit parameters for Gaussian fits, that were performed for different p_T ranges. Horizontal bars represent the fit range and vertical bars represent the error of the fit parameter. LHC21k6 used

Figure A.25: Fractional electron transverse momentum vs. transverse momentum for all reconstructed photons in LHC21k6.
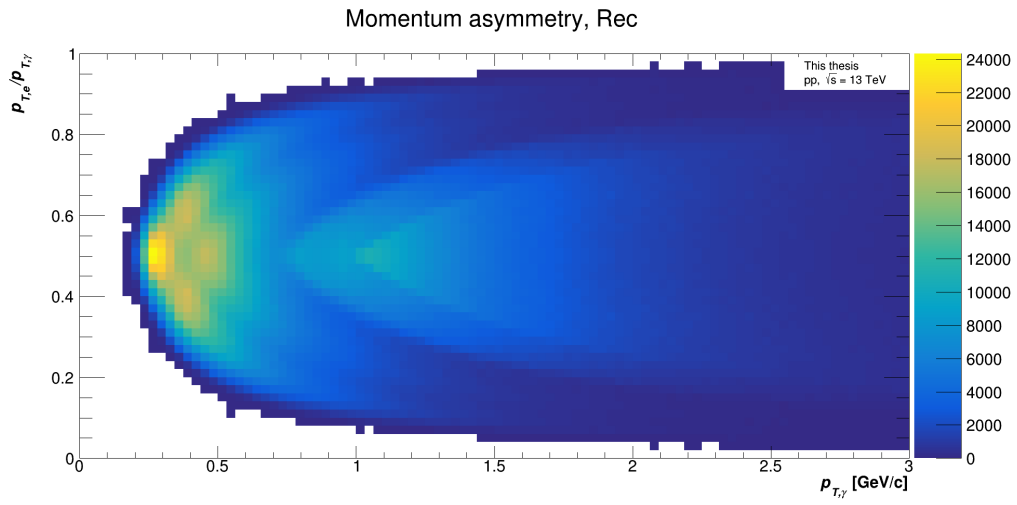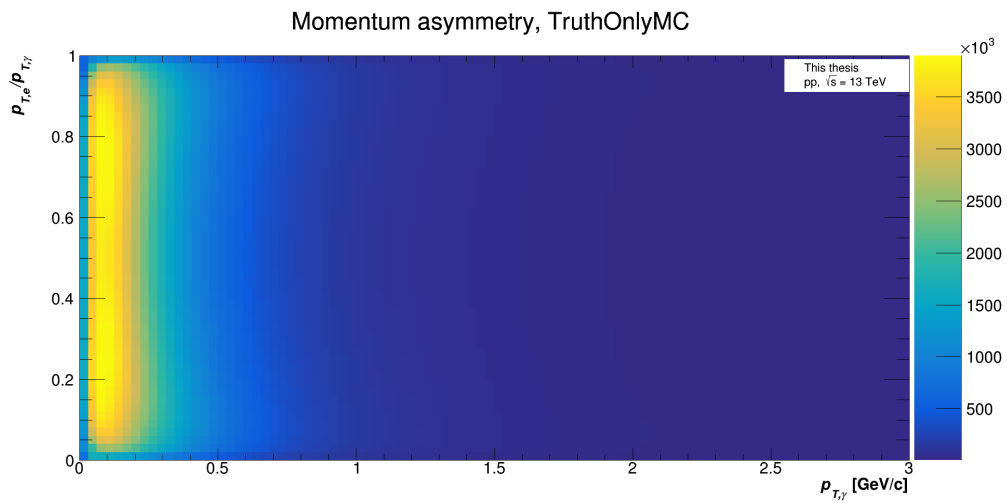

Figure A.26: Fractional electron transverse momentum vs. transverse momentum of all converted photon in LHC21k6.
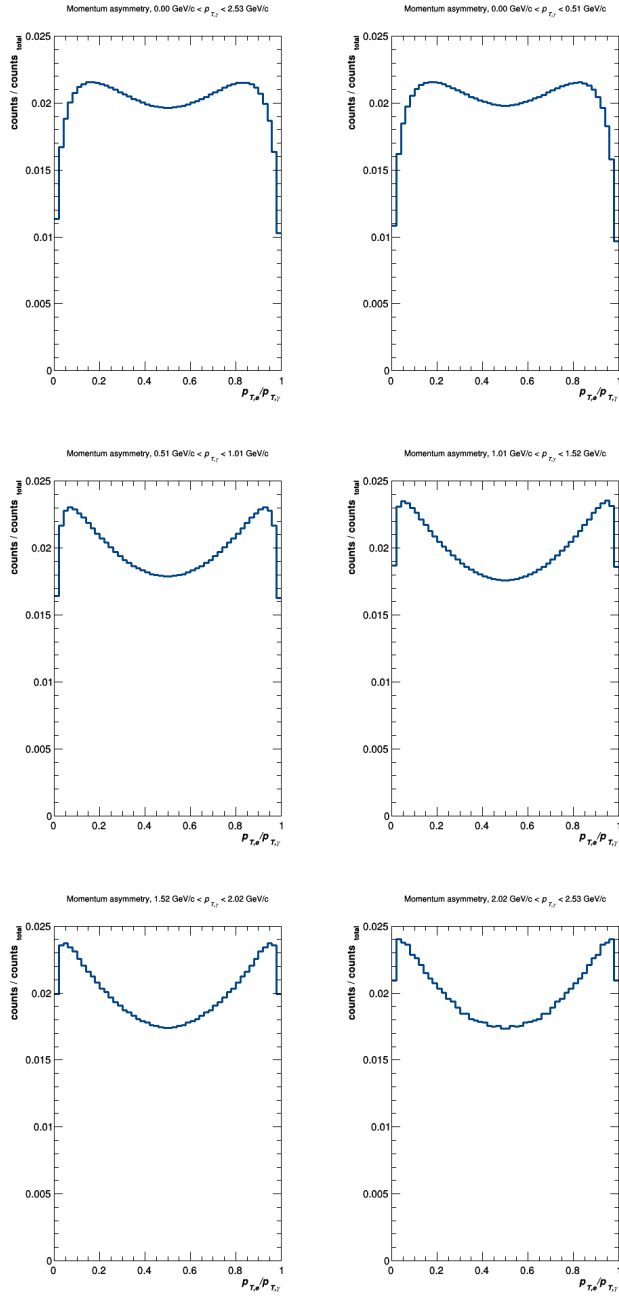
Figure A.27: Distribution of the electron transverse momentum fraction for different transverse momentum ranges. All converted photons TruthOnlyMC from LHC21k6 are shown. The distributions are normalized by the number of reconstructed and converted photons respectively.

Bibliography

[1] *The Standard Model.* URL: https://home.cern/science/physics/standard-model. (accessed: 15.07.2022).

[2] Daniel Dominguez. "Standard Model. Le modèle standard". In: (Mar. 2015). General Photo. URL: https://cds.cern.ch/record/2002395.

[3] *Heavy ions and quarck-gluon plasma.* URL: https://home.cern/science/physics/heavy-ions-and-quark-gluon-plasma. (accessed: 15.07.2022).

[4] D. Boyanovsky, H.J. de Vega, and D.J. Schwarz. "Phase Transitions in the Early and Present Universe". In: *Annual Review of Nuclear and Particle Science* 56.1 (Nov. 2006), pp. 441–500. DOI: 10.1146/annurev.nucl.56.080805.140539. URL: https://doi.org/10.1146%2Fannurev.nucl.56.080805.140539.

[5] Antonin Maire. "Phase diagram of QCD matter : Quark-Gluon Plasma". General Photo. June 2015. URL: https://cds.cern.ch/record/2025215.

[6] *Quenching jets in hot dense matter from lead-ion collisions.* accessed 29.08.2022. URL: https://home.cern/fr/node/4820.

[7] Meike Charlotte Danisch. "Measurement of neutral mesons and direct photons in Pb-Pb collisions at $\sqrt{s_{NN}}$ = 5.02 TeV with ALICE at the LHC". Presented 12 Jan 2022. Nov. 2021. URL: https://cds.cern.ch/record/2800150.

[8] Chun Shen and Ulrich Heinz. *The road to precision: Extraction of the specific shear viscosity of the quark-gluon plasma.* 2015. DOI: 10.48550/ARXIV.1507.01558. URL: https://arxiv.org/abs/1507.01558.

[9] Lucia Leardini. "Measurement of neutral mesons and direct photons in Pb-Pb collisions at $\sqrt{s_N N}$ = 2.76 TeV with the ALICE experiment at the LHC". Presented on 2017-11-20. 2017. URL: https://cds.cern.ch/record/2655137.

[10] *Measurement of photons stimulates quest for QGP temperature.* URL: https://cerncourier.com/a/measurement-of-photons-stimulates-quest-for-qgp-temperature/#:~:text=One%20of%20the%20classic%20signals,a%20nucleus%E2%80%93nucleus%20collision%20unscathed.. (accessed: 22.07.2022).

[11] Ewa Lopienska. "The CERN accelerator complex, layout in 2022. Complexe des accélérateurs du CERN en janvier 2022". In: (Feb. 2022). General Photo. URL: https://cds.cern.ch/record/2800984.

[12] Barthelemy von Haller, Patryk Lesiak, and Jacek Otwinowski and. "Design of the data quality control system for the ALICE O2". In: *Journal of Physics: Conference Series* 898 (Oct. 2017), p. 032001. DOI: 10.1088/1742-6596/898/3/032001. URL: https://doi.org/10.1088/1742-6596/898/3/032001.

[13] Dominik Mierzejewski and Janusz Rzeszut. "Roman Pot Detector Modelling and Proton Reconstruction in the TOTEM Experiment at the LHC". PhD thesis. Oct. 2010.

[14] *ALICE scrutinizes proton-lead run for quark-gluon plasma.* URL: https://home.cern/news/news/accelerators/alice-scrutinizes-proton-lead-run-quark-gluon-plasma#:~:text=ALICE%20is%20specialized%20in%20scrutinizing,nucleons%20(protons%20and%20neutrons).. (accessed: 15.07.2022).

[15] "Drawing of the ALICE experiment". In: (). General Photo. URL: https://alice-wiki.gsi.de/bin/view/Main/Research.

[16] Despina Chatzifotiadou. "Particle tracks fly out from the heart of the ALICE experiment from one of the first collisions at a total energy of 7 TeV. Les traces de particules jaillissent du cœur de l'expérience ALICE, résultant de l'une des premières collisions à une énergie totale de 7 TeV". Mar. 2010. URL: https://cds.cern.ch/record/1280693.

[17] F. Reidt. "Upgrade of the ALICE ITS detector". In: *Nuclear Instruments and Methods in Physics Research Section A: Accelerators, Spectrometers, Detectors and Associated Equipment* 1032 (2022), p. 166632. ISSN: 0168-9002. DOI: https://doi.org/10.1016/j.nima.2022.166632. URL: https://www.sciencedirect.com/science/article/pii/S0168900222002042.

[18] B Abelev et al and. "Technical Design Report for the Upgrade of the ALICE Inner Tracking System". In: *Journal of Physics G: Nuclear and Particle Physics* 41.8 (July 2014), p. 087002. DOI: 10.1088/0954-3899/41/8/087002. URL: https://doi.org/10.1088/0954-3899/41/8/087002.

[19] Aglieri Rinella Gianluca. "The ALPIDE pixel sensor chip for the upgrade of the ALICE Inner Tracking System". In: *Nuclear Instruments and Methods in Physics Research Section A: Accelerators, Spectrometers, Detectors and Associated Equipment* 845 (2017). Proceedings of the Vienna Conference on Instrumentation 2016, pp. 583–587. ISSN: 0168-9002. DOI: https://doi.org/10.1016/j.nima.2016.05.016. URL: https://www.sciencedirect.com/science/article/pii/S0168900216303825.

[20] J. Adolfsson et al. "The upgrade of the ALICE TPC with GEMs and continuous readout". In: *Journal of Instrumentation* 16.03 (Mar. 2021), P03022. DOI: 10.1088/1748-0221/16/03/p03022. URL: https://doi.org/10.1088/1748-0221/16/03/p03022.

[21] Ketil Røed et al. "Single Event Upsets in SRAM FPGA based readout electronics for the Time Projection Chamber in the ALICE experiment". In: (June 2022).

[22] F. Sauli. "GEM: A new concept for electron amplification in gas detectors". In: *Nuclear Instruments and Methods in Physics Research Section A: Accelerators, Spectrometers, Detectors and Associated Equipment* 386.2 (1997), pp. 531–534. ISSN: 0168-9002. DOI: https://

109

doi.org/10.1016/S0168-9002(96)01172-2. URL: https://www.sciencedirect.com/science/article/pii/S0168900296011722.

[23] A.Andronic. *ALICE TRD - Introduction*. [Online; accessed 17-June-2022]. URL: http://www-alice.gsi.de/trd/intro.html.

[24] "The ALICE Transition Radiation Detector: Construction, operation, and performance". In: *Nuclear Instruments and Methods in Physics Research Section A: Accelerators, Spectrometers, Detectors and Associated Equipment* 881 (2018), pp. 88–127. ISSN: 0168-9002. DOI: https://doi.org/10.1016/j.nima.2017.09.028. URL: https://www.sciencedirect.com/science/article/pii/S0168900217309981.

[25] Wolfgang Demtröder. *Experimentalphysik 4. Kern-, Teilchen- und Astrophysik*. Springer-Verlag GmbH Berlin Heidelberg, 2017. ISBN: 978-3-662-52883-9.

[26] Fabio Sauli. "Interaction of photons and neutrons with matter". In: *Gaseous Radiation Detectors: Fundamentals and Applications*. Cambridge Monographs on Particle Physics, Nuclear Physics and Cosmology. Cambridge University Press, 2014, pp. 43–75. DOI: 10.1017/CBO9781107337701.005.

[27] D.E. Groom and S.R. Klein. *Passage of Particles Through Matter*. [accessed 07-August-2022]. URL: https://pdg.lbl.gov/2022/reviews/contents_sports.html.

[28] Prof. Dr. Johanna Stachel. *Detectors in Nuclear and Particle Physics*. July 2018.

[29] Silvia Masciocchi. *Detectors for particle tracking and identification*. Oct. 2017.

[30] David Rohr. *Overview of the ALICE O2 System*. URL: https://indico.phy.ornl.gov/event/112/contributions/469/attachments/496/1348/2021-12-09_Streaming_Readout_Workshop_O2.pdf.

[31] Pierre Vande Vyvre. *ALICE Computing System for Run 3 and Run 4: the O2 Project*. URL: https://indico.cern.ch/event/471309/contributions/1981065/.

[32] P Buncic, M Krzewicki, and P Vande Vyvre. *Technical Design Report for the Upgrade of the Online-Offline Computing System*. Tech. rep. Apr. 2015. URL: https://cds.cern.ch/record/2011297.

[33] Federico Antinori and Urs Wiedemann. "ALICE: Physics Performance Report, Volume II". In: *Journal of Physics G: Nuclear and Particle Physics* 32.10 (Sept. 2006). DOI: 10.1088/0954-3899/32/10/e01. URL: https://doi.org/10.1088/0954-3899/32/10/e01.

[34] Data Preparation Group. *Analysis Tutorial*. URL: https://twiki.cern.ch/twiki/bin/viewauth/ALICE/AliceDPG.

[35] Cristina Agrigoroae. *The four LHC experiments are getting ready for pilot beams*. https://home.cern/news/news/experiments/four-lhc-experiments-are-getting-ready-pilot-beams. 2021.

[36] *Hyperloop system*. accessed 29.08.2022. URL: https://aliceo2group.github.io/analysis-framework/docs/hyperloop/.

[37] "The ALICE definition of primary particles". In: (June 2017). URL: https://cds.cern.ch/record/2270008.

[38] B Abelev et al and. "Upgrade of the ALICE Experiment: Letter Of Intent". In: *Journal of Physics G: Nuclear and Particle Physics* 41.8 (July 2014), p. 087001. DOI: 10.1088/0954-3899/41/8/087001. URL: https://doi.org/10.1088/0954-3899/41/8/087001.

[39] "Performance of the ALICE experiment at the CERN LHC". In: *International Journal of Modern Physics A* 29.24 (Sept. 2014), p. 1430044. DOI: 10.1142/s0217751x14300440. URL: https://doi.org/10.1142%2Fs0217751x14300440.

[40] *The Large Hadron Collider*. URL: https://home.cern/science/accelerators/large-hadron-collider. (accessed: 27.05.2022).

[41] *Accelerator upgrades during LS2*. URL: https://home.cern/press/2022/accelerator-upgrades-during-ls2. (accessed: 27.05.2022).

[42] Dominik Mierzejewski and Janusz Rzeszut. "Roman Pot Detector Modelling and Proton Reconstruction in the TOTEM Experiment at the LHC". PhD thesis. Oct. 2010.

[43] *Diverse experiments at CERN*. URL: https://home.cern/science/experiments#:~:text=LHC%5C%20experiments,and%5C%20characterised%5C%20by%5C%20its%5C%20detectors.. (accessed: 30.05.2022).

[44] *ATLAS*. URL: https://home.cern/science/experiments/atlas. (accessed: 30.05.2022).

[45] *CMS*. URL: https://home.cern/science/experiments/cms. (accessed: 30.05.2022).

[46] *LHCb*. URL: https://home.cern/science/experiments/lhcb. (accessed: 30.05.2022).

[47] *ALICE*. URL: https://home.cern/science/experiments/alice. (accessed: 30.05.2022).

[48] *LHCf*. URL: https://home.cern/science/experiments/lhcf. (accessed: 31.05.2022).

[49] *TOTEM*. URL: https://home.cern/science/experiments/totem. (accessed: 31.05.2022).

[50] *FASER*. URL: https://home.cern/science/experiments/faser. (accessed: 31.05.2022).

[51] Claudia Marcelloni and Max Brice. "The first ATLAS Inner Detector End-cap after complete insertion within the Liquid Argon Cryostat.. Le premier détecteur interne bouchon d'ATLAS après son insertion à l'intérieur de son cryostat d'argon liquide". May 2007. URL: https://cds.cern.ch/record/1035456.

[52] Maximilien Brice. "Replacement of the heart of the CMS experiment - the pixel detector, Part2". In: (Mar. 2017). General Photo. URL: https://cds.cern.ch/record/2254952.

[53]   Maximilien Brice and Julien Marius Ordan. "LHCb YETS 2018". In: (Jan. 2018). General Photo. URL: https://cds.cern.ch/record/2302374.

[54]   Julien Ordan. "Inside ALICE detector empty skeleton". In: (Mar. 2019). General Photo. URL: https://cds.cern.ch/record/2665476.

[55]   Maximilien Brice. "Nicola Turini, Deputy-Spokesperson TOTEM experiment in the LHC tunnel". In: (Sept. 2016). General Photo. URL: https://cds.cern.ch/record/2215532.

[56]   Lorenzo Bonechi. "One of the LHCf experiment's two detectors, LHCf Arm2, seen here during installation into a particle absorber that surrounds the LHC's beam pipe." In: (Nov. 2019). General Photo. URL: https://cds.cern.ch/record/2699736.

[57]   Maximilien Brice. "First phase of installation of FASER in the LHC tunnel". In: (Nov. 2020). General Photo. URL: http://cds.cern.ch/record/2744976.

[58]   *ALICE ITS*. https://alice-collaboration.web.cern.ch/node/34999. [Online; accessed 06-June-2022].

[59]   *ALICE ITS*. https://ep-news.web.cern.ch/content/alice-its-upgrade-pixels-quarks. [Online; accessed 06-June-2022].

[60]   Deb Bhattacharya et al. "Preliminary results of Ion Backflow study for a single GEM detector". In: (Aug. 2017).

[61]   *Addendum to the Technical Design Report for the Upgrade of the ALICE Time Projection Chamber*. Tech. rep. Feb. 2015. URL: https://cds.cern.ch/record/1984329.

[62]   Chilo Garabatos. *The ALICE TPC is upgraded*. https://home.cern/news/news/experiments/alice-tpc-upgraded. 2020.

[63]   *The ALICE Time Projection Chamber*. https://alice-tpc.web.cern.ch/content/alice-time-projection-chamber. [Online; accessed 11-June-2022]. 2020.

[64] P Cortese. *ALICE transition-radiation detector: Technical Design Report*. Technical design report. ALICE. Geneva: CERN, 2001. URL: https://cds.cern.ch/record/519145.

[65] Matthias Richter. "A design study for the upgraded ALICE computing facility". In: *Journal of Physics: Conference Series* 664.8 (Dec. 2015), p. 082046. DOI: 10.1088/1742-6596/664/8/082046. URL: https://doi.org/10.1088/1742-6596/664/8/082046.

[66] *Software, Physics Data Processing and Computing Coordination*. URL: https://alice-collaboration.web.cern.ch/organisation/pdp/index.html. (accessed: 29.07.2022).

[67] Tomá š Husek, Evgueni Goudzovski, and Karol Kampf. "Precise Determination of the Branching Ratio of the Neutral-Pion Dalitz Decay". In: *Physical Review Letters* 122.2 (Jan. 2019). DOI: 10.1103/physrevlett.122.022003. URL: https://doi.org/10.1103%2Fphysrevlett.122.022003.

Erklärung

Ich versichere, dass ich diese Arbeit selbstständig verfasst und keine anderen als die angegebenen Quellen und Hilfsmittel benutzt habe.

Heidelberg, den 06.09.2022,

Nikita Totsch